An experimental study on collisional evolution of highly porous small bodies

岡本，尚也

(Degree)
博士（理学）
(Date of Degree)
2015-03-25
(Date of Publication)
2017-03-25
(Resource Type)
doctoral thesis
(Report Number)
甲第6331号
(URL)
https://hdl.handle.net/20.500.14094/D1006331

博　士　論　文

An experimental study on collisional evolution of highly porous small bodies

空隙の大きな小天体の衝突進化に関する
実験的研究

平成27年1月

神戸大学大学院理学研究科

岡本　尚也

Contents

Abstract

Small bodies in the solar system have clues of the early solar system. One of important processes for evolutions of small bodies is impact. Recent space craft missions have found highly porous small bodies, and particularly comets have porosities even up to about 90%. In order to derive information on the physical properties of small bodies and their collisional evolution, it is necessary to investigate what kind of crater morphology is formed on such a small body by what kind of collision condition, and how much the bodies are disrupted by impact. However, impact processes for such highly porous bodies have not been understood well. In this study, we prepared targets with porosities ranging from 50% to 94%, and conducted impact experiments with impact velocities of 1.6–7.2 km^{-1}.

In Chapter 2, we investigated the penetration processes of projectiles into porous bodies. After the formation of small bodies, interplanetary dust particles impacting on their surface may have been captured because of their porous structure, and may have changed their composition of surface from original composition. The mechanism of dust penetration is thus of importance to understand the evolution of small bodies. Impact experiments of sintered glass-bead targets characterized by 80%, 87%, and 94% bulk porosity were conducted. Two types of track were observed: a thin and long track (carrot-shaped track), and a “bulb” with or without tails (bulb-shaped track). The deceleration process of projectiles without severe deformation and fragmentation was reproduced by a drag equation composed of an inertia drag that was proportional to the square of the projectile’s velocity and a constant drag proportional to the target’s compressive strength. We applied this deceleration equation to silicate dust penetrating into porous icy bodies. The penetration depth was approximately 100 times the projectile diameter for the bodies with 90% porosity.

In Chapter 3, we examined the craters formed on porous targets in strength regime in order to obtain the scaling relations for crater-dimensions. Impact experiments on sintered glass-bead targets with porosities of 87%, 93% and 94% as well as gypsum targets with porosity of 50% and pumice targets with porosity of 74%, were performed. The resulting cavity dimensions formed by these impacts were examined. We obtained empirical relations for the maximum diameter and the bulb depth. We applied our scaling relations to the surface of porous icy bodies. The surface strength of 9P/Tempel 1 was estimated to be of the orders of 10^1–10^3 Pa. We presented the possibility of formation of shallow craters on comets due only to impacts.

In Chapter 4, we summarized the disruption thresholds, Q^* for targets of various porosities. We conducted impact disruption experiments for targets with porosities of 80%, 87%, and 94%. Each Q^* value is on the order of kilojoules per kilogram, which is higher than the equivalent values for pure ice targets and basalt targets determined from high-velocity impact experiments. Comparisons with the results of various previous studies show that Q^* increases with increasing static compressive strength and with increasing porosity of the targets. We calculated the non-dimensional disruption thresholds, Π_s^* , which is previously proposed as strength parameter for the catastrophic disruption threshold. It is shown to be roughly constant, irrespective of porosity if we assume that a scaling parameter, μ decreases linearly with increasing porosity.

Chapter 1

General Introduction

1.1 Impact processes in the solar system

Impact is a fundamental phenomenon in the history of the solar system. The bodies in the solar system have experienced impacts and have been evolved. If bodies are heavily impacted, they are catastrophically disrupted. An asteroid family which is a population of asteroids that share similar proper orbital elements are considered to be fragments of a parent asteroid (e.g. Fujiwara, 1982). In contrast, smaller scale impacts form craters on their surfaces. Lunar craters smaller than about 15 km in diameter are simple craters with depth/diameter ratio 0.2 (Pike, 1974). Further large craters are often called basins, and the largest basin on the Moon is South Pole-Aitken basin, which located in far side of the Moon, with diameter of roughly 2,500 km (Petro and Pieters, 2004). Asteroids, comets, Trans-Neptunian objects (TNOs) are classified as small bodies. Craters on such small bodies have been observed by telescopes and spacecrafts, and the detail images of the craters have been obtained recently. For example, Deep Impact spacecraft observed a large amount of pits, or circular depressions on comet 9P/Tempel 1 (Thomas *et al.*, 2007a). The surface of Tempel 1 has many merged depressions ranging from 10 to 100 m across. The larger, isolated, rimless depressions are found on its surface and they range from 100 to 400 m in diameter, have no raised rims, have usually flat floors, concentric

albedo markings. Depths are well under 50 m. Depressions with rim remnants are also observed. They appear to be nearly circular raised rims of varying width, darker than their surroundings. Their interior fill is identical in color to the outside material. The largest of this type of depressions is 350 m in diameter, and the rim hight can only be estimated less than 30 m. Cassini spacecraft obtained high-resolution images of Hyperion, which is one of Saturn's irregular satellites (Thomas *et al.*, 2007b). They reveal a unique sponge-like appearance at scales of a few kilometers. The depth-to-diameter ratio of the craters on Hyperion was reported to be ~0.3 by White and Schenk (2011). The unusual appearances of Hyperion are dark surfaces in the floors of degraded craters. Whether these features on the icy bodies were caused by impact or sublimation or both of them is not understood well (e.g. Thomas *et al*., 2007b; Howard *et al*., 2012; Vincent *et al*., 2014).

Impacts also contribute to the composition of planetesimals and small bodies. They were formed by accretion of dust aggregates (e.g. Kataoka *et al.*, 2013), thus the aggregates are considered to be the primary component of the small bodies. On the other hand, dust particles transported from different region from the original formation region of the bodies may have modified the surface structure and composition of the original bodies. Dust particles collected from comet 81P/Wild 2, a Jupiter-family comet (JFC) that is believed to have formed in the outer region of the solar system and to have only recently entered the inner regions of the solar system (Brownlee *et al.*, 2006), were found to contains refractory objects resembling such as meteoritic Calsium-Alminum-rich Inclusion (CAI) (e.g. Brownlee *et al.*, 2006; McKeegan *et al.*, 2006; Zolensky *et al.*, 2006). The presence of high-temperature objects in a comet such as CAI-like, chondrule-like fragments suggests that the objects formed near the Sun were transported to the formation region of the icy bodies and captured.

Recent spacecraft missions have found that small bodies are porous, and particularly comets have extremely high porosities as seen in next section. Though the effect of the

porosity may play an important role in disruption, cratering of the bodies, and capture of dust particles, so far, little impact experiments with simulated highly porous bodies have been conducted. In order to understand collisional history of small bodies, thus it is necessary to investigate how deep impactor can penetrate into the bodies, what kind of crater morphology is formed on such a small body by what kind of collision condition, and how much the bodies are disrupted by impact.

1.2 Small bodies in the solar system

Small bodies have been formed from planetesimals. Kataoka *et al.* (2013) calculated density evolution of icy planetesimals by numerical simulation. Dust with sub-micron size first coagulated by hit-and-stick, and became fluffy aggregates. Then they were subjected to the effect of compression due to gas pressure and self-gravitation, the aggregates became planetesimals (Kataoka *et al.*, 2013). Density of the dust aggregates during their formation is less than 100 kg m^{-3}. It corresponds to porosity of larger than ~90%.

Recent spacecraft missions and advancement of meteorite studies allow to estimate the density and porosity of present small bodies. Those data show that small bodies have high porosities. Consolmagno *et al.* (2008) studied meteorite densities and porosity. Assuming what kind of meteorites or materials compose the small bodies, they deduced densities and porosities of asteroids and comets. The average porosities of S-type, C-type, and M-type asteroids are 19.9±1.2%, 37.7±2.2%, and 40±13%, respectively. Figure 1.1 shows porosity of comet nuclei. Extremely high porosities can be found for comets. Though some of them have large errors, comets have porosities even up to about 90%.

It may be suggested that the surface of small bodies are diverse. For example, sintered layers, regolith layers, and monolith may exist on their surfaces. The surface is also considered to compose of a variety of material such as silicate, metal, water ice, carbon dioxide ice, and other volatile materials. Here we describe the strength in some cases.

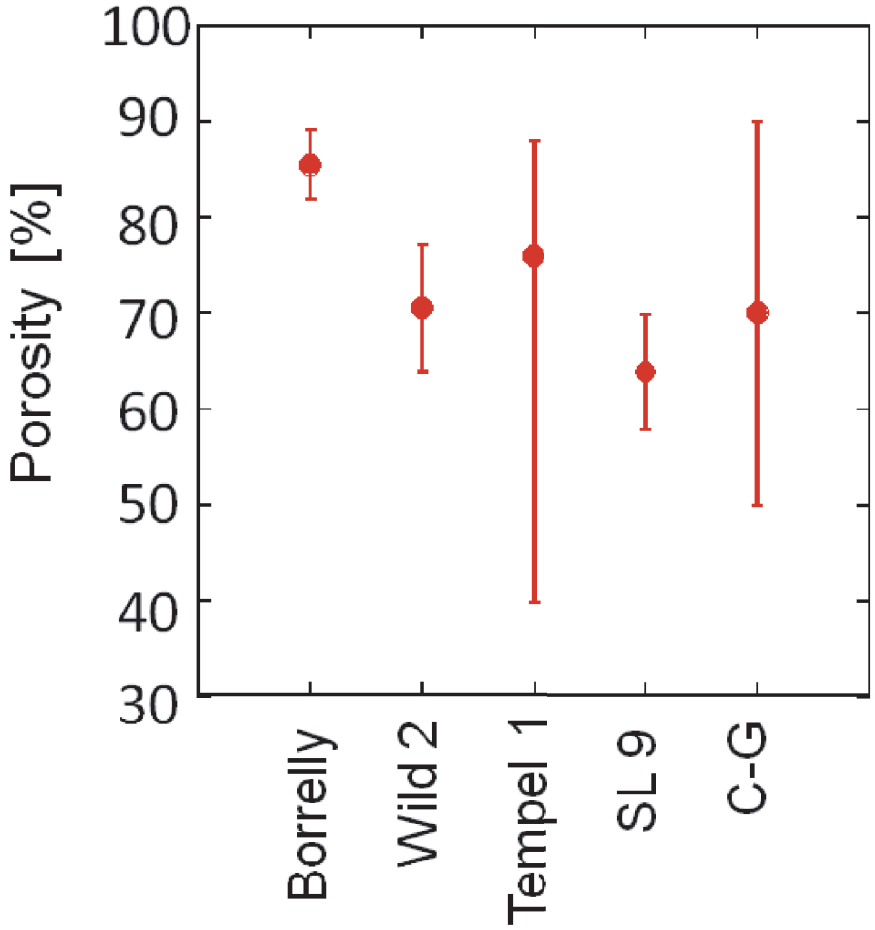

Figure 1.1: Bulk porosity of comets. C-G indicates comet 67P/Churyumov-Gerasimenko. Reference for C-G is from Davidsson and Gutierrez (2005), the others are from Consolmagno *et al.* (2008).

For the case of icy small bodies, the simplest putative case is that the surface is composed of snow. Mellor (1974) reviewed the basic snow mechanics. The uniaxial strength of bonded dry snow is given in the review. The tensile and compressive strengths for strain rates 10^{-4} to 10^{-2} s^{-1} are functions of density. The values of tensile and compressive strength range 10^3–2×10^6, and 10^3–10^7 Pa, respectively. Tensile and compressive strength are equal at lower densities, while at the density of solid ice the ratio of compressive strength to tensile strength is about 5. Arakawa and Tomizuka (2004) measured static compressive strength for pure ice targets and ice-silicate mixture targets (0.5 in mass ratio of ice to silicate) with 4 different porosities (12.5, 25, 32, 37%) in order to examine the relationship between porosity and mechanical strength. The uniaxial tests at a strain rate of 5.6×10^{-3} s^{-1} resulted in compressive strength, Y_c as a function of filling factor, f;

$$Y_c = Y_0 f^n, \tag{1.1}$$

where Y_0 and n are 9.8×10^6 Pa and 3.4, 9.5×10^6 MPa and 6.4 for pure ice targets and mixture targets, respectively. Note that filling factor, f is defined as $1 - \phi/100$ (The unit of ϕ is %). The result of pure ice targets is consistent with the data in Mellor (1974). The static compressive strength of the mixture targets is weaker than that of the pure ice targets.

Blum *et al.* (2006) listed the cometary tensile strength, and the strength of 46P/Wirtanen is 500 ± 450 Pa. Unfortunately, data on cometary tensile strengths are very scarce and in most cases yield lower limits. The Deep Impact mission successfully collided a 366 kg impactor-spacecraft with the surface of 6 km diameter comet Tempel 1 (A'Hearn *et al.*, 2005). Richardson *et al.* (2007) computed the ejected mass and estimated the strength of the comet Tempel 1 at the impact site. They compared their results with the excavated total mass determined from various observational measurments, and the results indicates an upper limit of the surface strength of the comet of order 10^3–10^5 Pa, with the range of 10^3–10^4 Pa being most likely.

1.3 Scaling laws of impact crater-dimensions

What parameters determine crater size? They are considered to be mass, m_p, radius, r_p, impact velocity, v_0, bulk density, ρ_p, and strength, Y_p, of an impactor, and bulk density, ρ_t, porosity, ϕ, strength, Y_t, and gravitational acceleration of the surface, g of a target. Crater scaling law is a relationship between crater size and impact condition. Establishing the scaling laws is necessary for understanding impact phenomena under general conditions. Holsapple developed an approach of a non-dimensional anaylysis for impact crater scaling, in which physical parameters such as above are combined into some non-dimensional parameters, π group (e.g. Holsapple and Schmidt, 1982; Holsapple, 1993). For example, crater volume, V of a transient crater can be expressed as:

$$V = f\left(v_0, \rho_\mathrm{p}, \rho_\mathrm{t}, Y_\mathrm{t}, g, m\right). \tag{1.2}$$

There are seven variables, however, all physical quantities can be expressed in terms of mass, length, and time. Thus 4 (=7-3) non-dimensional parameters can be formed. The π groups are

$$\pi_\mathrm{V} = \frac{\rho_\mathrm{t} V}{m_\mathrm{p}}, \tag{1.3}$$

$$\pi_2 = \frac{g}{{v_0}^2}\left(\frac{m_\mathrm{p}}{\rho_\mathrm{p}}\right)^{1/3} \quad \text{or} \quad \pi_2 = \frac{g r_\mathrm{p}}{{v_0}^2}, \tag{1.4}$$

$$\pi_3 = \frac{Y_\mathrm{t}}{\rho_\mathrm{p} {v_0}^2}, \tag{1.5}$$

$$\pi_4 = \frac{\rho_\mathrm{t}}{\rho_\mathrm{p}}. \tag{1.6}$$

π_V is often called crater efficiency, which is defined by the ratio of the mass of material originally contained within the crater to the mass of the projectile. The importance of gravity is expressed by π_2, which is the ratio of gravitational and inertial stresses. Strength is gauged by π_3, the ratio of material strength to dynamic pressure. π_4 is the ratio of target

and projectile density. Eq. (1.2) can be described by these dimensionless parameters:

$$\pi_{\mathrm{V}} = f'(\pi_2, \pi_3, \pi_4). \tag{1.7}$$

The scaling law in Eq. (1.7) can be simplified by assuming that the effect of gravity is negligible. This is what is called the "strength regime". Conversely, it can be simplified by assuming that the effect of strength is negligible. This case is called "gravity regime". Thus the dimensionless parameters of crater volume, π_{V} can be expressed by a function of π_2 in the gravity regime and by a function of π_3 in the strength regime.

Holsapple (1993) reviews the scaling of impact cratering. On the basis of his point source assumption, the coupling prameter, C, which is defined by

$$C = r_{\mathrm{p}} v^{\mu} \rho_{\mathrm{p}}^{\nu}, \tag{1.8}$$

is considered to be an important parameter for impact cratering, where both μ and ν are scaling constants. If impact phenomena is dependent on kinetic energy of projectile, μ equals 2/3, whereas if it is dependent on the momentum, μ equals 1/3. Theoretically, μ values of all materials must be between these scaling limits. Introducing this coupling parameter, Ep.(1.2) can be expressed as

$$V = f''(C, \rho_{\mathrm{t}}, Y_{\mathrm{t}}, g). \tag{1.9}$$

In this case, there are five variables, thus 2 (=5-3) independent dimensionless parameters can be formed. Two alternative useful forms obtained are

$$\rho_{\mathrm{t}} \frac{V}{m_{\mathrm{p}}} \left(\frac{Y_{\mathrm{t}}}{\rho_{\mathrm{t}} {v_0}^2} \right)^{3\mu/2} \left(\frac{\rho_{\mathrm{t}}}{\rho_{\mathrm{p}}} \right)^{3\nu-1} = F\left(\frac{g r_{\mathrm{p}}}{{v_0}^2} \left(\frac{\rho_{\mathrm{t}} {v_0}^2}{Y_{\mathrm{t}}} \right)^{(2+\mu)/2} \left(\frac{\rho_{\mathrm{t}}}{\rho_{\mathrm{p}}} \right)^{-\nu} \right), \tag{1.10}$$

$$\rho_{\mathrm{t}} \frac{V}{m_{\mathrm{p}}} \left(\frac{g r_{\mathrm{p}}}{{v_0}^2} \right)^{3\mu/(2+\mu)} \left(\frac{\rho_{\mathrm{t}}}{\rho_{\mathrm{p}}} \right)^{(6\nu-2-\mu)/(2+\mu)} = G\left(\frac{Y_{\mathrm{t}}}{\rho_{\mathrm{t}} {v_0}^2} \left(\frac{g r_{\mathrm{p}}}{{v_0}^2} \right)^{-2/(2+\mu)} \left(\frac{\rho_{\mathrm{t}}}{\rho_{\mathrm{p}}} \right)^{-2\nu/(2+\mu)} \right). \tag{1.11}$$

In strength regime, the right side of Eq. (1.10) is constant because it should not depend on g in the regime. Thus the following equation can be obtained, using a scaling constant, K_1:

$$\rho_{\mathrm{t}} \frac{V}{m_{\mathrm{p}}} = K_1 \left(\frac{Y_{\mathrm{t}}}{\rho_{\mathrm{t}} {v_0}^2} \right)^{-3\mu/2} \left(\frac{\rho_{\mathrm{t}}}{\rho_{\mathrm{p}}} \right)^{1-3\nu}. \tag{1.12}$$

In gravity regime, the right side of Eq. (1.13) is constant because it should not depend on Y_t in the regime. Thus the following equation can be obtained, using a scaling constant, K_2:

$$\rho_t \frac{V}{m_p} = K_2 \left(\frac{g r_p}{{v_0}^2}\right)^{-3\mu/(2+\mu)} \left(\frac{\rho_t}{\rho_p}\right)^{(-6\nu+2+\mu)/(2+\mu)} . \tag{1.13}$$

Using these relationship, scaling constants μ, ν, K_1, and K_2 are determined by impact experiments. The exponent ν is typically equal to 1/3 (Housen and Holsapple, 2003) or 0.4 (Housen and Holsapple, 2011) regardless of material type. The exponent μ is 0.41 for sand, and 0.55 for nonporous materials, such as water, metals, or rock. The value of μ tends to decrease with porosity (Housen and Holsapple, 2003). Since we focus here on the effects of target porosity, the above forms should be changed. Housen and Holsapple (2003) added the dependence of porosity to the previous forms (Holsapple and Schmidt, 1987). Table 1.1 summarizes the scaling laws about crater diameter and depth as well as crater volume, allowing for a porosity effect.

Table 1.1: Summary of scaling laws in strength and gravity regimes, allowing for a porosity effect (Housen and Holsapple, 2003).

Crater dimension	Strength regime	Gravity regime
Volume V	$\rho_t \frac{V}{m_p} = K_{Vs}(\phi) \left(\frac{Y_t}{\rho_p {v_0}^2}\right)^{\frac{-3\mu}{2}} \left(\frac{\rho_t}{\rho_p}\right)^{1-3\nu+\frac{3\mu}{2}}$	$\rho_t \frac{V}{m_p} = K_{Vg}(\phi) \left(\frac{g r_p}{{v_0}^2}\right)^{\frac{-3\mu}{2+\mu}} \left(\frac{\rho_t}{\rho_p}\right)^{\frac{-6\nu+2+\mu}{2+\mu}}$
Diameter D	$D \left(\frac{\rho_t}{m_p}\right)^{\frac{1}{3}} = K_{Ds}(\phi) \left(\frac{Y_t}{\rho_p {v_0}^2}\right)^{\frac{-\mu}{2}} \left(\frac{\rho_t}{\rho_p}\right)^{1-3\nu+\frac{\mu}{2}}$	$D \left(\frac{\rho_t}{m_p}\right)^{\frac{1}{3}} = K_{Dg}(\phi) \left(\frac{g r_p}{{v_0}^2}\right)^{\frac{-\mu}{2+\mu}} \left(\frac{\rho_t}{\rho_p}\right)^{\frac{-6\nu+2+\mu}{3(2+\mu)}}$
Depth d	$d \left(\frac{\rho_t}{m_p}\right)^{\frac{1}{3}} = K_{ds}(\phi) \left(\frac{Y_t}{\rho_p {v_0}^2}\right)^{\frac{-\mu}{2}} \left(\frac{\rho_t}{\rho_p}\right)^{1-3\nu+\frac{\mu}{2}}$	$d \left(\frac{\rho_t}{m_p}\right)^{\frac{1}{3}} = K_{dg}(\phi) \left(\frac{g r_p}{{v_0}^2}\right)^{\frac{-\mu}{2+\mu}} \left(\frac{\rho_t}{\rho_p}\right)^{\frac{-6\nu+2+\mu}{3(2+\mu)}}$

$K_{Vs}, K_{Vg}, K_{Ds}, K_{Dg}, K_{ds}$, and K_{dg} are scaling constants as a function of porosity. Note that Housen and Holsapple (2003) listed radius, R of a crater dimension. We changed radius, R to diameter, D in this list for convenience in this study.

It is important whether surface of small bodies is dominated by strength or gravity when we consider crater formation on the surface. As the first order of approximation, the formation of the crater is controlled by strength, i.e., strength regime, when surface strength, Y_t is much larger than $\rho_t gD$. On the other hand, the formation of the crater is controlled by gravity, i.e., gravity regime, when $\rho_t gD$ is much larger than Y_t. For comet Tempel 1, g is 3.4×10^{-4} m s^{-2} and ρ_t is 4×10^2 kg m^{-3}(Richardson *et al.*, 2007). For 81P/Wild 2 g is 3×10^{-4} m s^{-2} (Schmude, 2010), and ρ_t is 4.9×10^2 kg m^{-3}(Consolmagno *et al.*, 2008). When crater diameter, D of 100 m is assumed, $\rho_t gD$ for both cases are of the order of 10 Pa. Strength of comet surface, Y_t is supposedly expected to be similar to the strength of H_2O snow, 10^3–10^7 Pa (Mellor, 1974). These values are much larger than 10 Pa. The surface strength of Tempel 1 estimated by Richardson *et al.* (2007) is also larger than the value. Therefore the condition of crater formation on comet surfaces would be strength regime.

1.4 Catastrophic disruption threshold

The outcome of a collision depends on an energy density, Q, which is also called a specific energy. The energy density is defined as the ratio of the kinetic energy of the impactor to the mass of the target (Gault and Wedekind, 1969; Fujiwara *et al.*, 1977). Impact with extremely small values of Q, results in just rebound of impactor. Larger values of Q form craters, whereas further larger values can shatter a target into pieces. The specific energy to shatter, Q_S^* is defined as the threshold value of the energy density for which the largest remnant following a collision has one-half the mass of the original body (e.g. Greenberg and Hartmann, 1977; Hartmann, 1980). The specific energy, Q_S^* is often called the shattering energy. Whether the shattered pieces reaccumulate or not depends on their velocity relative to the escape velocity. A threshold Q_D^* is defined as the threshold of energy density such that the largest object following reaccumulation is one-half the mass

of the original body (Davis *et al.*, 1979). It is called the dispersion energy. In this study, we focus on the shattering energy Q^*_S. Hereafter Q^* denotes Q^*_S unless we note particular attention.

A lot of experiments of catastrophic disruption using various targets have been conducted, and the shattering energy, Q^*_S of each target was determined. The power-law relationship between the largest fragment mass ratio and energy density was generally reported by previous studies and the degree of fragmentation is strongly dependent on the target material. For example, Q^* for metal is approximately four orders of magnitude larger than that for ice (Holsapple *et al.*, 2002). The strength and porosity of targets may be the dominant physical properties governing an impact disruption. The mechanics of impacts into highly porous targets is substantially different from those into low-porosity targets, due to significant energy losses as the shock wave compacts the target material. Ryan *et al.* (1999) conducted impact experiments into porous and solid ice targets. The results shows that Q^* for porous ice was larger by a factor of about 5 than that for solid ice. Love *et al.* (1993) used porous sintered glass-bead targets with varying strengths and porosities. They showed an empirical equation: Q^* is proportional to $f^{-3.6}$. Sintered glass-bead targets with similar porosity of ~40% but different compressive strength (between 0.035–2.2 MPa) were prepared in Setoh *et al.* (2010). They found that the value of Q^* increases with the target compressive strength.

1.5 Purpose of this study

In this dissertation, we study the impact cratering and disruption of highly porous bodies. We conducted high-velocity impact experiments at impact velocities ranging from 1.6 to 7.2 km s^{-1}. In Chapter 2, we examine the penetration process of the projectile in order to estimate how deep dust can penetrate into the bodies. In Chapter 3 we investigate the cavity morphology, and estimated the surface strength of Tempel 1 and the depth-to-

diameter ratio of craters on icy bodies. In Chapter 4 we investigate disruption threshold Q^* of porous targets. Our summary is presented in Chapter 5.

Chapter 2

Experimental study of dust penetration into porous bodies[*1]

2.1 Introduction

Early planetesimals that formed from dust aggregates are thought to have been very porous. Numerical simulations of sequential collisions of water-ice dust aggregates showed that aggregates in protoplanetary disks had an extremely low density (< 100 kg m^{-3}), which corresponds to a bulk porosity of more than 90% (Kataoka *et al.*, 2013). The previous experimental study (Blum and Schräpler, 2004) also showed that laboratory-grown random ballistic-deposition aggregates of non-ice particles with diameter of 1.5 μm have been shown to have a bulk porosity of 85% if mono-disperse spherical dust grains are used. Deviation from sphericity resulted in an increase of the porosity to 89%, whereas a wide size distribution of irregularly shaped monomers yielded an even higher porosity of 93%.

Planetesimals collided with each other and evolved into small primitive bodies, and their bulk porosity decreased through mechanisms such as compaction caused by collisions, disk-gas pressure, self-gravity (Kataoka *et al.*, 2013), and/or sintering (Yomogida

[*1]An earlier version of this chapter has been published as:
Okamoto T., Nakamura A. M., Hasegawa S., Kurosawa K., Ikezaki K., and Tsuchiyama A. 2013. Impact experiments on capture of exotic dust grains by highly porous primitive bodies. *Icarus* **224**, 209—217.

and Matsui, 1984). However, some of the resulting small bodies —such as asteroids, comets, and Kuiper Belt Objects (KBOs)—still have high bulk porosities. The macro-porosities of C-class asteroids, for example, are estimated to range from a few to 60% if asteroids are assumed to consist of carbonaceous chondrites. The macro-porosities of comets are estimated to be even higher, up to 86%, if comets are assumed to consist of water ice and organic material with a CM-like density (Consolmagno *et al.*, 2008). Thus, small primitive bodies have been porous throughout the history of the solar system. Dust can be captured at the surface of such highly porous bodies long after their formation.

Dust particles from comet 81P/Wild 2, a Jupiter-family comet (JFC) that is believed to have formed in the Kuiper Belt and to have only recently entered the inner regions of the solar system, were returned to Earth by the Stardust mission (Brownlee *et al.*, 2006). The dust particles were analyzed and found to contain refractory objects resembling meteoritic Calsium-Alminum-rich Inclusion (CAI) (e.g. Brownlee *et al.*, 2006; McKeegan *et al.*, 2006; Zolensky *et al.*, 2006). Numerous Wild 2 particles also have been shown to be either chondrule fragments or chondrule-like fragments (e.g. Nakamura *et al.*, 2008; Ogliore *et al.*, 2012). The presence of high-temperature objects in a comet such as CAI-like, chondrule-like and chondrule fragments suggests that the objects formed near the Sun were transported to the formation region of the icy bodies. In addition, spectroscopic observations of both Oort Cloud and Jupiter-family comets found that comets consist of crystalline silicate materials, which are produced by a high-temperature process (Harker *et al.*, 2005). It is also thought that the crystalline silicates in comets are evidence of active material transport in the radial direction in the protoplanetary disk (Wooden *et al.*, 2007).

There are two possibilities as to when and how during the history of the solar system the refractory grains became components of the small icy bodies. The first assumes that the grains were original components of these bodies during the accretion stage, and that they were somehow transported from the inner part of the nebula and then mixed with the

initial dust component of the formation region of the icy planetesimals. The second possibility is that grains were collected in a debris disk after the bodies formed. In the second process, exotic components would have accumulated on the surface of the icy bodies and changed their surface composition. For example, short-period comet nuclei would accumulate meteoroids as a consequence of collisions with asteroidal debris (Cintala, 1981).

The purpose of this study is to investigate the penetration depth of dust into small porous bodies. Dust penetration into silica aerogel has been studied extensively for calibration of the Stardust tracks (e.g. Niimi *et al.*, 2011). However, it is not clear how far the understanding thus gained can be extrapolated to dust penetration into small porous primitive bodies in a planetary system. Laboratory impact experiments of cratering and disruption processes of porous targets have been conducted and scaling laws have been studied (Love *et al.*, 1993; Housen and Holsapple, 2003; Setoh *et al.*, 2010; Yasui *et al.*, 2012). In this study, we focus on the penetration process of projectiles into highly porous targets to gain a better understanding of the physical processes of dust penetration into small porous bodies. We conducted impact-penetration experiments of millimeter-sized metal and rock projectiles into highly porous sintered targets, which consisted of pores that were much smaller than the projectiles themselves. Yasui *et al.* (2012) performed similar experiments of a gypsum target with bulk porosity of 50% using metal and nylon projectiles for observation of crater formation and projectile penetration. Targets in this study were much porous with bulk porosities up to 94%. We investigated the deceleration process as well as deformation and fragmentation degree of the projectiles in the porous bodies.

2.2 Experiments

2.2.1 Preparation of targets

We prepared sintered targets characterized by three bulk porosities using glass beads. The preparation procedure was similar to that used in previous experiments (Setoh *et al.*, 2010; Machii and Nakamura, 2011). The sintering conditions and the physical properties of the individual targets are listed in Table 2.1. Hollow soda-lime-borosilicate glass microspheres (3M Co.), with an average diameter and shell thickness of 55 μm, 0.95 μm, respectively, isostatic crush strength of 5.2 MPa and an average grain density of 2.5 g cm^{-3}, were sintered in a cylindrical mold of 60 mm in diameter, 150 mm in height and 10 mm in thickness with a lid of 5 mm in thickness. The targets were heated for 6 hours to two different peak temperatures to attain bulk porosities of 87% and 94%. Low-alkali glass particles of 5 μm in diameter (on average) and 2.6 g cm^{-3}in grain density (on average) were first put through a sieve with 500 μm-wide openings and then poured into the mold for sintering to attain 80% bulk porosity. All targets were heated from room to peak temperature in an oven under atmospheric pressure. Upon reaching peak temperature, each target was cooled naturally in the oven. We named the targets after their bulk porosities: fluffy94, fluffy87, and fluffy80, respectively. The typical target lengths and diameters were 130 and 62 mm, respectively, for fluffy94, 100 and 48 mm for fluffy87, and 130 and 62 mm for fluffy80. An example image of a target is shown in Figure 2.1.

We measured the targets' compressive strengths using a uniaxial compressive testing machine (EZ Graph, SHIMADZU Co.) at Kobe University, Japan. The samples, of size 20×10 mm^2 (length $\times$ diameter), were drilled from different depths of the targets, with their axes parallel to that of the cylindrical target. The core samples were placed in a load frame, which provided a record of the force applied and the displacement of the moving crosshead. The loading rate was 2 μm s^{-1}. Because of the targets' fluffiness, they could

(a)

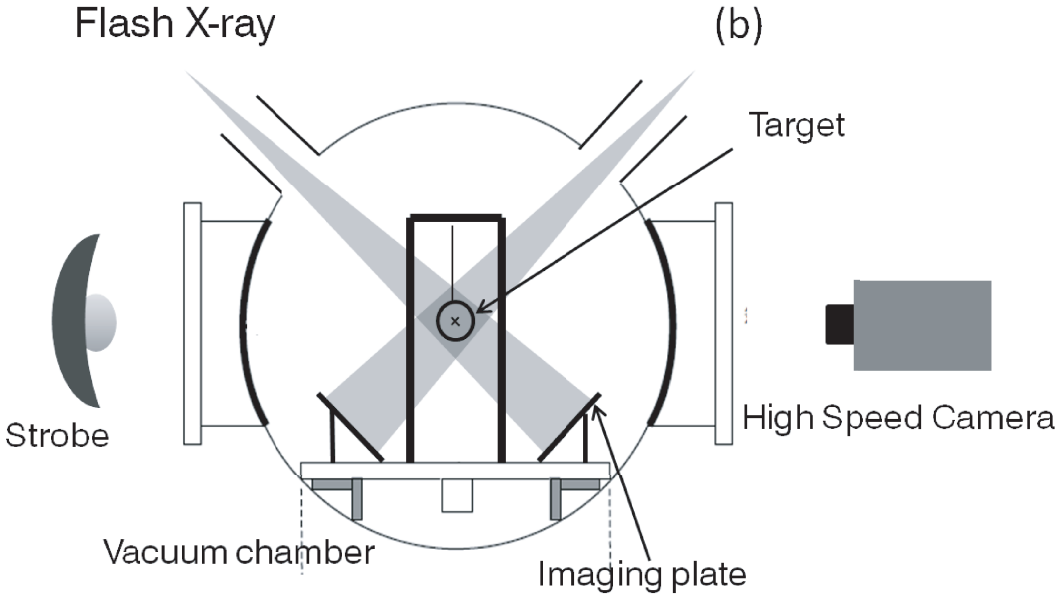

Figure 2.1: (a) Side view of sintered glass-bead target (fluffy94) hung by a thread from the top of a target-support frame. (b) Experimental configuration viewed from the gun muzzle. The targets were suspended from the top of the target box.

Table 2.1: Sintering conditions and physical properties

Target type	Peak temp. (°C)	Duration (h)	Compressive strength of stronger part[a] (MPa)	Compressive strength of weaker part[a] (MPa)	Porosity (%)
fluffy94	700	6	0.47±0.13	0.27±0.04	94.4±0.2
fluffy87	800	6	1.43±0.40	0.86±0.10	86.8±0.3
fluffy80	710	6	–[b]	–[b]	80.3±0.9

[a] The compressive strength was higher for the samples at 0–50 mm and 0–25 mm from the top surface for fluffy94 and fluffy87, respectively (see the text).
[b] Uniaxial compressive strength was not measured because the core could not be obtained due to the target's brittleness. Thus without taking the core samples, original target's surface was loaded by a stainless steel (SUS) cylinder of diameter of 3 mm which was attached to a load cell. The measurement shows 4.5 MPa, which indicated that the value from unconfined uniaxial compressive test must be smaller than 4.5 MPa.

be easily compressed and their contact area with a top and a base plate spread until the stress eventually reached a maximum value and maintained this level. We considered the maximum force applied per unit area of the original cylinder to be the compressive strength of the targets. The compressive strength was higher for the samples at 0–50 mm and 0–25 mm from the top surface for fluffy94 and fluffy87, respectively, probably because of the different thickness of the mold and the lid. The results are shown in Table 2.1, with a standard deviation of 4–6 measurements for different samples, which is much larger than the measurement errors.

2.2.2 Impact experiments

Impact experiments were conducted using a two-stage light-gas gun at the Institute of Space and Astronautical Science (ISAS), Japan. The experimental configuration is illustrated in Figure 2.1. Targets were hung with a thread from the top of a target-support frame placed in a vacuum chamber under an ambient pressure of approximately 10 Pa. We positioned a high-speed video camera at a side window of the chamber and put a strobe light

at the opposite side window to obtain shadowgraph images of projectile and target. The interval between frames was 2–8 μs. We used a flash X-ray system to observe the deceleration processes of the projectiles in non-transparent targets. Targets were illuminated by flash X-rays from two diagonal directions, and X-ray transmission images were recorded on two imaging plates. Controlling the timing of the X-ray exposure, we obtained two successive X-ray images with time intervals between 2 and 50 μs. Table 2.2 summarizes the experimental conditions. The projectiles were titanium, aluminum, and stainless-steel spheres and basalt cylinders. A cylindrical nylon sabot (Kawai *et al.*, 2010) was used for projectile acceleration. The impact velocities ranged from 1.6 to 7.2 km s^{-1}. The targets' track morphologies and the projectiles' final states were observed on transmission images taken by a micro-X-ray tomography instrument [ELE-SCAN NX-NCP-C80-I (4); Nittetsu Elex Co.] at Osaka University (Tsuchiyama *et al.*, 2002).

2.3 Results and discussions

2.3.1 Track morphology and projectile disruption

Figure 2.2 shows examples of the track morphologies after impact. The density or brightness of each image represents the column density of the target material. Therefore, the brightest part indicates some empty space along the projectile trajectory, whereas darker parts indicate higher-density regions. Two types of track morphology were observed. The first type, the "carrot" shape, is a thin, long track. The second, the "bulb" shape, is thick and short with tails. These track types were also observed for dust tracks in silica aerogel (Hörz *et al.*, 2006). The higher-density region is observed in the track behind the projectile after penetration for targets consisting of hollow glass beads, probably due to the crushed shell of the beads.

According to the X-ray transmission images, the projectile shot at the lowest impact velocity was nearly intact, whereas the others were not. In particular, the projectiles launched

Table 2.2: Shot conditions of the impact experiments

Target name	Target type	Projectile material	Impact velocity (km s^{-1})	Projectile size (mm)	Projectile mass (mg)
1102_2	fluffy94	Ti	2.64	1.0	2.44
1101_1	fluffy94	Ti	4.04	1.0	2.44
1101_3	fluffy94	Ti	6.74	1.0	2.44
1101_4c	fluffy94	Ti	3.92	1.0	2.44
1101_4a	fluffy94	Ti	3.63	1.0	2.44
1105_A	fluffy94	Al	7.17	1.0	1.45
1105_B	fluffy94	Al	4.28	1.0	1.45
1105_C	fluffy94	Al	2.44	1.0	1.45
1109_A	fluffy80	Ti	2.55	1.0	2.44
1109_B	fluffy80	Ti	4.25	1.0	2.44
1109_C	fluffy80	Ti	6.75	1.0	2.44
1109_D	fluffy80	Ti	1.69	3.2	75.4
1109_F	fluffy80	Basalt	2.52	D3.2 × H2.0	49
1109_G	fluffy80	Basalt	3.89	D3.2 × H2.0	51
1109_Z	fluffy94	Basalt	2.17	D3.2 × H2.0	59
1109_Y	fluffy94	Basalt	4.22	D3.2 × H2.0	51
1109_X	fluffy94	Basalt	6.63	D3.2 × H2.0	50
1111_A	fluffy94	Ti	6.37	3.2	75.4
1111_O	fluffy87	Ti	2.01	1.0	2.44
1111_P	fluffy87	Ti	4.28	1.0	2.44
1111_Q	fluffy87	Ti	6.76	1.0	2.44
1111_R	fluffy87	Ti	1.83	3.2	75.4
1111_T	fluffy87	Ti	4.26	3.2	75.0
1111_U	fluffy87	Ti	6.18	3.2	75.0
1201_A	fluffy94	Ti	2.26	3.2	75.4
1201_B	fluffy94	SUS	2.27	1.0	3.7
1201_C	fluffy94	Basalt	2.31	D3.2 × H2.2	45.2
1201_D	fluffy94	Basalt	3.28	D3.2 × H2.3	49.8
1201_O	fluffy87	SUS	2.18	1.0	3.7
1201_Q	fluffy87	SUS	2.26	1.0	3.7
1201_E	fluffy94	Basalt	1.94	D3.2 × H2.2	46.0
1204_G	fluffy94	Basalt	2.26	D3.2 × H2.2	46.0
1201_H	fluffy94	Basalt	2.30	D3.2 × H2.3	50.0

[a] Diameter for spherical projectiles; diameter (D) and height (H) for cylindrical projectiles.

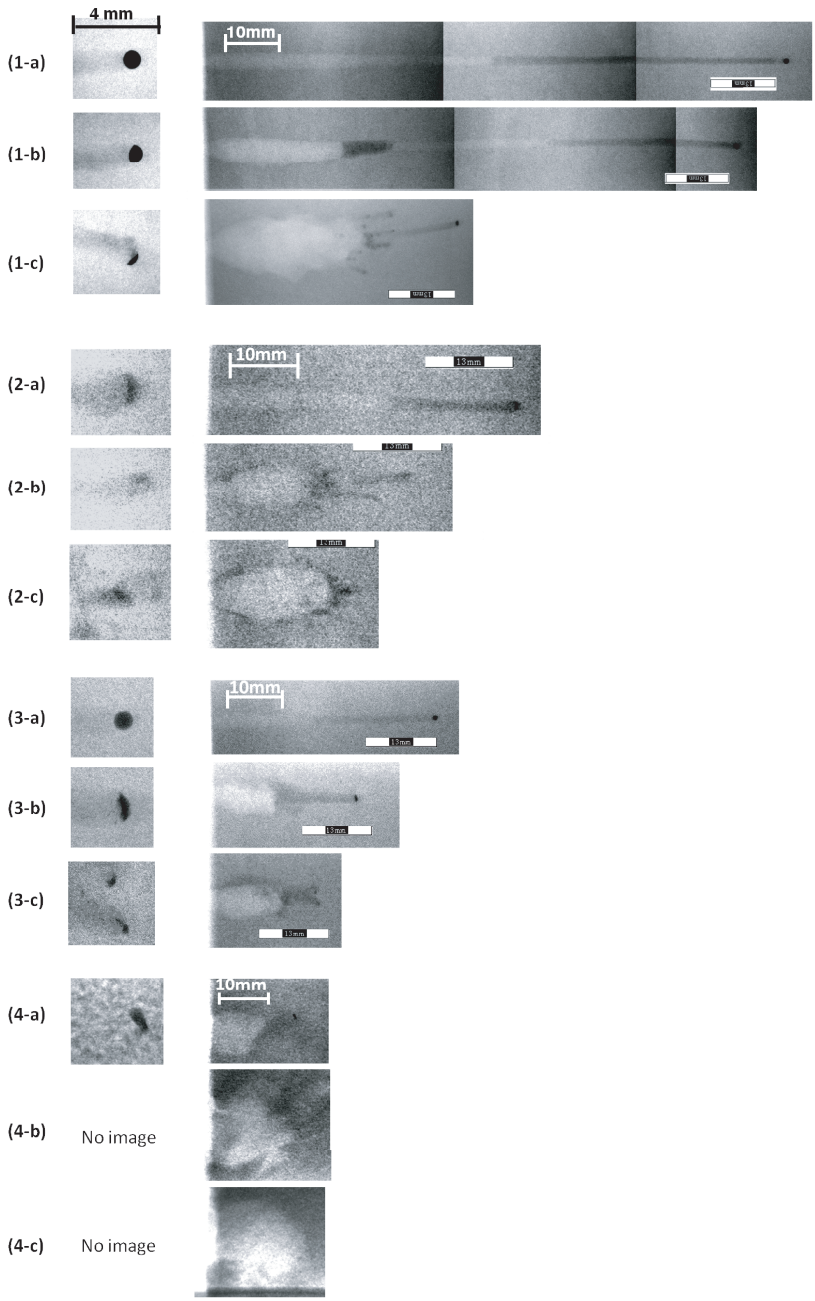

Figure 2.2: Transmission images of the targets for metal projectiles. (1) and (2): 94% porosity targets with titanium and aluminum projectiles, respectively; (3): 87% porosity targets with titanium projectiles; (4): 80% porosity targets with titanium projectiles. The impact velocities of (a), (b), and (c) were approximately 2.5, 4, and 7 km s^{-1}, respectively. Left: Terminal projectiles. The terminal projectile cannot be found in images (4-b) or (4-c) given the resolution of these images. Right: Projectile tracks. The tracks of images (1-a), (1-b), (2-a), and (3-a) are carrot-shaped; the others are bulb-shaped (see Figure 2.4).

at the highest impact velocity broke into a number of pieces. Housen and Holsapple (2003) showed that an area of high relative density was found below the crater center in a Computed Tomography (CT) image. Such an area was not observed in our transmission images. We excavated deformed or moderately disrupted terminal projectiles from the targets. These projectiles were covered by a thin layer of less porous glass beads. The tips of the projectiles had conical caps of less porous glass beads. When we scratched those parts using sandpaper, we could remove them almost entirely. We measured the diameter (d_L) and mass (m_L) of the excavated terminal projectiles. The diameter (d_L) was defined as the width of the projectile in the plane perpendicular to its symmetry axis. Since the shape of basalt projectiles were irregular, the diameter (d_L) was defined as the largest width of the projectile in the plane perpendicular to the symmetry axis of the conical cap. For nearly intact projectiles we used the measurement values of the X-ray transmission images. The results are summarized in Table 2.3. Figure 2.3 shows the relationship of the mass ratio of the terminal fragment to the initial projectile and the initial dynamic pressure, $\rho_t {v_0}^2$, where ρ_t and v_0 are the target density and impact velocity, respectively, normalized by the projectile ' s tensile strength, Y_{pt} = 320 MPa for titanium, 55 MPa for aluminum and 19.4 MPa for basalt (Kaye and Laby, 1986; Nakamura *et al.*, 2007). Projectile deformation starts at a dynamic pressure of 4–7 times the tensile strength of the projectiles. Projectiles seem to start to lose mass when the dynamic pressure becomes 10 times the projectile tensile strength, and projectiles are then heavily disrupted (terminal-fragment mass fraction < 0.5). The following regression line was obtained for all the data except for the two leftmost points:

$$\frac{m_L}{m_p} = 10^{1.5\pm0.7}\left(\frac{\rho_t v_0^2}{Y_{pt}}\right)^{-1.5\pm0.5} \tag{2.1}$$

The largest-fragment mass fraction becomes half of the original mass when the dynamic pressure becomes 16 times the projectile tensile strength.

The measured penetration depth and track morphology depend on the impact velocity

Table 2.3: Experimental results

Target name	Penetration depth (mm)	m_L/m_p	d_L/d_p	MW/PD	C_d
1102_2	116	1.0	1.0	0.030	—[d]
1101_1	112	0.84	1.1	0.055	—[d]
1101_3	52	0.32	1.1	0.28	—[d]
1101_4c	> 25	—[e]	—[e]	—[e]	1.55
1101_4a	> 46	—[e]	—[e]	—[e]	1.64
1105_A	22	—[f]	—[f]	0.38	—[d]
1105_B	31	—[f]	—[f]	0.19	—[d]
1105_C	47	1.07	1.4	0.074	—[d]
1109_A	18	—[f]	—[f]	—[g]	—[d]
1109_B	19	—[f]	—[f]	—[g]	—[d]
1109_C	21	—[f]	—[f]	—[g]	—[d]
1109_D	—[h]	—[h]	—[h]	—[h]	1.007±0.002[i]
1109_F	—[h]	—[h]	—[h]	—[h]	2.85±0.06
1109_G	—[h]	—[h]	—[h]	—[h]	3.09±0.11
1109_Z	> 128	—[e]	—[e]	—[e]	1.23±0.17
1109_Y	—[j]	—[j]	—[j]	—[j]	3.43±0.05
1109_X	—[h]	—[h]	—[h]	—[h]	3.54±0.02
1111_A	—[h]	—[h]	—[h]	—[h]	1.52±0.29
1111_O	42	1.0	1.0	0.065	—[d]
1111_P	28	1.0	1.4	0.27	—[d]
1111_Q	21	—[f]	—[f]	0.38	—[d]
1111_R	> 102	—[e]	—[e]	—[e]	0.80±0.02[i]
1111_T	—[h]	—[h]	—[h]	—[h]	2.00±0.37
1111_U	—[h]	—[h]	—[h]	—[h]	2.78±0.08
1201_A	> 138	—[e]	—[e]	—[e]	1.41[i]
1201_B	> 137	—[e]	—[e]	—[e]	1.03[i]
1201_C	132	0.08	0.4	0.11	2.15±0.43
1201_D	—[j]	—[j]	—[j]	—[j]	2.61±0.16
1201_O	71	1.0	1.0	0.040	—[d]
1201_Q	74	1.0	1.0	0.037	—[d]
1204_E	> 139	—[e]	—[e]	—[e]	1.59±0.08
1204_G	134	0.12	0.5	0.12	2.03±0.08
1204_H	> 137	—[e]	—[e]	—[e]	1.90±0.06

[a]Ratio of terminal-fragment to initial projectile mass. The measurement error is several percent.
[b]d_L/d_p: Ratio of terminal to initial projectile diameter. The measurement error is a few tens of percent.
[c]MW, PD: Maximum width, penetration depth of the tracks.
[d]No flash X-ray images obtained.
[e]Penetration depth or terminal projectile mass could not be measured because the projectile passed through the target.
[f]Terminal projectile was not identified on the X-ray transmission image.
[g]Track profile could not be obtained because X-ray transmission image was not clear.
[h]Penetration depth or terminal projectile mass could not be measured because the target was broken by the impact.
[i]Used for C_d derivation (see text).
[j]Penetration depth or terminal projectile mass could not be measured because the target broke during analysis.

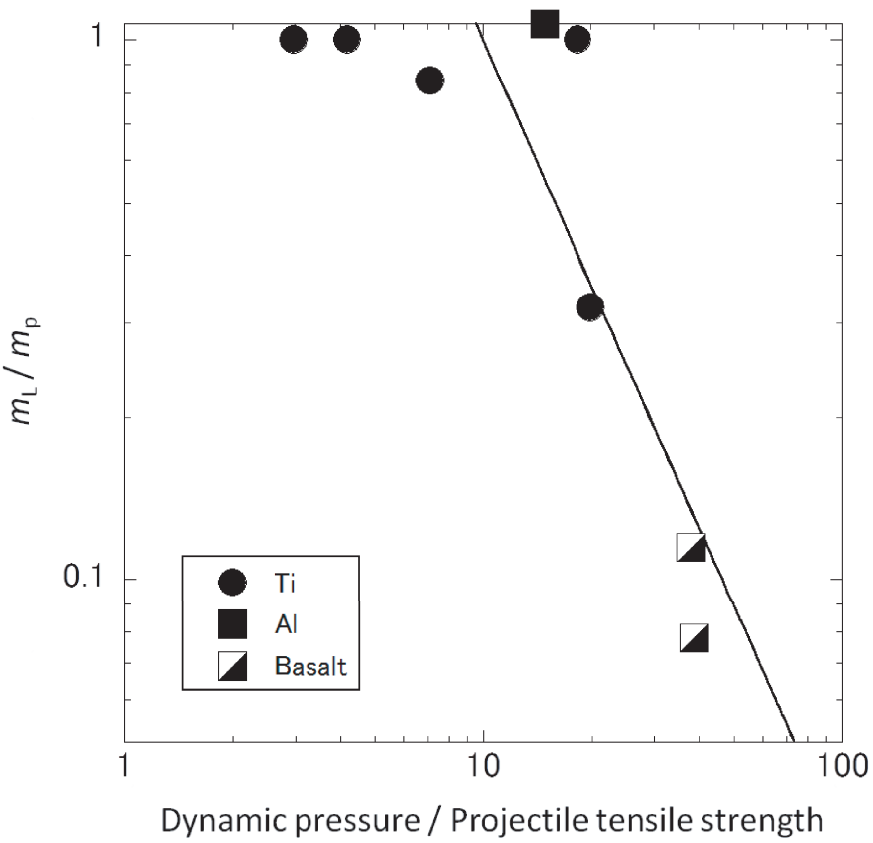

Figure 2.3: Normalized terminal-fragment mass versus normalized dynamic pressure. The line is a fit to six data points for deformed or disrupted projectiles with dynamic pressure/projectile tensile strength > 6

and the bulk porosity of the targets. Let us discuss the results of shots using a 1 mm titanium projectile. Carrot tracks formed in the fluffy94 targets at impact velocities of 2.6 and 4.0 km s^{-1}, as shown in Figure 2.2-(1-a) and 2.2-(1-b). The projectile was eroded in the 4.0 km s^{-1} shot and the track length was shortened. At an impact velocity of 6.7 km s^{-1}, the projectile was disrupted because of the initial peak pressure. A bulb track formed instead of a carrot track, and the penetration depth was much shorter, as shown in Figure 2.2-(1-c). At some fixed impact velocity, the projectile was more damaged in less porous targets and a shorter penetration occurred. For example, the projectile in the fluffy87 target was more damaged than that in the fluffy94 target, at roughly 4 km s^{-1} impact, and the penetration depth was shortened, resulting in a bulb-shaped track.

Burchell *et al.* (2008) indicated that the ratio of maximum track width (MW) to penetration depth (PD), MW/PD, is informative as regards the track types. They classified carrot-shaped tracks as those with $MW/PD < 0.11$, and bulb-shaped tracks as those with a MW/PD ratio of > 0.11. Figure 2.4 shows the relationship between the MW/PD ratio and the initial dynamic pressure, normalized by the projectile's tensile strength. We also plotted the results of various projectiles into aerogel, as obtained in previous studies (Burchell *et al.*, 2008; Hörz *et al.*, 2009; Kearsley *et al.*, 2012; Niimi *et al.*, 2012), using the tensile strength of soda-lime glass, copper (60 MPa, 195 MPa, respectively; Kaye and Laby 1986), alumina (258 MPa; Shackelford and Alexander, 2000), carbonaceous chondrite meteorites ($\leq 37, \leq 14, \leq 14$ MPa for Allende, Murchison, Orgueil, respectively; Tsuchiyama *et al.*, private communication, 2012), and graphite (10.9 MPa; Manhani *et al.*, 2007). The MW/PD ratio increases with increasing dynamic pressure. The transition between "carrot" and "bulb" occurs at a pressure of approximately 20 times the projectile's tensile strength. The data points to the right of this boundary in Figure 2.4 have MW/PD values equal to or greater than 0.11, which is in agreement with the criterion for morphological classification (Burchell *et al.*, 2008). The data of the Murchison projectile are also consistent with

the tendency of this figure, although it has been suggested that evaporation of the volatile component may play a role in the formation of bulb-shaped tracks (Hörz *et al.*, 2006). The results here suggest that projectile disruption is more important for track-shape formation.

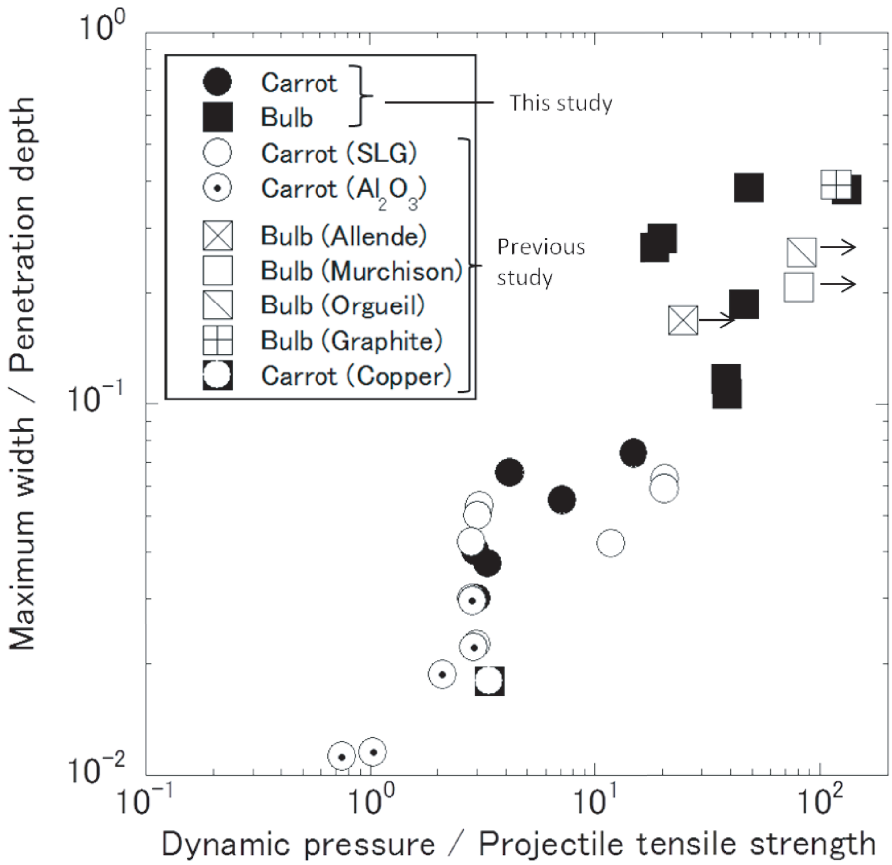

Figure 2.4: Correspondence of the MW/PD ratio and the normalized initial dynamic pressure. Projectile material is denoted in parentheses. SLG: Soda-lime glass.

2.3.2 Compaction

Compacted region by impact can be identified on flash X-ray images. Figure 2.5 is the image of a shot of a 3.2 mm-diameter titanium projectile into fluffy87 at 6.18 km s^{-1} (1111_U) taken at the time 4.54 μs after impact. We analyzed this image in order to determine the density of compacted region. Inhomogeneity in the brightness was observed

on the image. For example, Figure 2.5 (b) shows that there were some brighter parts (A, C) and some darker parts (B, D), though there were no obstacles in the path of the flash X-ray. This may be due to the differences in initial X-ray intensities toward different directions or/and in sensitivity of the imaging plate. In order to correct this inhomogeneity, a flat field correction described in the following was carried out. X-ray intensity decays through objects and it is expressed as following equation:

$$I = I_0 \exp\left(-\mu_{\mathrm{X}} \rho_{\mathrm{t}} l\right), \tag{2.2}$$

where I, I_0, μ_{X}, and l are weakened X-ray intensity, initial X-ray intensity, X-ray absorption coefficient, and length for X-ray passing through an object, respectively. Brightness value on the image, B, is expressed as $B = \mathrm{k}I$, where k is a coefficient representing the sensitivity. Note that coefficient, k here, is different constant for each pixel. Thus the relation between brightness values that we obtained and X-ray intensity is

$$B = \mathrm{k}I = \mathrm{k}I_0 \exp\left(-\mu_{\mathrm{X}} \rho_{\mathrm{t}} l\right). \tag{2.3}$$

First we picked out brightness values of 5 columns (two from in front of the impact side of the target, three from behind the back side of the target) in order to determine $\mathrm{k}I_0$. Brightness values for each column were fitted by a fifth degree polynomial as a function of row numbers . Six fitting coefficients could be obtained for each column, then we fitted the coefficients versus column numbers by linear fits. Thus we could calculate the brightness of the originally streaky pattern for each pixel, kI_0. Dividing the brightness value for each pixel of the flash X-ray image, B by $\mathrm{k}I_0$, the pattern was corrected. The image after the flat field correction is shown in Figure 2.6.

Figure 2.7 shows $B/\mathrm{k}I_0$ versus column density. The X-ray absorption coefficient, μ_{X}, was determined from the data fitting using the relation of Eq.(2.3). Assuming the density of compacted region, ρ_{t}', is uniform, the brightness values in the region are expressed as

follows:

$$B = \mathrm{k}I_0 \exp\{-\mu_\mathrm{X}(\rho_\mathrm{t} l_1 + \rho_\mathrm{t}' l_2)\}, \tag{2.4}$$

where l_1 and l_2 are the lengths of the regions with the initial target density and the compacted, respectively. Using Eq. (2.4), density of the compacted region was calculated as well as density of non-compacted region, and shown in Figure 2.8. The average density of compacted region was obtained to be $(6.1 \pm 2.4) \times 10^2$ kg m^{-3}.

The total mass of the compacted region was calculated by $\rho_\mathrm{t}' V_\mathrm{comp}$, where V_comp is the total volume of the compacted region, which was obtained by integrating the area of circular ring of the compacted region. The width of the circular ring was assumed to be a constant value of 1.5 mm. Figure 2.9 shows the comparison of the total mass of the compacted region 4.54 μs after impact with the original mass of the region that subsequently formed the cavity and the compacted region. The latter mass is calculated by $\rho_\mathrm{t}(V_\mathrm{cav}+V_\mathrm{comp})$, where V_cav is the volume of cavity. It was found that the almost all materials existed in cavity part was transported to the compacted region. This corresponded that little ejecta was observed by the high-speed camera.

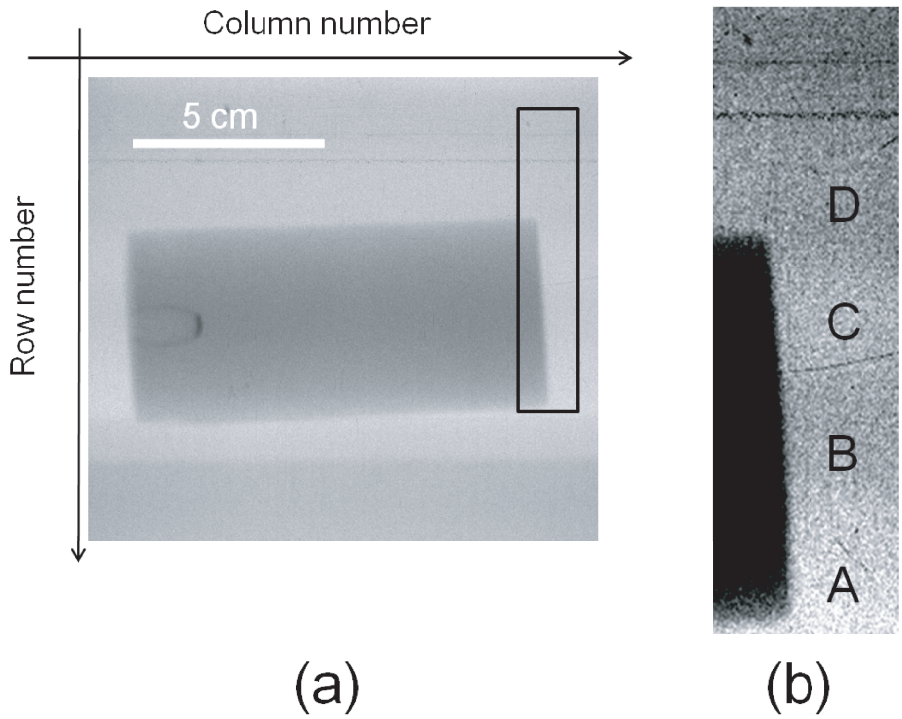

Figure 2.5: Flash X-ray images of a shot into 1111_U taken at the time 4.54 μs after impact. (a) Original flash X-ray image of the shot. Darker region below the target is due to the ceiling of the target box. (b) Contrast-enhanced image of the rectangle zone of (a). Inhomogeneity was observed on the image. For example, A and C are brighter, whereas B and D are darker.

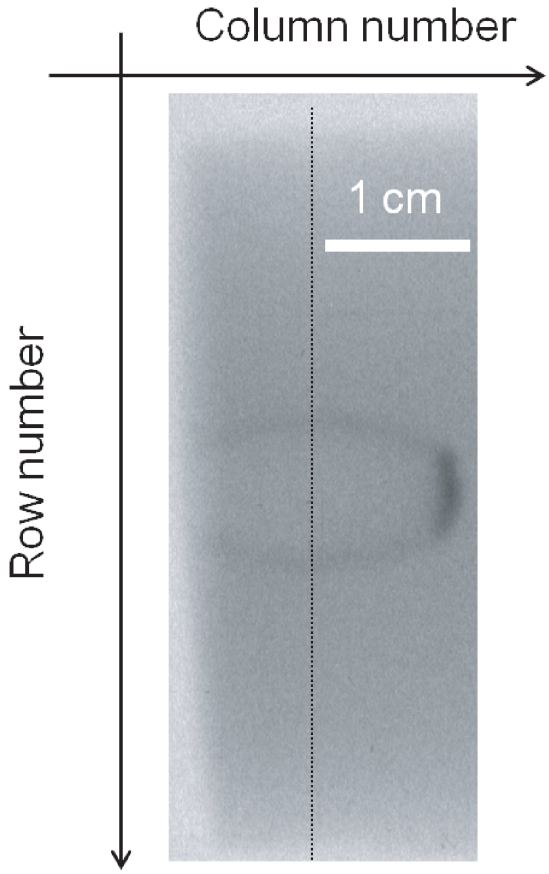

Figure 2.6: A flash X-ray image after the correction of inhomogeneity in the brightness. Dotted line is the column which we analyzed.

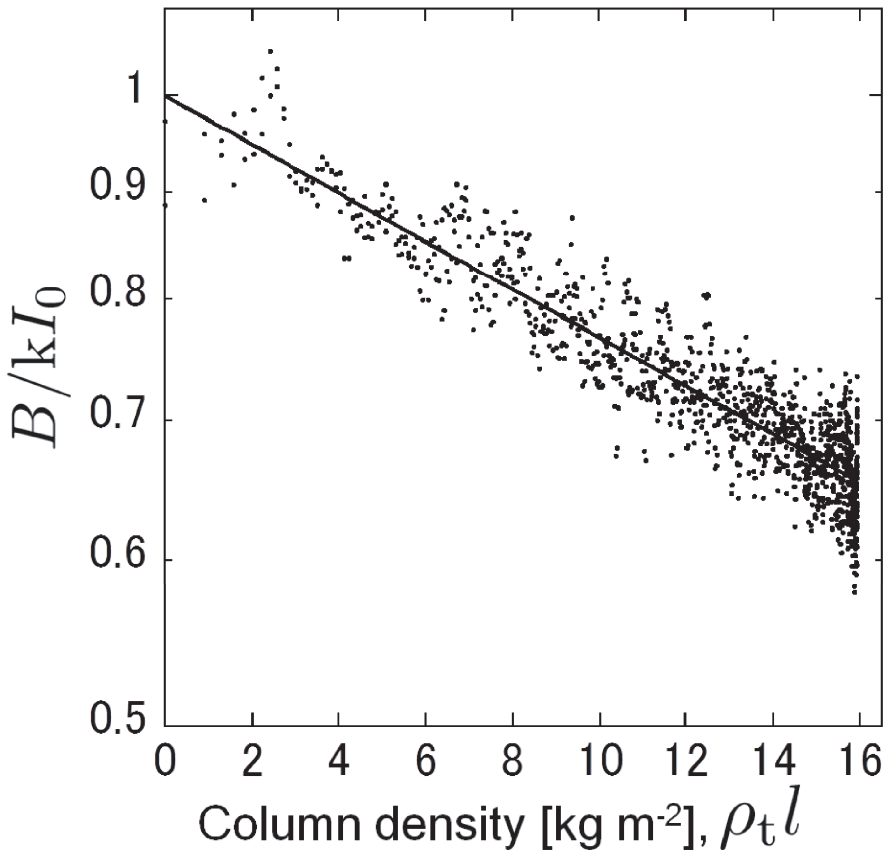

Figure 2.7: $B/\mathrm{k}I_0$versus column density. The solid line shows the regression line fitted by Eq. (2.2).

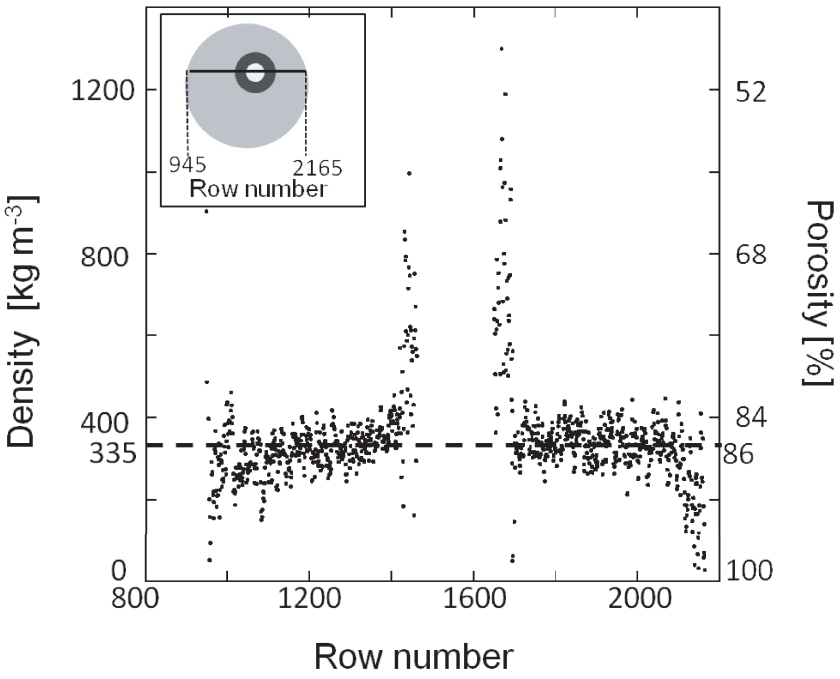

Figure 2.8: Calculated density versus row number. Dashed line shows the density and porosity of the initial target. The inserted illustration shows the calculated column; Light gray, dark gray, and open circle show the target of the original density, the compacted region, and the cavity region, respectively. The numbers show the row numbers of the edges of the target in the column.

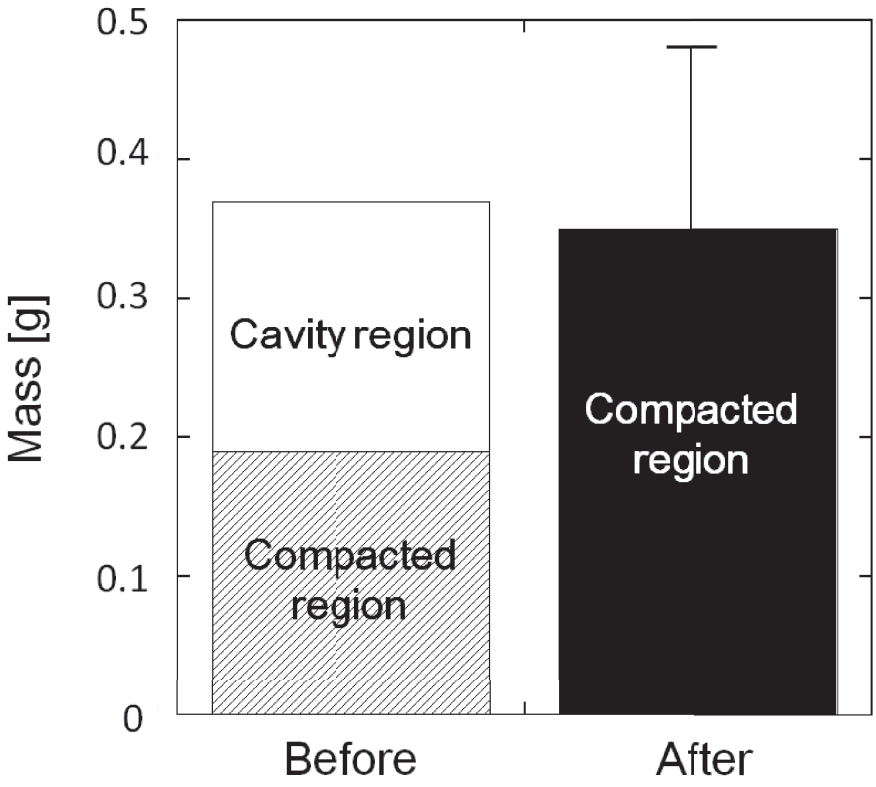

Figure 2.9: The comparison of the mass of the compacted region 4.54 μs after impact with the original mass of the region that subsequently formed the cavity and the compacted region.

2.3.3 Projectile deceleration

The track shapes of the sintered glass-bead targets were similar to those for aerogel targets. Thus, we assumed that the deceleration process of projectiles in porous sintered glass beads was similar to that in the aerogel targets studied previously (Niimi *et al.*, 2011). Given a high-velocity projectile, inertial resistance is dominant, and other forms of resistance can be neglected. Consequently, the equation of motion for a penetrating projectile is given by

$$m_{\mathrm{p}}\frac{\mathrm{d}v}{\mathrm{d}t} = -\frac{1}{2}C_{\mathrm{d}}\rho_{\mathrm{t}}S\,v^2, \tag{2.5}$$

where $m_{\mathrm{p}}, v, C_{\mathrm{d}}$, and S are the projectile mass, projectile velocity, drag coefficient, and projectile cross-section, respectively. Penetration depth, $x(t)$, as a function of time, is derived by integrating Eq. (2.5),

$$x(t) = \frac{1}{\alpha}\ln(\alpha v_0 t + 1), \tag{2.6}$$

$$\alpha = \frac{C_{\mathrm{d}}\rho_{\mathrm{t}}S}{2m_{\mathrm{p}}}, \tag{2.7}$$

where t is the time from the collision between the projectile and the target. Using Eq. (2.6), we fit the experimental data obtained from the flash X-ray images shown in Figure 2.10 by leaving α as a free parameter. After determining α, the drag coefficient C_{d} was calculated from Eq. (2.7)—listed in Table 2.3—and plotted versus initial dynamic pressure, normalized by the projectile's tensile strength in Figure 2.11. Note that C_{d} for two shorter targets (1101_4c and 1101_4a) was determined using high-speed video-camera images in which the projectiles' penetration was observed. Also note that the cross-section, S, and the projectile mass, m_{p}, in Eqs (2.5) and (2.7) were assumed to be constant as the projectiles' initial values, although changes in S and m_{p} were observed in the experiments.

Figure 2.11 shows that the drag coefficient increases with normalized initial dynamic pressure. The increase in C_{d} is caused by the increase in α, because we assumed that the other parameters remained constant. However, the increase in α is probably owing to

the change in projectile mass and shape when projectile deformation starts at a dynamic pressure of 4–7 times the tensile strength of the projectiles as described in Section 2.3.1. Yasui *et al.* (2012) also suggested that deformation and disruption of the original projectile may cause higher drag coefficient C_d. It could also be due to an increase in target density in front of the projectile, which was observed as conical caps of less porous glass beads (described in the previous section). That is, the increase in C_d in Figure 2.11, along with the initial dynamic pressure, indicates an increase in the term $\rho_\mathrm{t} S/m_\mathrm{p}$ in Eq. (2.7). The drag coefficient was determined as 1.1 ± 0.3 based on four shots in which the projectiles were nearly intact (marked in Table 2.3). This value is similar to the result of Niimi *et al.* (2011), who reported $C_\mathrm{d} = 1.1 \pm 0.1$. Note that the assumption of constant S and m_p is unphysical, because they should change because of fragmentation at high dynamic pressure as discussion in 3.3.2. Nevertheless, our analysis provides the "effective drag coefficient" for broken projectiles during penetration. In such cases, the effective drag coefficient reaches higher values.

We constructed a simple model for projectile deceleration and penetration depth for projectiles that did not experience severe deformation and fragmentation based on the experimental results, as follows. When a projectile collides with a target, the projectile loses mass at the impact point because of the high initial pressure. The remaining projectile then penetrates into the target according to the following equation, a modification of the equivalent equation of Niimi *et al.* (2011),

$$m_\mathrm{L} \frac{\mathrm{d}v}{\mathrm{d}t} = -\frac{1}{2} C_\mathrm{d} \rho_\mathrm{t} S_\mathrm{L} v^2 - S_\mathrm{L} Y_\mathrm{c}, \tag{2.8}$$

where m_L and $S_\mathrm{L} = (\pi {d_\mathrm{L}}^2)/4$ are the mass and cross-section of the terminal projectile, respectively, and Y_c is the target's compressive strength. The penetration depth was assumed to be determined by the size of the largest fragment. Eq. (2.8) can be integrated and the penetration depth, normalized by the diameter of the largest fragment, is derived

as follows, if the largest fragment is assumed to be a sphere (Kadono and Fujiwara, 2005):

$$\frac{PD}{d_{\mathrm{L}}} = \frac{2}{3}\frac{\rho_{\mathrm{p}}}{C_{\mathrm{d}}\rho_{\mathrm{t}}}\ln\left(1 + \frac{C_{\mathrm{d}}\rho_{\mathrm{t}}{v_0}^2}{2Y_{\mathrm{c}}}\right). \tag{2.9}$$

We used the values of d_{L} and m_{L} of the terminal projectile in Table 2.3 and Eq. (2.8)—not Eq. (2.9), because the excavated projectiles were deformed from spheres—to estimate the penetration depth for projectiles that did not experience severe deformation and fragmentation. The estimated penetration depth is compared with the experimental data in Figure 2.12. We used the compressive strength of the weaker part of the targets as Y_{c}, because all projectiles penetrated deeper than the stronger part. The error bars reflect the uncertainty in the drag coefficient. Figure 2.12 shows that the estimate reproduces the experimental data well.

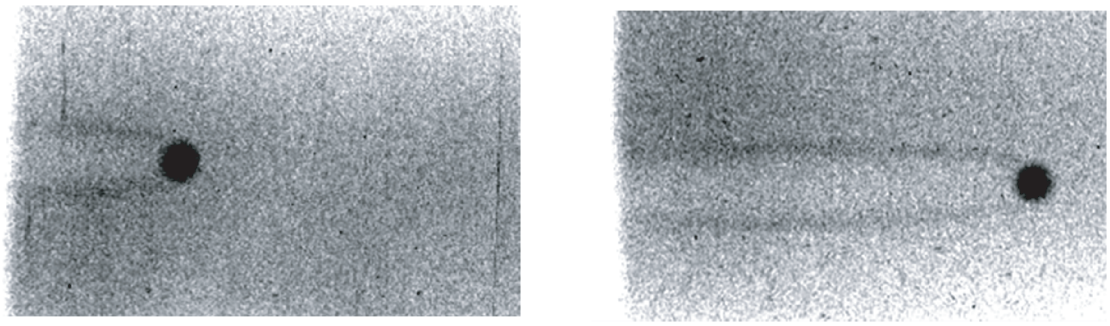

Figure 2.10: Flash X-ray images of a shot of a 3.2 mm-diameter titanium projectile into fluffy87 at 1.8 km s^{-1} (1111_R). Elapsed time from impact is 11.0 μs for the left-hand and 30.9 μs for the right-hand image. The projectile was neither deformed nor disrupted in this shot.

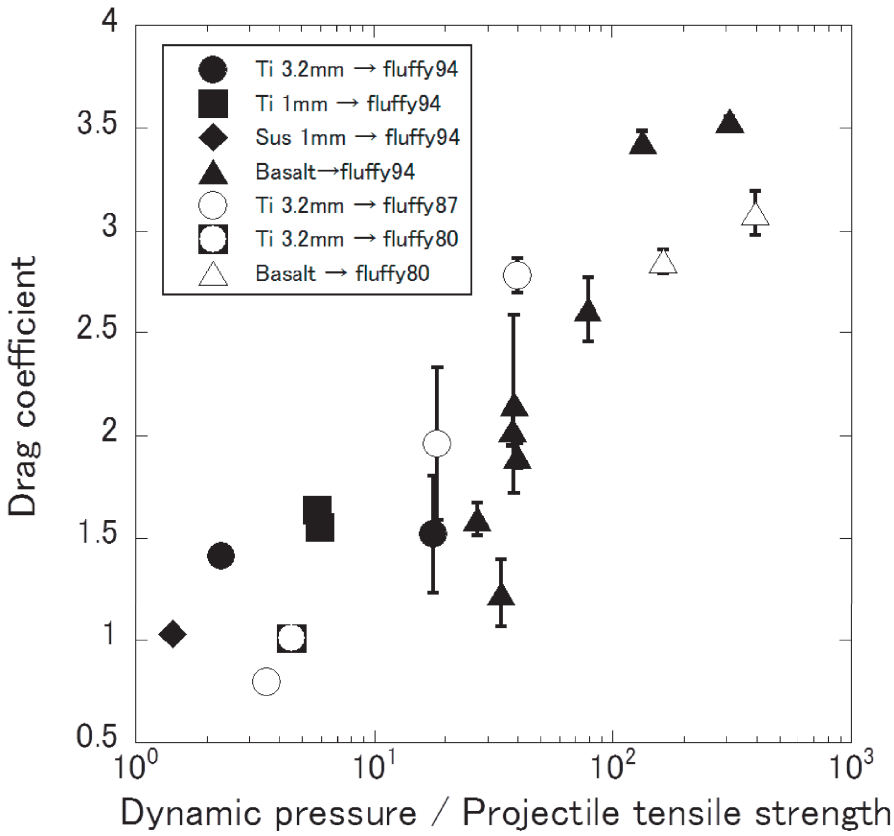

Figure 2.11: Drag coefficient versus normalized initial dynamic pressure.

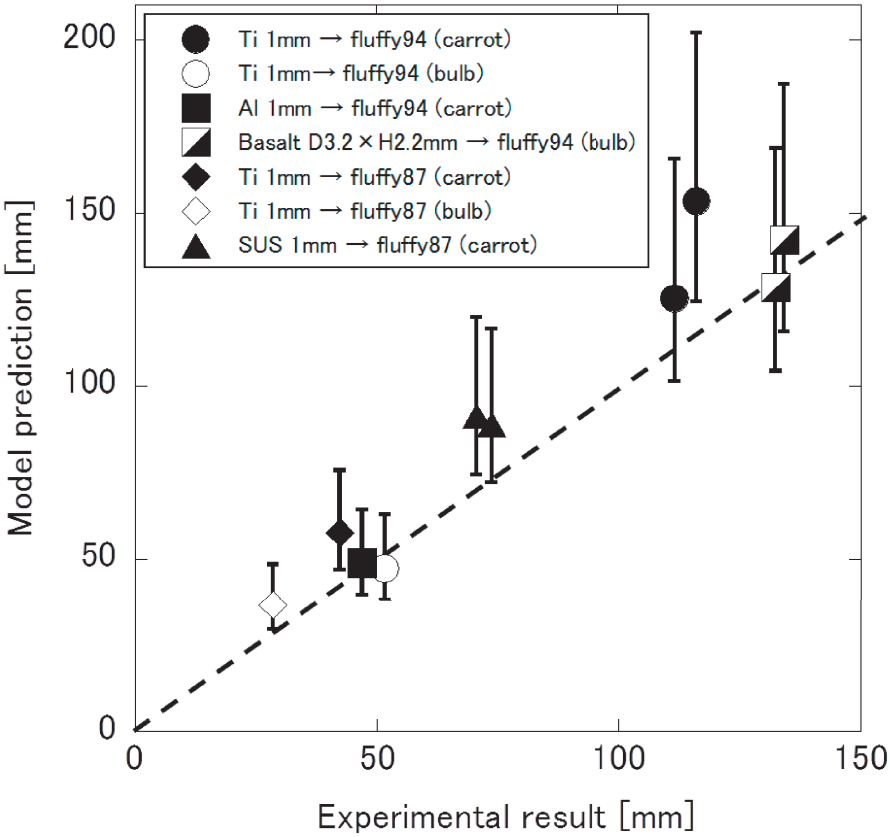

Figure 2.12: Comparison of the estimated penetration depth and the experimental results. The dashed line shows a reference where both are in agreement.

2.3.4 Implication for dust penetration into icy bodies

We applied this penetration model to tracks formed by the penetration of silicate dust grains into icy bodies orbiting in the Kuiper Belt region. According to Eqs (2.1) and (2.9), we can calculate the penetration depth of the projectile,

$$\frac{PD}{d_{\mathrm{p}}} = \frac{d_{\mathrm{L}}}{d_{\mathrm{p}}}\frac{PD}{d_{\mathrm{L}}}, \tag{2.10}$$

and

$$\frac{d_{\mathrm{L}}}{d_{\mathrm{p}}} = \left(\frac{m_{\mathrm{L}}}{m_{\mathrm{p}}}\right)^{\frac{1}{3}} = \min\left(1, \left\{10^{1.5\pm0.7}\left(\frac{\rho_{\mathrm{t}}{v_0}^2}{Y_{\mathrm{pt}}}\right)^{-1.5\pm0.5}\right\}^{\frac{1}{3}}\right). \tag{2.11}$$

Here we use Eq. (2.9) and not Eq. (2.8), because dust particles would not be deformed like metal projectiles, as in the present experiment. Therefore, we assumed that the disrupted dust can be approximated by a sphere. Although we applied the present result to the relationship between the degree of fragmentation of the projectile and the dynamic pressure, normalized by the projectile's tensile strength, this relationship may be dependent on the size of the projectile and the impact velocity (Housen and Holsapple, 1999). We assumed that the grain density of the constituents of icy bodies is 1600 kg m^{-3}. This value matches the smallest well-measured icy dwarf planet, Pluto's moon Charon, which presumably is large enough to have zero macro-porosity but small enough to avoid significant internal compression (Consolmagno *et al.*, 2008). Greenberg (1998) also proposed a similar value, 1650 kg m^{-3}, as the maximum mean density of a fully packed comet nucleus. The compressive strength of icy bodies for a range of porosities is assumed as follows, based on previous uniaxial strength tests of dry snow. We derived an empirical equation from the measurement results of strength as a function of bulk porosity (see fig.17 in Mellor, 1974),

$$Y_{\mathrm{c}} = Y_{\mathrm{c,snow}} = 8.8\left(1 - \frac{\phi}{100}\right)^{4.4} = 8.8 f^{4.4}[\mathrm{MPa}], \tag{2.12}$$

where $Y_{\mathrm{c,snow}}$ is the compressive strength of dry snow and ϕ is the bulk porosity. This equation can be applied to a bulk porosity ranging from 60% to nearly 100%. The crushing

strength of comet nuclei ranges from 10^3 to 10^5 Pa (Öpic, 1966). The compressive strength of dry snow adopted here with a porosity of 70–90% is within this range. It is also in agreement with the modeled compressive strength of grain aggregates (Sirono, 2000).

The result of this calculation for impacts with relative velocities of up to 1000 m s^{-1} (Farinella and Davis, 1996) for dust with the mechanical properties of basalt, i.e., a density of 2700 kg $m^{-3}$and a tensile strength of 19.4 MPa (Nakamura *et al.*, 2007), is shown in Figure 2.13. This figure shows the penetration depth at each impact velocity versus the bulk porosity of the bodies, which are homogeneous on a much smaller scale than the impacting dust particles. The penetration depth increases with increasing bulk porosity of the target body. For bodies of order 90% bulk porosity, the penetration depth is approximately 100 times the projectile diameter.

Wild 2 probably experienced multiple outer planet perturbations that transferred Wild 2 from beyond Neptune to JFC orbits. The period of this migration is typically a few million years (Levison and Duncan, 1997). During the active period of typical JFC comets, the radii shrink by at least 25% (Thomas, 2009). If Wild 2 is roughly halfway through its JFC lifetime in the inner solar system, it should have lost over 200 m of its original surface (Brownlee *et al.*, 2012). The size of dust captured by the Stardust mission which is considered to be lifted from the comet surface by gas drag ranged from submicron to several hundred microns (Brownlee *et al.*, 2012). The corresponding penetration depth of such dust particles is at most several centimeter as shown in Figure 2.13. With the shallow penetration depth, dust particles captured at recent inner orbit would have been lost as the gas evaporated from the surface. Thus the dust particles that contain high-temperature objects may be original components which formed the comet in Kuiper belt at the accretion stage, rather than captured dust at inner region after the comet became JFC. Outward transport of the high-temperture objects at the accretion stage would have been due to X-wind, which has been modeled by Shu *et al.* (1996, 2001), or processes

involving turbulent diffusion and instabilities (e.g. Bockelee-Morvan *et al.*, 2002; Ciesla, 2007; Cuzzi *et al.*, 2008).

Much larger impactors may have been captured by high-porosity bodies at greater depths from the surface and stored for longer times.

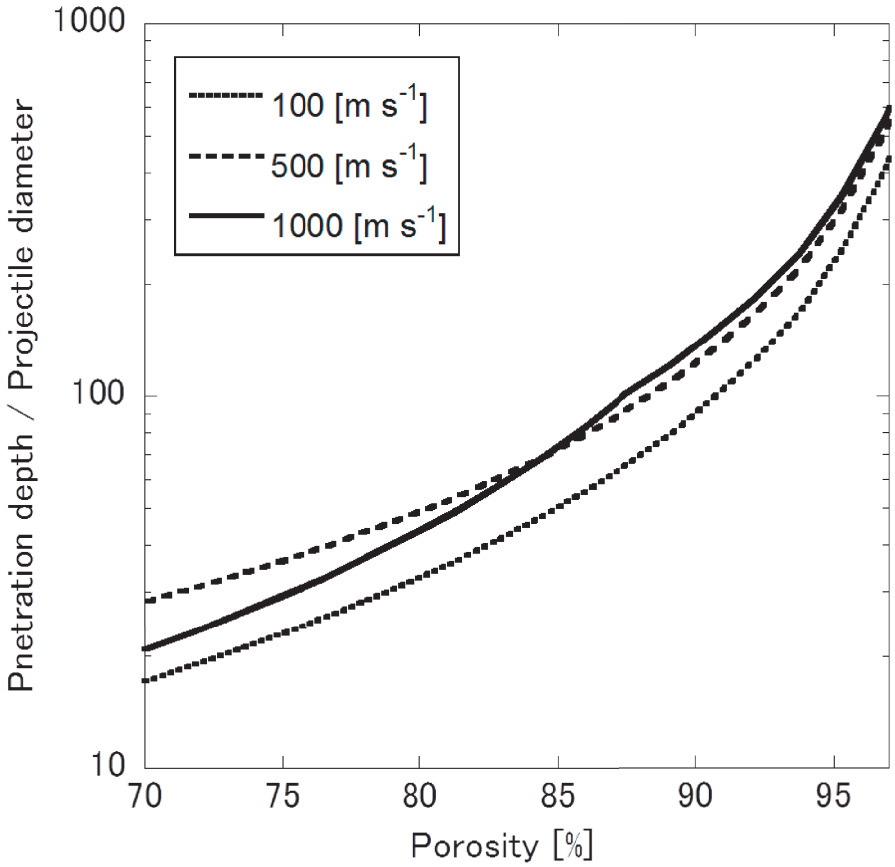

Figure 2.13: Estimation of penetration depth versus porosity of icy bodies.

2.4 Summary

We sintered glass beads under different conditions and prepared porous targets with 94%, 87%, and 80% bulk porosity. Impact-penetration experiments were conducted using a two-stage light-gas gun at ISAS/JAXA. The projectiles were metal spheres and basalt cylinders. Impact velocities ranged from 1.6 to 7.2 km s^{-1}. A flash X-ray imaging system and a high-speed video camera were used to observe projectile deceleration processes. We also used micro-X-ray tomography for analysis of the track morphologies. Two types of track morphologies were observed, similar to the dust tracks in silica aerogel blocks. The first type, a thin, long "carrot"-shaped track, occurs when the projectile remains almost intact. The second type, which is thick and short with tails ("bulb" shape), occurs when the projectile is disrupted. The transition from carrot to bulb shape occurs when the initial dynamic pressure exceeds approximately 20 times the projectile's tensile strength. The compacted region due to impact was observed on images. The average density of the compacted region was calculated to be $(6.1\pm2.4)\times10^2$ kg m^{-3} for the targets 1111_U, which had originally the density of 3.35×10^2 kg m^{-3}. It was found that the almost all material existed in cavity part was transported to the compacted region. We derived an equation of motion for the largest fragment of a projectile during penetration into highly porous bodies. This model roughly reproduces the experimental results with respect to penetration depth for projectiles that did not experience severe deformation and fragmentation. We applied this penetration model to icy bodies which were homogeneous on much smaller scales than the impacting dust particles with different bulk porosities and estimated the penetration depth of silicate dust. The predicted depth showed that the dust penetration was only approximately 100 times the projectile diameter, even for bodies with 90% bulk porosity.

Chapter 3

Experimental study of cavity morphology of highly porous targets[*1]

3.1 Introduction

In the history of the solar system, small bodies were probably characterized by very high porosities as described in Section 1.2 and 2.1. Craters on small bodies have been observed by spacecrafts. Craters on icy bodies are different from the impact craters on asteroids and the Moons.

Crater-like features was detected on the nuclei of comet Tempel 1, with diameters of as large as a few hundred meters (Thomas *et al.*, 2007a). They are flatter than the impact craters of similar sizes seen on asteroids and the Moons (Vincent *et al.*, 2014). The Cassini spacecraft took the images of the surface of Hyperion, which is a satellite of Saturn. The image shows that Hyperion is sponge-like appearance, which is characterized by the reticulate, honeycomb pattern of narrow divides between craters (Thomas *et al.*, 2007b). A lot of craters on Hyperion have dark surfaces in the floors. (Thomas *et al.*, 2007b). The depth-to-diameter ratio is slightly larger than that of the Moon, 0.295 (White and Schenk, 2011).

[*1] An earlier version of this chapter has been published as:
Okamoto T., Nakamura A. M., and Hasegawa S. 2014. Impact Experiments on Highly Porous Targets: Cavity Morphology and Disruption Thresholds in the Strength Regime. *Planetary and Space Science, in press*

Howard *et al.* (2012) proposed that the unique appearance of Hyperion is caused by slope erosion governed by diffusive mass wasting induced by sublimation. The dark surfaces in the floors of the craters were interpreted to be lag deposits of contaminants left behind by sublimation of the surround in ice (Cruikshank *et al.*, 2007; Howard *et al.*, 2012). On the other hand, Thomas *et al.* (2007b) proposed that the craters on Hyperion could be explained by the loss to space of ejecta during impact events. They estimated H_2O sublimation rates at Saturn's distance from the Sun, and it shows that water ice will sublimate much less than 10 m over the period of existence of the solar system so far, even allowing for some concentration of incident radiation at the bottom of depressions. This value is much smaller than the observed craters (the Cassini imagery :180 m/pixel, Brad *et al.*, 2012). Thus they concluded that primary impact crater morphology rather than sublimation explains the unusual appearance of Hyperion.

Whether these craters could be formed by impact only has not been examined in detail. The characteristic physical properties of surface such as low density, high porosity and weak strength may influence on the crater formation. In this study, we focus on craters of porous bodies in strength regime, and discuss what kind of crater morphologies is formed on such surface.

Previous laboratory experiments have been conducted using porous targets such as gypsum, sintered glass-bead, pumice, and foamed polystyrene with high velocity of order of km s^{-1}. Love *et al.* (1993) and Michikami *et al.* (2007) used sintered glass-bead targets with porosities of up to 60% and 80%, respectively, and showed that the crater depths increased with increasing porosity of the target. However the results are not compared among the different materials. Thus using the data of our high-velocity impact experiments and the data of previous studies, we conducted scaling analyses of dimensions, i.e., diameter and depth of cavity formed in the targets with various porosities for estimating the crater dimensions on the surface of the porous bodies.

3.2 Experiments

We prepared sintered hollow glass-bead targets with porosities, ϕ, of 87% and 94%, which we refer to as fluffy87 and fluffy94, respectively as described in Section 2.2.1. As well as these targets, we prepared sintered glass-bead targets with porosities of 93%, which have uniaxial compressive strength one order of magnitude smaller than that for fluffy94; thus we refer to it as weak_fluffy93[*2]. Gypsum with porosities of about 50% and pumice with porosities of about 74% were also prepared. We mixed water and hemihydrate gypsum ($CaSO_4 \cdot 1/2H_2O$) powder in a 0.67 : 1 mass ratio. The mixed slurries were dried in an oven at 60 °C. Pumice targets were cut from blocks of natural pumice (originating from Ito ignimbrite from Aira caldera, Japan). Sintered glass-bead targets and gypsum targets were cylindrical in shape whereas pumice targets are irregular in shape. Table 3.1 shows a summary of the target properties; target dimensions are listed in Table 3.2. Uniaxial compressive strengths of the sintered glass-bead targets were measured using a compressive testing machine at Kobe University (Japan). The details of target preparation and strength measurement are described in Section 2.2.1.

Impact experiments were conducted using a two-stage light-gas gun at the Institute of Space and Astronautical Science (ISAS), Japan. A split-type nylon sabot (Kawai *et al.*, 2010) was used to accelerate projectiles of different types. The projectiles were titanium (4.5 g cm^{-3}), aluminum (2.7 g cm^{-3}), nylon (1.1 g cm^{-3}), and polystyrene (1.1 g cm^{-3}) spheres with diameters of 1 mm or 3.2 mm and basalt (2.7 g cm^{-3}) cylinders with a diameter of 3.2 mm and height of 2 mm. The impact velocities ranged from 2.3 to 7.2 km s^{-1}. Table 3.2 summarizes the impact conditions. The track profiles were observed and analyzed using transmission images obtained with a micro-X-ray tomography instrument

[*2]For weak_fluffy93, hollow glass-beads in a mold with aluminum circular cylinder of thickness of 3 mm and alumina top and bottom plates, had been heated from room temperature to the peak temperature of 630 °C in 6 hours, whereas they were cooled in the closed oven after the heater was switched off which takes roughly a day.

(ELE-SCAN NX-NCP-C80-I (4); Nittetsu Elex Co.) at Osaka University, now moved to Kyoto University (Tsuchiyama *et al.*, 2002) and a micro-X-ray CT scanner (MicroXCT-400; Xradia Inc.) at Hyogo Prefectural Institute of Technology. The results of the experiments are also presented in Table 3.2.

Table 3.1: Physical properties of porous targets investigated in the present and also previous studies.

Material	Type	Bulk density ($g\ cm^{-3}$)	Compressive strength stronger part (MPa)	Compressive strength weaker part (MPa)	Porosity (%)
Sintered glass beads[a]	fluffy94	0.140±0.004	0.47± 0.13	0.27±0.04	94.4±0.2
	weak_fluffy93				
	fluffy87	0.340± 0.009	1.43±0.40	0.86±0.10	86.8±0.3
	fluffy80	0.510± 0.020	—	—	80.3±0.9
Gypsum	—	1.10± 0.04	15.6±1.3[b]		52.3±1.7
Pumice	—	0.60± 0.01	5.1[c]		74.1±0.6
Sintered glass beads[d]	P35-R0	1.59	12.1± 3.4		36.5±0.3
	P35-R12.5	1.69	15.3±6.3		34.3±1.0
	P35-R25	1.80	17.5± 5.9		32.3±1.6
	P40-R0	1.49	1.91± 0.51		40.3±1.8
Gypsum[e]	—	1.10± 0.05	15.6± 1.3[b]		50±2
Foamed polystyrene[f]	L	0.011	0.07[g]		99.0[h]
	M	0.037	0.16[g]		96.4 ± 0.1[h]
	H	0.074	>0.2[g]		92.8 ± 0.3[h]
Aerogel[i]	—	0.060	—		97.7[j]

[a] Detailed information about the sintered glass-bead targets fluffy80, fluffy87, and fluffy94 is given in Section 2.2.1. We adopted the strength of either the stronger or the weaker part in our analyses, depending on which of either the top or bottom surfaces was impacted by the projectile.
[b] The compressive strength of gypsum with a porosity of 47±3% from Fujii and Nakamura (2009) is adopted here.
[c] The compressive strength of pumice from Nakamura *et al.* (2009) is adopted here.
[d] Data of Hiraoka (2008).
[e] Data of Yasui *et al.* (2012).
[f] Data of Ishibashi *et al.* (1990).
[g] Standard value (JIS A9511), corresponding to each bulk density.
[h] Porosity of the foamed polystyrene target is calculated assuming that the density of polystyrene is 1.056 g cm^{-3}(Chronological Scientific Tables, 2012).
[i] Data of Niimi *et al.* (2011).
[j] Porosity of the aerogel target is calculated assuming that the density of silicon dioxide is 2.648 g cm^{-3}(Greenwood and Earnshaw, 1984).

Table 3.2: Experimental conditions and results for cavity formation

Run number	Target type[a]	Impact velocity (km s^{-1})	Projectile material	Projectile size[b] (mm)	Projectile mass (mg)	Cavity Shape D_{ent}[c] (mm)	Cavity Shape D_{max}[d] (mm)	Cavity Shape L_{max}[e] (mm)	Cavity Shape BD[f] (mm)
1101_3	fluffy94	6.74	Ti	1.0	2.44	3.4	14.5	17.9	32.6
1105_A	fluffy94	7.17	Al	1.0	1.45	2.5	8.1	8.7	22.3
1105_B	fluffy94	4.28	Al	1.0	1.45	1.6	5.8	9.5	19.9
1111_P	fluffy87[g]	4.28	Ti	1.0	2.44	2.5	7.5	10.4	18.1
1111_Q	fluffy87[g]	6.76	Ti	1.0	2.44	3.9	8.1	8.7	16.5
1201_C	fluffy94	2.31	Basalt	$D3.2 \times H2.2$	45.2	4.1	14.2	30.3	79.4[h]
1204_G	fluffy94	2.26	Basalt	$D3.2 \times H2.2$	46.0	4.5	15.7	34.8	78.0[h]
1312_B	fluffy87	6.33	Nylon	3.2	19	12.4	20.5	12.4	27.9
1312_C	fluffy87	4.29	Nylon	3.2	19	6.9	13.6	11.6	26.1
1407_C	weak_fluffy93	2.74	Polystyrene	1.1	0.8	5.0 ± 0.2	7.6 ± 0.3	5.0 ± 0.2	13.6 ± 0.5
1407_D	weak_fluffy93	2.66	Basalt	$D3.2 \times H2.3$	47.9	4.5 ± 0.3	> 28.1[i]	> 32.7[i]	> 72.1[i]
1407_E	weak_fluffy93	4.04	Basalt	$D3.1 \times H2.2$	45.8	5.7 ± 0.6	> 24.9[i]	> 27.1[i]	> 87.2[i]
1407_F	weak_fluffy93	6.84	Al	1.0	1.5	9.4 ± 1.2	15.5 $^{(<19.2)}_{(>12.3)}$[j]	12.2 $^{(<14.6)}_{(>9.8)}$[j]	> 22.7[j]
1407_A	weak_fluffy93	6.77	Ti	1.0	2.4	14.8 ± 0.8	18.3 $^{(<19.4)}_{(>17.2)}$[j]	20.6 ± 8.1	27.2
1412_Z-o1	Pumice[k]	7.13	Nylon	3.2	19	29.0 ± 5.2	> 20.2 ± 1.3[l]	—[m]	19.3 ± 1.1
1412_Z-o5	Pumice[k]	3.58	Nylon	3.2	19	13.4 ± 1.4	> 10.4 ± 0.8[l]	—[m]	14.7 ± 0.6
1412_Z-o7	Pumice[k]	5.54	Nylon	3.2	19	23.1 ± 6.4	> 15.5 ± 2.2[l]	—[m]	19.0 ± 0.4
1412_Z-o8	Pumice[k]	5.51	Nylon	3.2	19	25.2 ± 2.5	> 19.5 ± 2.0[l]	—[m]	18.2 ± 2.0
1412_Y[n]	Pumice	7.19	Nylon	3.2	19	—[o]	> 18.9 ± 3.2[l]	—[m]	22.2 ± 0.6
1412_A	Gypsum	6.15	Al	3.2	45	38.6 ± 6.4	> 18.4 ± 1.3[p]	< 3.6 ± 0.6[p]	17.4 ± 0.3
1412_B	Gypsum	2.34	Nylon	3.2	19	11.8 ± 0.3	> 7.6 ± 0.5[p]	< 1.7 ± 1.1[p]	6.7 ± 0.2
1412_C	Gypsum	6.03	Al	3.2	45	33.1 ± 1.8	> 18.9 ± 0.7[p]	< 3.5 ± 0.8[p]	21.5 ± 3.3

[a] Diameters of fluffy94, fluffy87, weak_fluffy93, and gypsum are 62.5 ± 0.6 mm, 47.5 ± 0.3 mm, 145.1 ± 0.4 mm, and 122.7 ± 0.4, respectively. Heights of fluffy94, fluffy87, weak_fluffy93, and gypsum are 132.6 ± 5.4 mm, 102.4 ± 0.5 mm, 132.6 ± 2.0 mm, and 66.4 ± 2.7, respectively. Masses of fluffy94, fluffy87, weak_fluffy93, and gypsum are 57.4 ± 3.1 g, 59.7 ± 0.5 g, 361.1 ± 7.1 g, and 834 ± 45, respectively. The volume of irregular shape of pumice was measured by the spilled water from a bucket filled with water. The mass of pumice targets were 0.899–0.907 kg for 1412_Z and 0.793 kg for 1412_Y.
[b] Diameter for spherical projectiles; diameter (D) and height (H) for cylindrical projectiles.
[c] Entrance-hole diameter of the cavity.
[d] Maximum diameter of the cavity.
[e] Depth from the entrance hole to the maximum diameter of the cavity.
[f] Depth from the entrance hole to the bottom of the bulb.
[g] 1111_P and 1111_Q targets are differently shaped compared with the other fluffy87 targets; 48 mm in diameter, 200 mm in height, and 125.9 g in mass.
[h] These track types are transition between "carrot" and "bulb".
[i] The targets were partly destroyed due to the impacts. Thus the measurement of these dimensions are obtained from the X-ray images with time after 3000 μs and 2000 μs for 1407_D and 1407_E, respectively.
[j] The targets were destroyed near the impact cite and the cross-sections of the tracks could be observed. The upper and lower limits of the dimensions were obtained from visible images of the cross-sections.
[k] The target was cut into rough cubic from a block; Ten and several centimeters on a side.
[l] D_{max} for pumice here represents lower limit because those pit craters look like bulb shapes or box shapes (see text and Figure 3.1 (b) and (c)).
[m] L_{max} could not be determined because those pit craters look like bulb shapes or box shapes and the transmission images of these targets were not obtained.
[n] The target was irregular in shape except for the surfaces of the bottom and impact site, which are the planes and perpendicular to each other ; The sides of planes are ten and several centimeters.
[o] D_{ent} could not be determined because projectile impacted near the edge of the surface of the impact site and the spall zone reached the edge.
[p] D_{max} and L_{max} for gypsum here represents lower limits and upper limits, respectively (see text).

3.3 Results and discussions

3.3.1 Track profile and drag coefficient

Figure 3.2 shows some track profiles of sintered glass-bead targets extending from the entrance hole to the end of the track. Note that the X-ray images of the tracks are shown in Figure 2.2. The track shape of sintered glass-bead targets could be divided into two types: an elongated "carrot" shape and a short "bulb" shape. A distinction of these two types for the targets was the same criteria as that for aerogel targets (Burchell *et al.*, 2008), that is the ratio of the maximum diameter to the projectile's penetration depth was 0.11, although transitional shapes between the carrot and bulb shapes exists. The track shape depends on the ratio of the projectile's dynamic pressure to its strength (see Section 2.3.1). In this study, we focus on the bulb-shaped tracks, in particular on the cavity shape. Figure 3.3 presents an example of an X-ray transmission image and a sketch of a cavity cross section. The bulb-shaped cavity is characterized by an entrance hole with a diameter of several times the projectile diameter and a maximum cavity diameter located at some depth from the entrance hole. These characteristics of the bulb-shaped cavity have previously also been found in very porous targets such as aerogel and foamed polystyrene (Hörz *et al.*, 2006; Ishibashi *et al.*, 1990).

The craters formed on gypsum targets consisted of a small central pit like a bowl shape and surrounding spalls, which are similar to those reported based on previous impact experiments on sintered glass-bead targets with different porosities (Love *et al.*, 1993; Michikami *et al.*, 2007). Hiraoka (2008) describes experiments in which various projectiles (SUS, glass, alumina and nylon) were used as impactors with velocities of 2.5 to 3.5 km s^{-1} onto sintered glass-bead targets containing some rocky materials. The resulting craters in their experiments were also this type. Figure 3.1 (a) presents a sketch of a cross section of the crater with pit like a bowl shape. The crater shapes formed on pumice targets

are shown in Figure 3.1 (b) and (c). These craters also have pits, but they don't look like bowl shapes, but bulb shapes (b) or box shapes (c), i.e., the parts of pits' walls are parallel to the impact direction.

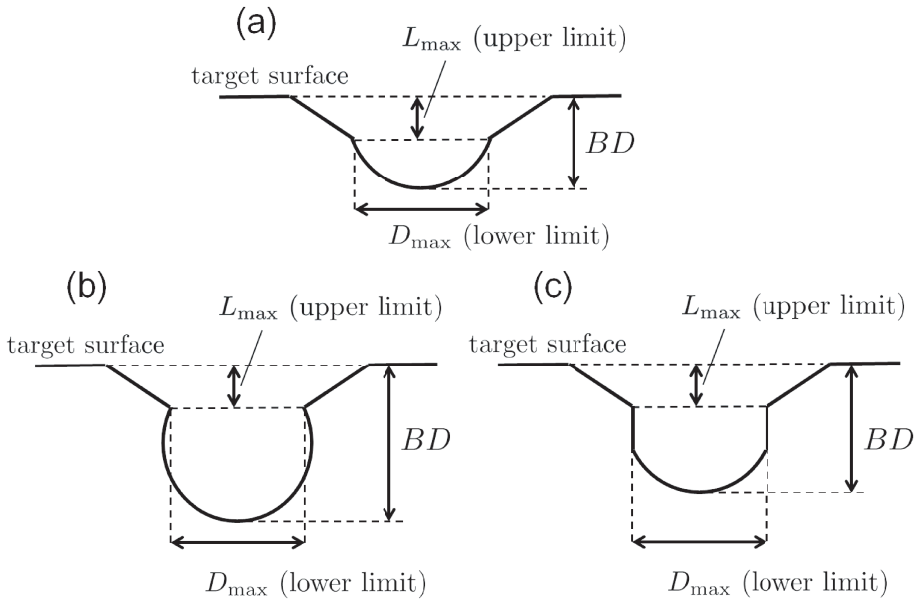

Figure 3.1: Schematic illustration of craters consisting of a central pit and surrounding spalls. The pit shape formed on gypsum targets and sintered glass-bead targets with porosities of 32–40% (Hiraoka, 2008) is illustrated in (a), whereas the pit shapes formed on pumice targets is illustrated in (b) for a bulb shape and (c) for a box shape. The depth from the target surface to the pit diameter and the pit diameter are regarded as upper limit to $L_{\max}$ and lower limit to $D_{\max}$, respectively.

Previous studies (Niimi *et al.*, 2011; Okamoto *et al.*, 2013) have reported that projectiles decelerate in the target through both inertial drag and drag that is proportional to the target strength. It has been shown that the former dominates during most of the penetration process, while the latter is effective only in the final phase of a projectile's penetration. The equation of motion for a given projectile is thus given by Eq. (2.5). Drag coefficient, C_{d} was calculated in Section 2.3.3 based on the initial cross-section area, S, and the initial projectile mass, m_{p}, although changes in S and m_{p} were observed over the course of the experiments unless the projectiles were intact. Here we refer to the drag coefficient as

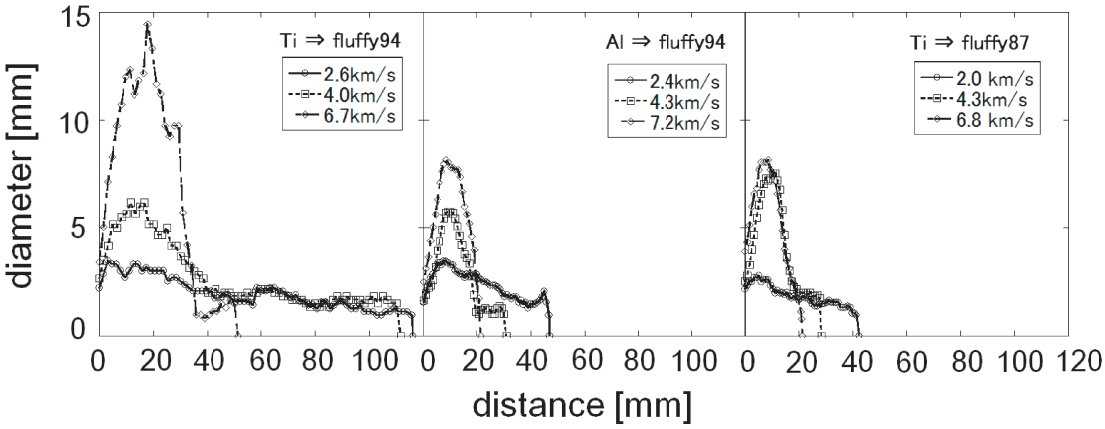

Figure 3.2: Track profiles of the targets from the entrance hole to the end. Left: Results of fluffy94 impacted by titanium (Ti) projectiles; carrot-shaped tracks are formed for impact velocities of 2.6 km s^{-1} and 4.0 km s^{-1}, while bulb-shaped track is formed for impact velocity of 6.7 km s^{-1}. Middle: Results of fluffy94 impacted by aluminum (Al) projectiles; a carrot-shaped track is formed for an impact velocity of 2.4 km s^{-1}, while bulb-shaped tracks are formed for impact velocities of 4.3 km s^{-1} and 7.2 km s^{-1}. Right: Results of fluffy87 impacted by Ti projectiles; a carrot-shaped track is formed at impact velocity of 2.0 km s^{-1}, while bulb-shaped tracks are formed for impact velocities of 4.3 km s^{-1} and 6.8 km s^{-1}. All X-ray transmission images are shown in Figure 2.2.

the effective drag coefficient, $C_{\mathrm{d\_eff}}$. The effective drag coefficient was shown to depend on the projectile's dynamic pressure normalized by its tensile strength. Figure 3.4 is a revised version of Figure 2.11; all previously obtained (Okamoto *et al.*, 2013) and new data pertaining to nylon projectiles have been re-plotted, along with the results of previous studies of aerogel and gypsum targets, as included in Table 3.1 (Niimi *et al.*, 2011; Yasui *et al.*, 2012). The effective drag coefficient increases with increasing normalized dynamic pressure. The following empirical relation is obtained for the sintered glass-bead targets:

$$C_{\mathrm{d\_eff}} = 10^{-0.039\pm0.041}\left(\frac{\rho_{\mathrm{t}}{v_0}^2}{Y_{\mathrm{pt}}}\right)^{0.22\pm0.03}. \tag{3.1}$$

Note that the effective drag coefficient is about unity when the projectile is not deformed or disrupted (Okamoto *et al.*, 2013). Eq. (3.1) will not be applicable in such cases. On the other hand, the effective drag coefficient may increase with increasing dynamic pressure because the projectile's cross-section area becomes larger during penetration. This

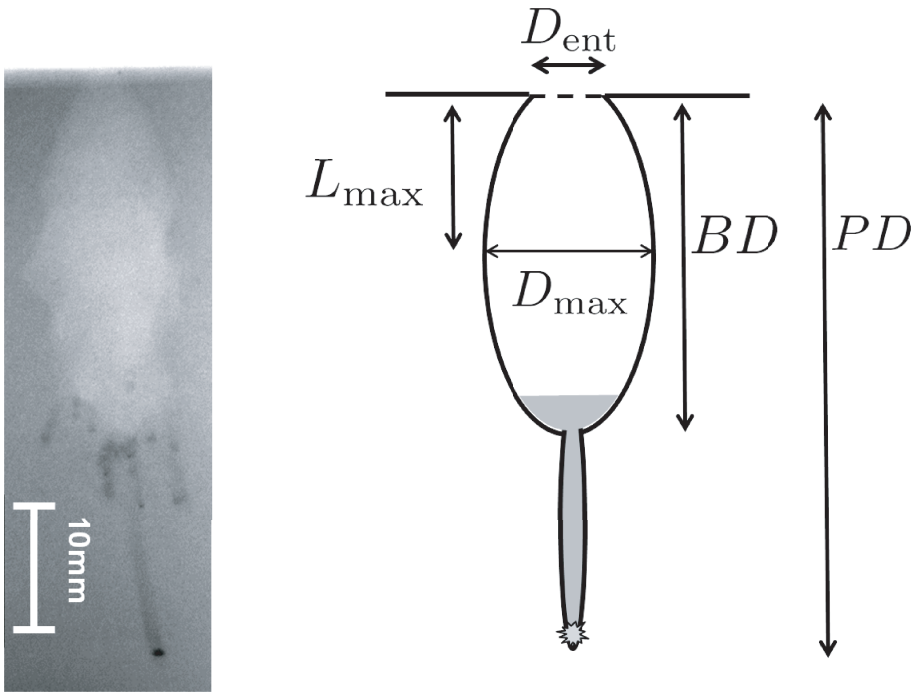

Figure 3.3: Left: X-ray transmission image after the impact of Ti with a diameter of 1 mm into fluffy94 at an impact velocity of 6.7 km s^{-1}. Right: Schematic illustration of the cavity dimensions. The gray part shows higher-density regions.

extended cross-section areas were measured on flash X-ray images. Figure 3.5 shows the area normalized by the projectile's initial cross-section area as a function of time from impact for run number 1111_T. Figure 3.5 indicates that the average normalized cross-section area seems to be approximately 2, which is comparable to the effective drag coefficient, $C_{\mathrm{d\_eff}} = 2.0 \pm 0.4$, derived from Eqs. (2.6) and (2.7), assuming that the considered cross-section area is the initial area. Thus, it is suggested that the value of the effective drag coefficients can be regarded as the average ratio of the projectiles' cross-section areas to its initial areas at the early stages of penetration in this case. Note that the run number 1111_T is the only shot in which the projectile was deformed or disrupted but not dispersed; i.e., the total mass remained equal to the initial mass. Other data on the effective drag coefficients may be affected by other mechanisms such as mass loss caused by dispersion.

3.3.2 Characteristic dimensions of the cavity

Depth from the entrance hole to the maximum cavity diameter, L_{max}

First, We describe the results of the depth from the entrance hole to the maximum cavity diameter, L_{max} (see Figure 3.3). Our results show that L_{max} decreases with increasing impact velocity and increases with increasing target porosity. The equation of motion for projectiles at the early stages of penetration is a function of α, which can be described as

$$\frac{\mathrm{d}v}{\mathrm{d}t} = -\alpha v^2, \tag{3.2}$$

where α is defined by Eq. (2.7). Eq. (3.2) is solved to yield $v(x)$,

$$v = v_0 \exp(-\alpha x), \tag{3.3}$$

where x is the distance from the point of impact. The kinetic energy of the projectile, E, is expressed as

$$E = E_0 \exp(-2\alpha x), \tag{3.4}$$

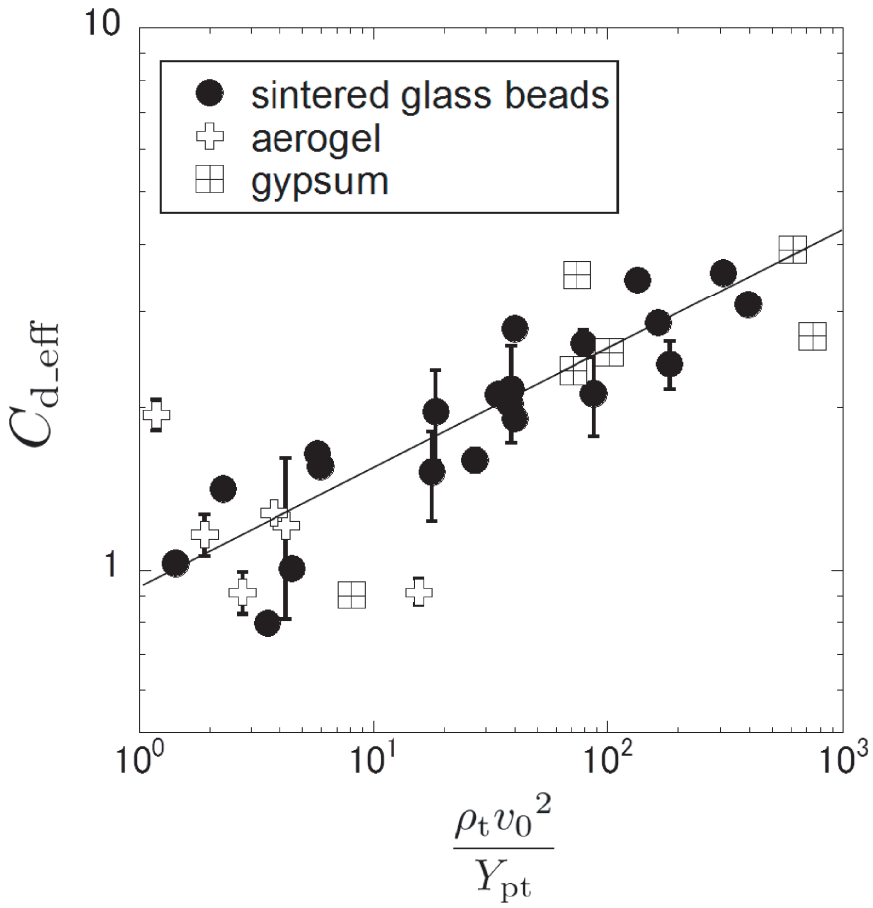

Figure 3.4: Effective drag coefficient versus normalized initial dynamic pressure, adapted from and updated compared with Figure 2.11. One of the effective drag coefficients (for basalt projectile impacting onto a fluffy94 target) has been re-examined and corrected with respect to the original plot. Results for aerogel targets (Niimi *et al.*, 2011) and gypsum targets (Yasui *et al.*, 2012) are also shown.

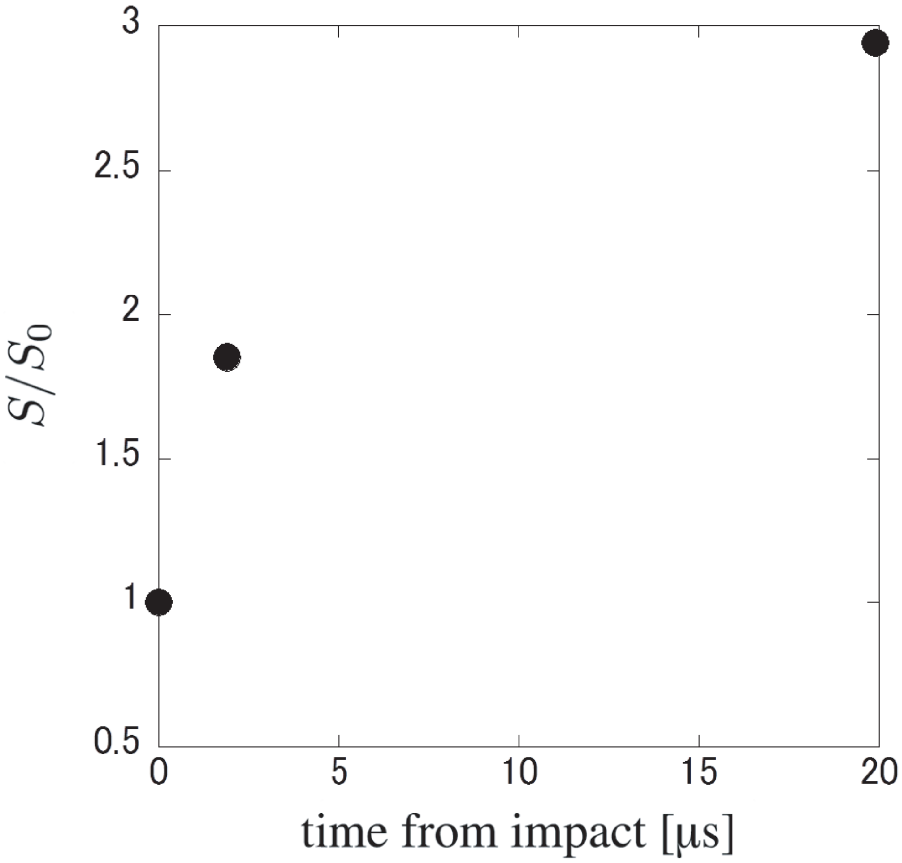

Figure 3.5: Projectile cross-section area, S, normalized by the initial cross-section area, S_0, as a function of time from the impact for run number 1111_T.

where E_0 is initial kinetic energy. The inverse of 2α has the dimension of length. We define a characteristic length, $L_0 = 1/(2\alpha)$, where the kinetic energy becomes 1/e of E_0. Using Eqs. (2.7) and (3.1), we calculate L_0. Figure 3.6 shows the relationship between $L_{\max}$ and L_0, both normalized by projectile diameter. Previous data of craters in sintered glass-bead targets with 32–40% porosity (Hiraoka, 2008) and bulb-shaped cavities in foamed polystyrene targets formed by nylon projectiles (Ishibashi *et al.*, 1990) are also shown (see Table 3.1). We assume that the pit diameter is the maximum diameter of the cavity, and we also assume that the depth from the target surface to the circumference of the pit is $L_{\max}$. The $L_{\max}$ data thus represent an upper limit, because the real depth to the maximum cavity diameter may be shallower than the depth to the pit diameter due to the existence of surface spalls (see Figure 3.1). The normalized $L_{\max}$ increases with the normalized L_0. This may suggest that the depth to the maximum cavity diameter depends on the degree of projectile deformation or disruption caused by the effective drag coefficient, and it also depends on the projectile-target density ratio. Fitting the data pertaining to fluffy87, waek_fluffy93, and fluffy94 and foamed polystyrene targets, i.e., targets with porosities of >87%, yields

$$\frac{L_{\max}}{d_{\mathrm{p}}} = 10^{0.62\pm0.05}\left(\frac{L_0}{d_{\mathrm{p}}}\right)^{0.47\pm0.06}. \tag{3.5}$$

The empirical equation for the effective drag coefficient, Eq. (3.1), can be used to derive the following empirical equation from Eq. (3.5):

$$\frac{L_{\max}}{d_{\mathrm{p}}} = (3.6 \pm 0.5)\left(\frac{Y_{\mathrm{pt}}}{\rho_{\mathrm{t}} {v_0}^2}\right)^{0.10\pm0.02}\left(\frac{\rho_{\mathrm{t}}}{\rho_{\mathrm{p}}}\right)^{-0.47\pm0.06}. \tag{3.6}$$

The power-index of the normalized strength, $Y_{\mathrm{pt}}/(\rho_{\mathrm{t}} {v_0}^2)$, is smaller than that of the density ratio, thus $L_{\max}/d_{\mathrm{p}}$ is almost determined by the density ratio.

Maximum cavity diameter, $D_{\max}$, and the bulb depth, BD

Second, we describe the results of the maximum cavity diameter, $D_{\max}$, and the bulb depth, BD. Note that bulb depth is defined as length from the entrance hole to the bottom

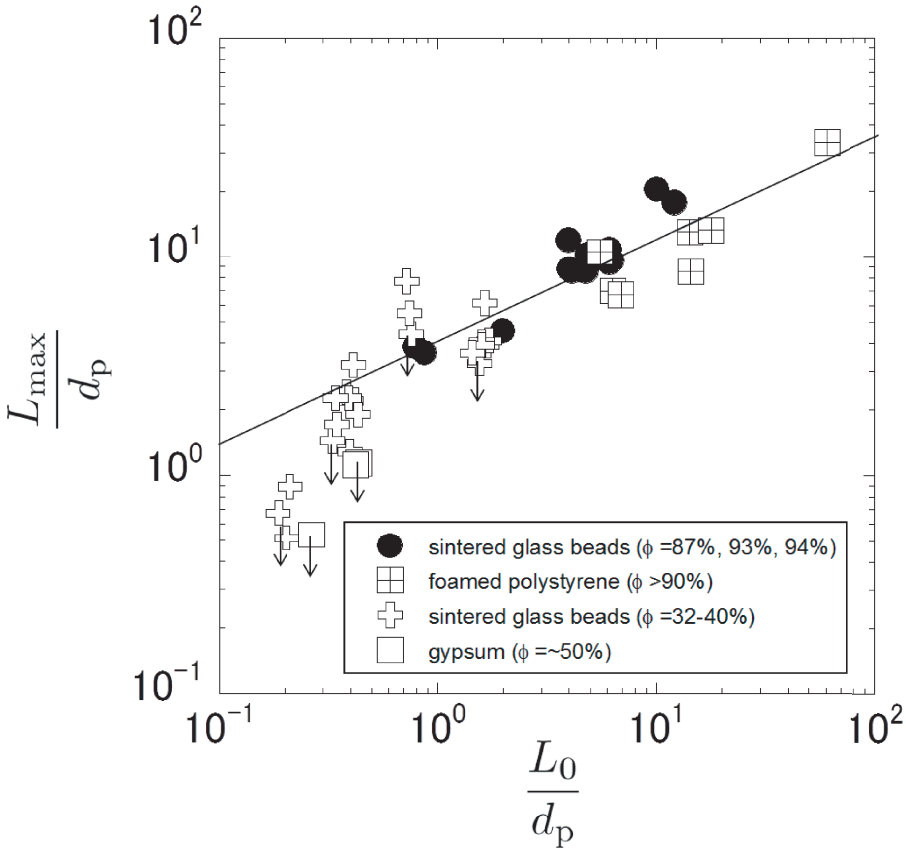

Figure 3.6: Normalized $L_{\max}$ versus normalized characteristic length. Results for sintered glass-bead targets (ϕ =32%–40%; Hiraoka, 2008) and foamed polystyrene targets (Ishibashi *et al.*, 1990) are also shown. The data for sintered glass-bead targets with porosity of 32–40% and gypsum targets (our study) yield upper limits (see text). The best-fitting line has been obtained using data for sintered glass beads (ϕ =94, 93, 87%) and foamed polystyrene targets.

of the bulb (see Figure 3.3).

Scaling relations for craters were derived by assuming that projectiles behave as point sources (Holsapple and Schmidt, 1987). The scaling relation for the strength regime applies when the target strength, Y, is much greater than $\rho_t gh$, where g is the gravitational acceleration and h is a characteristic crater length (e.g. diameter or depth). This is the case for the present experiment. In this regime, as seen in Section 1.3, the crater diameter is described by

$$D\left(\frac{\rho_t}{m_p}\right)^{\frac{1}{3}} = K_{Ds}(\phi)\left(\frac{Y_t}{\rho_p {v_0}^2}\right)^{\frac{-\mu}{2}}\left(\frac{\rho_t}{\rho_p}\right)^{1-3\nu+\frac{\mu}{2}}, \tag{3.7}$$

(Housen and Holsapple, 2003). Eq. (3.7) is modified simply as follows if the projectile is a sphere:

$$\frac{D}{d_p} = H_{Ds}(\phi)\left(\frac{Y}{\rho_t {v_0}^2}\right)^{-\mu/2}\left(\frac{\rho_t}{\rho_p}\right)^{-\nu}, \tag{3.8}$$

where H_{Ds} is a scaling constant as a function of porosity. We use the non-dimensional parameter sets in Eq. (3.8) for our analysis of the maximum cavity diameter. The compressive strength of the target, Y_c, is used as a proxy of the target strength, Y. It has been reported that the exponent of ν is equal to approximately 0.4 regardless of material type (Housen and Holsapple, 2011). We adopt this value here. Figure 3.7 shows the maximum diameter normalized by projectile diameter, multiplied by the ratio of the bulk densities to the power 0.4 as a function of the target's compressive strength, normalized by the initial dynamic pressure. Data from previous studies (see Table 3.1) are also shown. The pit-diameter values are used as the maximum diameters except for sintered glass-bead targets with porosities of 94, 93, and 87% and foamed polystyrene targets. Therefore they represent lower limits for the same reasons as those pertaining to the maximum-diameter depths for the sintered glass-bead targets of Hiraoka (2008). The normalized maximum diameters show the approximate power-law dependence of the diameters to the normalized strengths. It is also shown that the values of the scaled diameters increase with increasing target porosity. The best-fitting results based on application of Eq. (3.8) to the data

pertaining to fluffy87, weak_fluffy93, and fluffy94, and foamed polystyrene targets, i.e., targets with porosities of >87% yield

$$\frac{D_{\max}}{d_{\mathrm{p}}} = 0.20 \pm 0.07 \left(\frac{Y_{\mathrm{c}}}{\rho_{\mathrm{t}} {v_0}^2}\right)^{-0.26\pm0.04} \left(\frac{\rho_{\mathrm{t}}}{\rho_{\mathrm{p}}}\right)^{-0.4}. \tag{3.9}$$

We also fitted the data pertaining to gypsum targets and pumice targets. The summary of the results for scaling constants in Eq. (3.8) is shown in Figure 3.8. The values of μ is approximately within the range of 1/3 to 2/3 allowed by the scaling theory based on the point-source assumption. The values of H_{Ds} decrease with increasing porosity. Empirical equations of scaling constants of H_{Ds} and μ are obtained as follows:

$$H_{\mathrm{Ds}}(f) = (0.15 \pm 0.06)(1 - f)^{-1.4\pm0.6}, \tag{3.10}$$

$$\mu(f) = (0.53 \pm 0.09) + (0.15 \pm 0.18) f. \tag{3.11}$$

We will discuss the crater diameter of the icy bodies using these empirical equations in Section 3.3.3.

The crater depth is described by

$$d\left(\frac{\rho_{\mathrm{t}}}{m_{\mathrm{p}}}\right)^{\frac{1}{3}} = K_{\mathrm{ds}}(\phi)\left(\frac{Y}{\rho_{\mathrm{p}} {v_0}^2}\right)^{\frac{-\mu}{2}} \left(\frac{\rho_{\mathrm{t}}}{\rho_{\mathrm{p}}}\right)^{1-3\nu+\frac{\mu}{2}}, \tag{3.12}$$

(Housen and Holsapple, 2003). Eq. (3.12) is modified simply as follows if the projectile is a sphere as in the case of crater diameter:

$$\frac{d}{d_{\mathrm{p}}} = H_{\mathrm{ds}}(\phi)\left(\frac{Y}{\rho_{\mathrm{t}} {v_0}^2}\right)^{-\mu/2} \left(\frac{\rho_{\mathrm{t}}}{\rho_{\mathrm{p}}}\right)^{-\nu}, \tag{3.13}$$

where H_{ds} is a scaling constant. The compressive strength of the target, Y_{c}, is used as a proxy of the target strength, Y. We assigned 0.4 to the value of ν. Figure 3.9 shows the bulb depth normalized by projectile diameter, multiplied by the ratio of the bulk densities to the power 0.4 as a function of the target's compressive strength, normalized by the initial dynamic pressure. The depth from the entrance hole to the bottom of the cavity is used

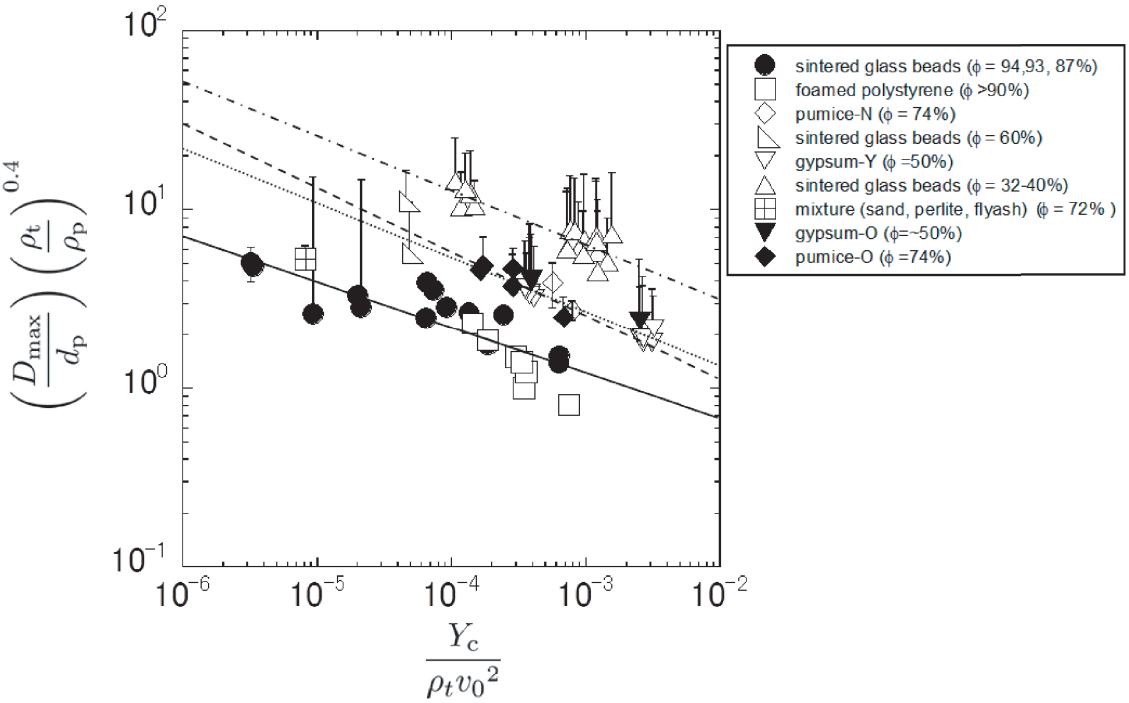

Figure 3.7: Normalized $D_{\max}$, multiplied by the ratio of the bulk densities to the power 0.4 versus the non-dimensional parameter, $Y_c/\rho_t v_0{}^2$. Results for foamed polystyrene targets (Ishibashi *et al.*, 1990), sintered glass-bead targets (ϕ= 60%, Michikami *et al.*, 2007, ϕ= 32–40%, Hiraoka, 2008), pumice-N (Nakamura *et al.*, 2009), gypsum-Y targets (Yasui *et al.*, 2012), and sand-perlite-flyash mixture targets (Housen and Holsapple, 2003) are also shown. Data for the sintered glass-bead targets (ϕ =32–40%; Hiraoka, 2008) and gypsum targets yield lower limits (see text). These data has upper limits which indicate the entrance-hole diameters. Solid line is the best-fitting line based on the data for sintered glass beads (ϕ = 94%, 93%, 87%) and foamed polystyrene targets. Dashed, dotted, and dashed-dotted lines are the best-fitting lines for pumice, gypsum, sintered glass-bead targets (ϕ =32–40%; Hiraoka, 2008), respectively.

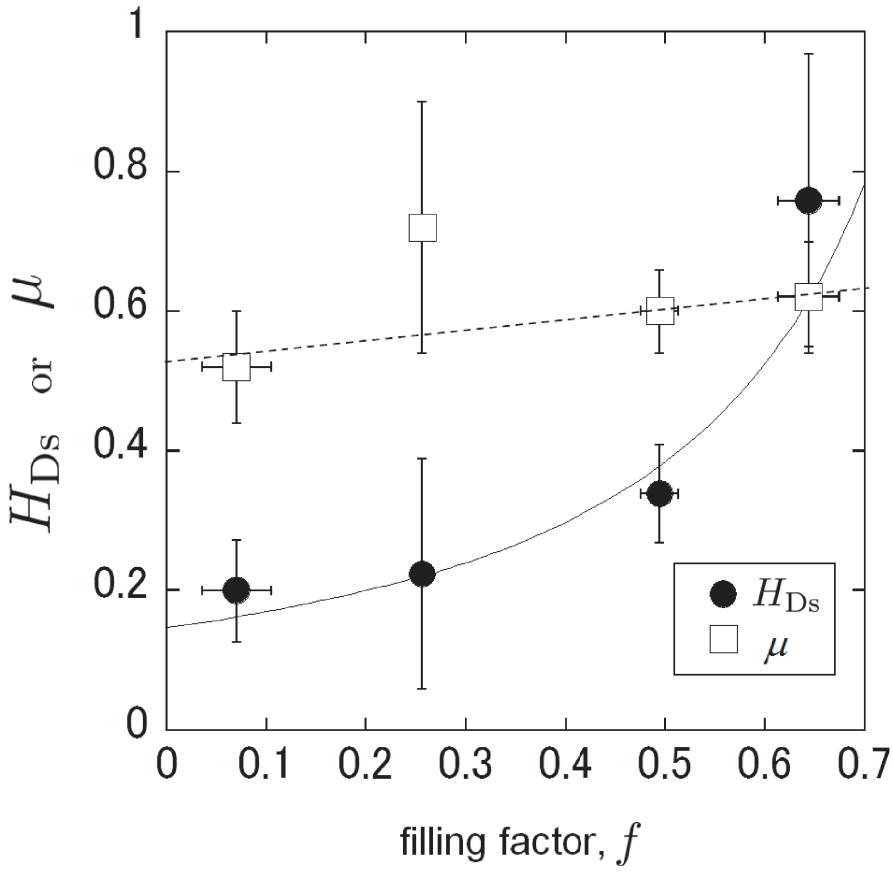

Figure 3.8: Scaling constants as a function of filling factor. Scaling constants H_{Ds} and μ are defined as Eq. (3.8).

as the bulb depth for sintered glass-bead targets with porosities lower than 60%, pumice targets and gypsum targets. We fitted the data by Eq. (3.13). The summary of the results for scaling constants in Eq. (3.13) is shown in Figure 3.10. Empirical equations of scaling constants of H_{ds} and μ are obtained as follows:

$$H_{\mathrm{ds}}(f) = (0.48 \pm 0.20) f^{-0.95\pm0.21}, \tag{3.14}$$

$$\mu(f) = (-0.01 \pm 0.07) + (0.76 \pm 0.20) f. \tag{3.15}$$

The values of H_{ds} increases with increasing porosity. The values of μ is out of the range of 1/3 to 2/3. This must be because the point-source assumption can not be applicable for the bulb depth due to penetration of the projectiles. Thus whether this bulb depth scaling is allowed to be used directly for the surface of small bodies is not convincing.

On the other hand, Love *et al.* (1993) and Michikami *et al.* (2007) reported a relationship between crater depth and the ratio of projectile density to the target density. In Figure 3.11, we compared the bulb depth of our results with those of various previous studies. Figure 3.11 shows the approximate power-law relation between the normalized bulb depth and the projectile to target density ratio, though the data are scattered within a factor of ~2. The best-fitting line for all data yields:

$$\frac{BD}{d_{\mathrm{p}}} = 10^{0.46\pm0.03} \left(\frac{\rho_{\mathrm{p}}}{\rho_{\mathrm{t}}}\right)^{0.72\pm0.03}. \tag{3.16}$$

Note that Eq. (3.16) may be applicable validly only within the range of the experimental conditions under which the experiments were conducted, i.e., the impact velocity ranging from 1.22 to 7.20 km s^{-1}, and the porosity being larger than 32%.

In the following discussion, we will use both scalings for bulb depths obtained from the crater scaling law and the relation between the depth and the projectile-to-target density ratio.

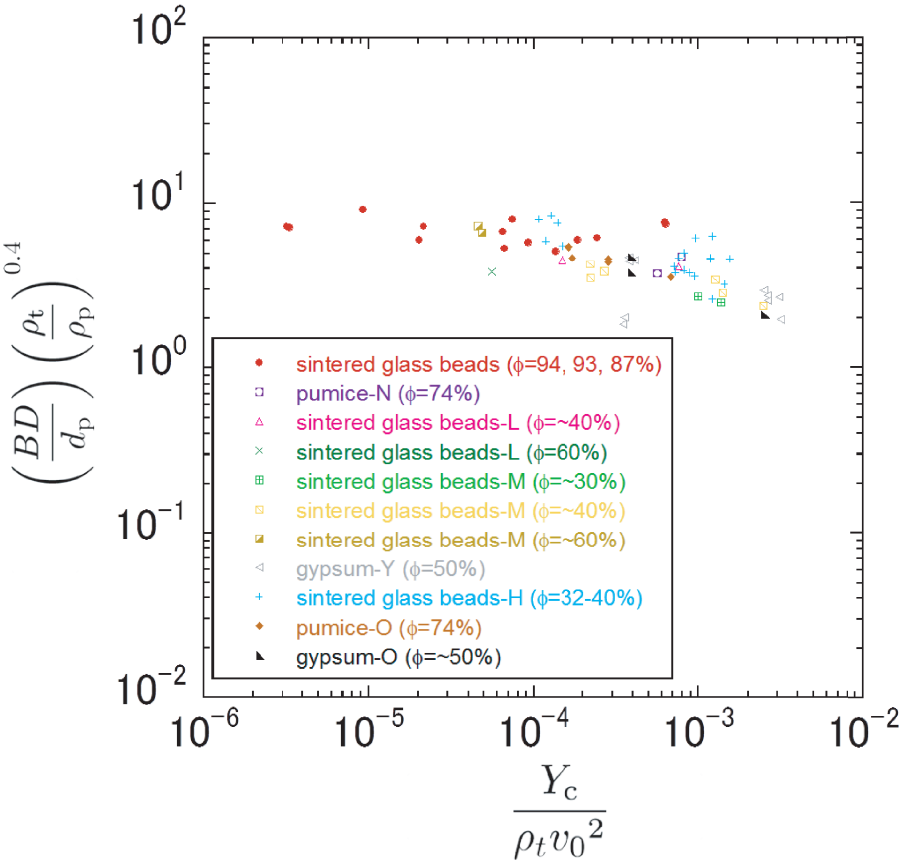

Figure 3.9: Normalized *BD*, multiplied by the ratio of the bulk densities to the power 0.4 versus the non-dimensional parameter, $Y_c/\rho_t {v_0}^2$. Results for sintered glass beads-L targets (Love *et al.*, 1993), sintered glass beads-M targets (Michikami *et al.*, 2007), sintered glass beads-H targets (Hiraoka, 2008), pumice-N (Nakamura *et al.*, 2009), and gypsum-Y targets (Yasui *et al.*, 2012) are also shown.

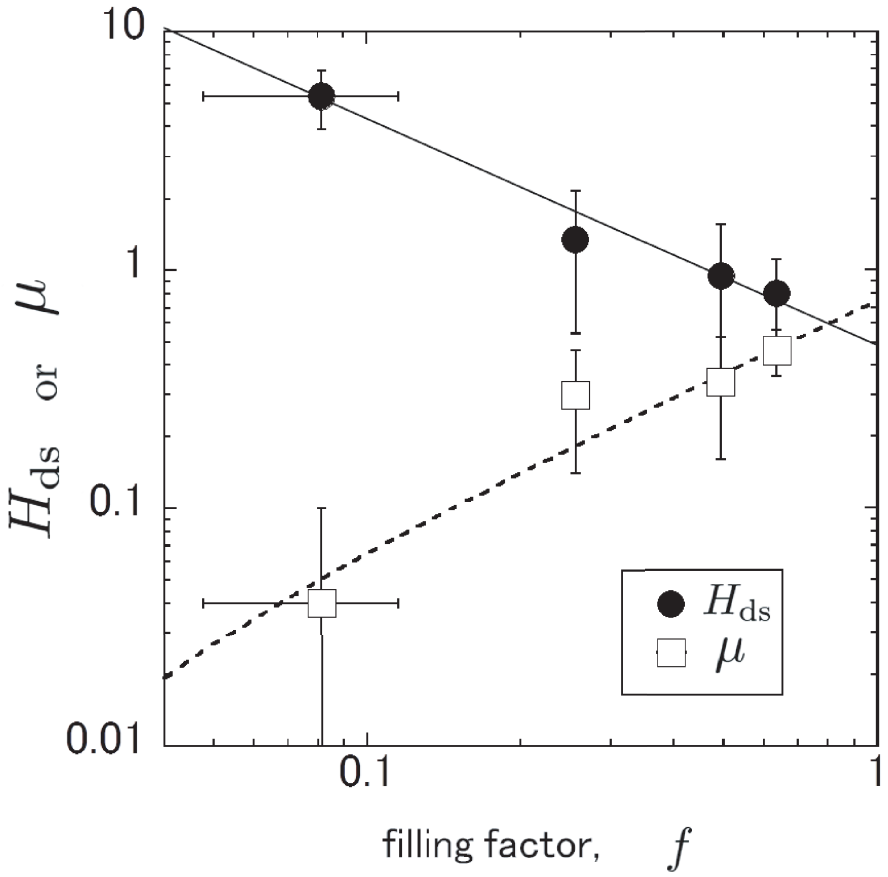

Figure 3.10: Scaling constants as a function of filling factor. Scaling constants $H_{\rm ds}$ and μ are defined as Eq. (3.13). The results are obtained from data of sintered glass-bead targets (Love *et al.*, 1993; Michikami *et al.*, 2007; Hiraoka, 2008) for filling factor of 0.64, and from data of gypsum targets (Yasui *et al.*, 2012; this study) for filling factor of 0.49, and from data of pumice targets (Nakamura *et al.*, 2009; this study) for filling factor of 0.26, and from data of sintered glass-bead targets (This study) for filling factor of 0.08.

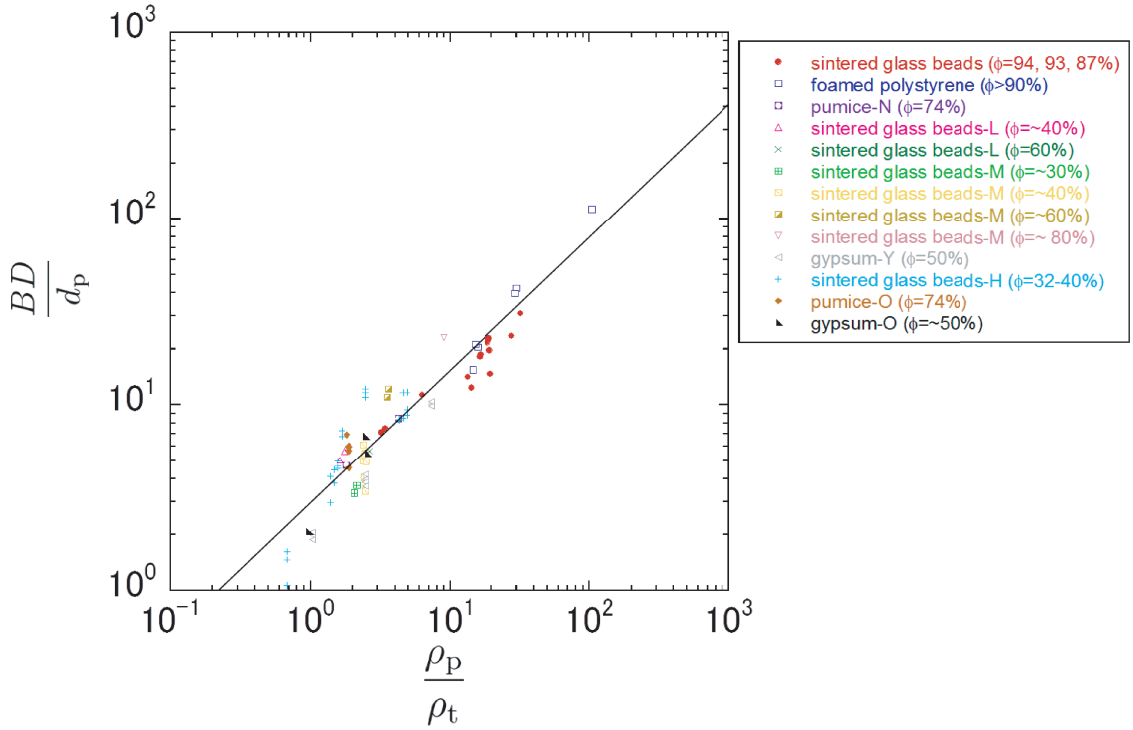

Figure 3.11: *BD* normalized by the projectile diameters versus the ratio of the projectile density to the target density. Results for foamed polystyrene targets (Ishibashi *et al.*, 1990), sintered glass beads-L targets (Love *et al.*, 1993), sintered glass beads-M targets (Michikami *et al.*, 2007), sintered glass beads-H targets (Hiraoka, 2008), pumice-N (Nakamura *et al.*, 2009), and gypsum-Y targets (Yasui *et al.*, 2012) are also shown. The solid line shows the best-fitting line for all data.

3.3.3 Implication for craters on icy bodies

We apply the empirical relations obtained here to the surfaces of the porous icy bodies. We assumed that the cratering process is dominated by strength rather than surface gravity in the following discussions.

It was reported that an impactor of 370 kg in mass and about 1m in diameter, which was made of copper (49%) and aluminum (24%) was hit on the surface of comet Tempel 1 at an impact velocity of 10.2 km s^{-1} and an impact angle, θ of about 60° from the regional surface normal vector (A'Hearn *et al.*, 2005). However, the impact angle is highly uncertain. Richardson *et al.* (2007) reported that the axis orientation of ejecta plume changed with time. They interpreted the apparent change as meaning that the impact apparently occurred on a locally westward facing slope roughly 1/3–1/2 the size of the final crater (on the order of a few tens of meters) produced. Thus impact angle may be closer to 0° rather than 60°. Here we use values of d_p=1.0 m, ρ_p=700 kg m^{-3}(the mean impactor density), ρ_t=400 kg m^{-3}(Richardson *et al.*, 2007), v_0=10.2 km s^{-1} (A'Hearn *et al.*, 2005), and ϕ=76% (Consolmagno *et al.*, 2008). We used two impact angles, θ=0° and 60°, assuming only the normal component of impact velocities contributes to the cratering process. Figure 3.12 shows the maximum diameter normalized by projectile diameter obtained from Eqs. (3.8), (3.10) and (3.11), as a function of the compressive strength of the comet surface. The final crater had not been directly measured in Deep Impact mission because of a large amount of fine dust in the ejecta obscuring the view (A'Hearn *et al.*, 2005), however the images of the impact site were taken by the Stardust-NExT spacecraft. The impact crater was tentatively identified, barely resolvable, and the investigation of the images suggests that the diameter is 49 ± 12 m (Richardson and Melosh, 2013). To create a crater of this size, the compressive surface strength should be 479^{+813}_{-258} Pa for the case of impact angle of 0° and 120^{+203}_{-65} Pa for the case of impact angle of 60°, respectively. These values are one order of magnitude less than the values of the comet strength which were estimated as not

more than 10^3–10^4 Pa by Richardson *et al.* (2007), however in agreement with the other estimate of 500 Pa in bulk tensile strength for comet Wirtanen (Blum *et al.*, 2006).

We discuss the particle size of the surface of Tempel 1 and necessity of metamorphic event of the surface in a simple cometesimal-formation model based on sticking of sub-micrometer-sized ice particles (e.g. Kataoka *et al.*, 2013). Assuming that grains are monodisperse, compressive strength of granular media, σ_c is approximately expressed as follows :

$$\sigma_c = \frac{100 - \phi}{\phi} \cdot \frac{F_c}{{d_g}^2}, \tag{3.17}$$

(Rumpf, 1970; Tsubaki, 1984) where F_c and d_g are the compressive force worked in contact between two grains, and grain diameter, respectively. When we assume only interparticle force, the force, F_c is the force needed to separate two particles in contact, and it is expressed as,

$$F_t = 3\pi\gamma R, \tag{3.18}$$

where γ is surface energy, and $R = (1/r_1 + 1/r_2)^{-1}$ is the reduced radius of the grains of radii r_1 and r_2. Here R is $d_g/4$. The surface energy for ice is 100 mJ m^{-2} (Israelachvili, 1992), and we adopted this value. Figure 3.13 shows the relation between the compressive strength of the surface and the grain size for $\phi = 70$ and 80%. The compressive strength for $\phi = 70\%$ is 1.7 times larger than that for $\phi = 80\%$ at the same grain size. The range of the compressive strength of Tempel 1 obtained from this study is also shown in Figure 3.13. The corresponding grain diameter is from 58 μm to 1.4 mm for the porosity of Tempel 1 ($\phi = 76\%$). As the relation shown in Fig. 3.13 is derived only from interparticle forces, the strength of comet surfaces must become stronger because sintering may occur. Thus the grain size of the impact site of Tempel 1 is larger than 58 μm. It suggests that a simple cometesimal-formation model based on sticking of sub-micrometer-sized ice particles (e.g. Kataoka *et al.*, 2013), i.e., the formation of icy cometesimals only by direct sticking can

not explain the larger dust size. Metamorphic event of the surface is necessary for the explanation.

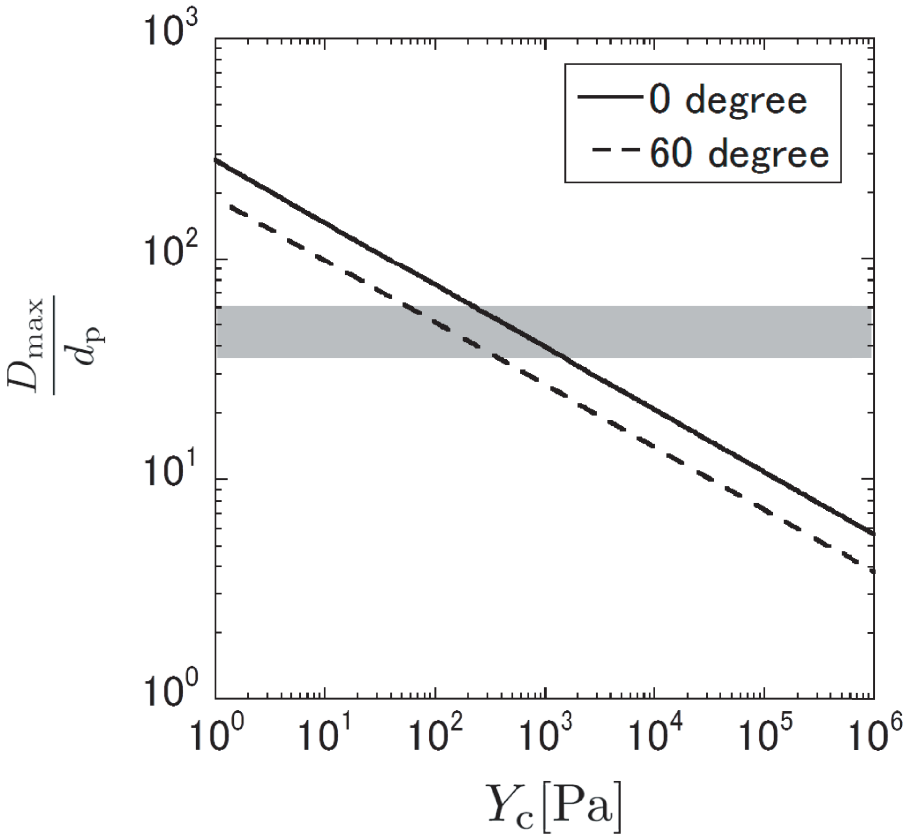

Figure 3.12: Normalized maximum cavity diameter as a function of compressive strength of the comet surface obtained from Eqs. (3.8), (3.10) and (3.11). Solid line and dashed line show the results of impact angle of 0°, and 60°, respectively. Light gray area corresponds to the normalized diameter determined from observation by Stardust-NExT (Richardson and Melosh, 2013).

Hyperion is a Saturn's irregular satellite and has a sponge-like appearance. It has characteristics of a primitive icy body that condensed in the solar nebula. It is acceptable to think of this satellite as a captured body that formed outside the Saturn system (Brad *et al.*, 2012). Mean crater depth-to-diameter ratio of Hyperion was estimated to 0.295 ± 0.451 for 3 examples by White and Schenk (2011). Howard *et al.* (2012) reported crater diameter and depth for 8 examples on Hyperion and the mean value is 0.25 ± 0.09. These depth-

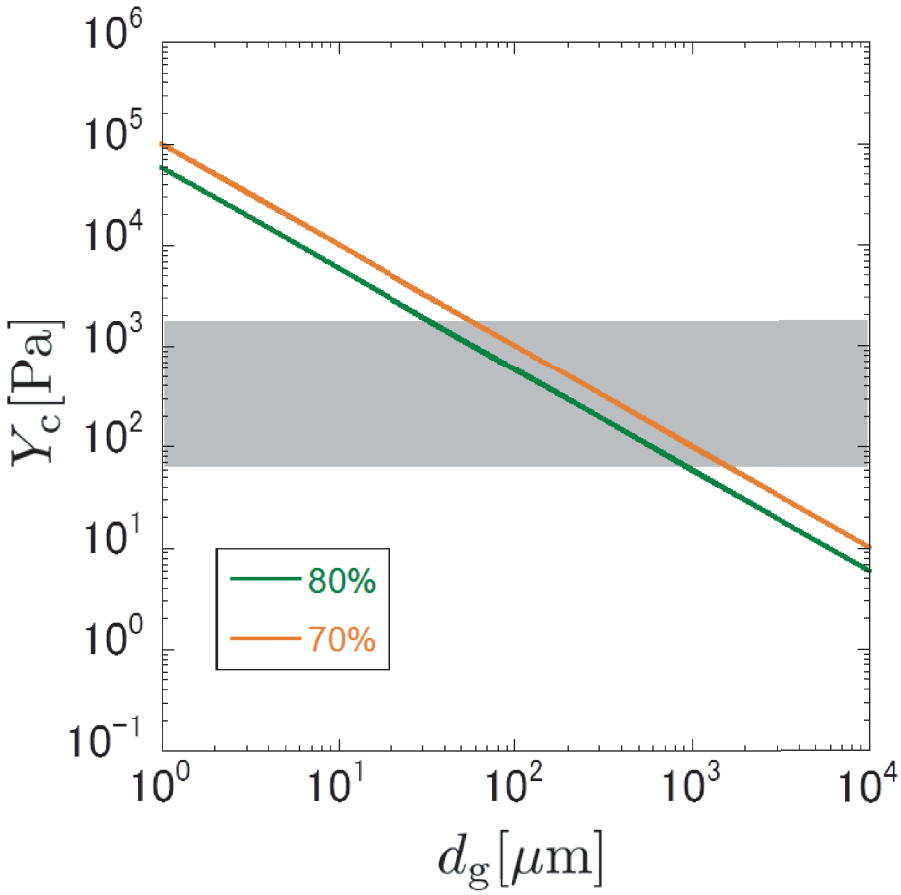

Figure 3.13: The compressive strength of the comet surface as a function of grain size obtained from Eqs. (3.17) and (3.18). The orange line shows the result for ϕ = 70%, and the green line shows the result for ϕ = 80%. The Light gray area corresponds to the range of the compressive strength of the surface obtained from this study.

to-diameter ratio is slightly larger than that observed on the Moon, ~0.2. The surface exhibits a lot of depressions ranging in size from the resolution limits of Cassini imagery (180 m/pixel) to upwards of 50 km diameter (Brad *et al.*, 2012). The unusual appearances of Hyperion are dark surfaces in the floors of degraded craters (Thomas *et al.*, 2007b). The compositional analysis of the dark deposition of low albedo material was conducted by Brad *et al.* (2012), and the results show that the low albedo material is nanophase iron and iron oxide, while some carbonaceous materials (aromatic and aliphatic hydrocarbons) are present.

Here we tentatively discuss the case that an impactor is a C-type asteroid (planetesimal) that would be abundant in the formation region of Saturn in the Grand Tack model (Walsh *et al.*, 2011) and that contains aromatic and aliphatic hydrocarbons (Sephton, 2002). The bulk density and tensile strength of a C-type asteroid are assumed in two cases; one is the case of high density and strength and the other is the case of low density and strength. The parameter values for the former are based on a carbonaceous chondrite. We assumed that the bulk density as 2250 kg m^{-3}(Consolmagno *et al.*, 2008), which is the average density of CM chondrites. The tensile strength, Y_{pt} is assumed to be 3.2 MPa (Tsuchiyama *et al.*, private communication, 2012) which was obtained from the mean tensile strength of small fragments of a CM carbonaceous chondrite (Murchison) with mean diameter of 60–300 μm. The value falls the same order of magnitude with the upper limit value of the bulk strengths upon entry of meteoroids into Earth's atmosphere (Popova *et al.*, 2011). In the latter, we assumed the tensile strength to be 500 Pa, which is the estimated value of the bulk tensile strength of comet Wirtanen with diameter of about 1.2 km (Blum *et al.*, 2006). This value is also of the same order of magnitude of the surface compressive strength of Tempel 1 we obtained in this study. In this case, the mean bulk density of a C-type asteroid, ρ_p=1400 kg $m^{-3}$is used (Consolmagno *et al.*, 2008). Table 3.3 shows the parameters of impactors in both cases. The mean bulk density of Hyperion was given as ρ_t=544 kg

m^{-3}(Thomas *et al.*, 2007b). We adopted the value of the porosity of Hyperion, ϕ= 65%, assuming that the grain density is 1600 kg m^{-3}which is used for estimation of comets' porosities (Consolmagno *et al.*, 2008), whereas Thomas *et al.* (2007b) reported that the porosity is larger than 40%, which was derived assuming that Hyperion is primarily water ice.

Table 3.3: The parameters of impactor used in the estimation

	Density (kg m^{-3})	Strength (Pa)	impact velocity (km s^{-1})
case 1	2250	3.2×10^6	1 5 10.5
case 2	1400	500	1 5 10.5

Figure 3.14 is the results of the ratio of bulb depth to maximum diameter and the ratio of penetration depth to maximum diameter as a function of compressive strength of surface of Hyperion. These results are obtained from Eqs. (2.1) and (2.9) for penetration depth, Eqs. (3.8), (3.10) and (3.11) for maximum diameter, and Eq. (3.16) for bulb depth. All the results of the ratios increase with increasing of the surface strength. For the ratio of bulb depth to the maximum diameter, BD/D_{max}, this is because the maximum diameter decreases with increasing the strength, whereas the bulb depth is determined only by projectile-to-target density ratio in our scaling relation. The ratio of penetration depth to the maximum diameter, PD/D_{max} decreases with increasing impact velocities. This is because the largest fragment of the impactor is disrupted at high initial dynamic pressure and resulted in the fragment of smaller size which can not penetrate deep inside the bodies (see Section 2.3.4). The results of the ratio of penetration depth to the maximum diameter for the case of lower density and weaker strength of impactor is smaller than that for the

case of higher density and stronger strength. This is also because the penetration depth becomes shallow due to disruption of projectile.

For impact velocity of 1 km s^{-1}, the line of BD/D_{max} and PD/D_{max} for ρ_p = 2250 kg m^{-3}, Y_{pt} = 3.2 MPa is crossover at the depth to the diameter ratio of ~0.3. It indicates that the part of impactor survives at the bottom of the crater. In other words, the craters are supposed to be created by carbonaceous impactors at impact velocity around 1 km s^{-1} and result in high values of depth-to-diameter ratio of ~0.3, and in survivals of impactors as dark material on the floors of craters. The crossover point corresponds to the compressive strength of 10^2–10^3 Pa, which is similar to the value obtained in the comet Tempel 1 in this study. On the other hand, the crater size that can be applicable to the scaling relations in strength regime on Hyperion would be smaller than about 10 km, if we assume that the crater size D is similar to $Y_t/(\rho_t g)$, and ρ_t is 544 kg m^{-3}(Thomas *et al.*, 2007b), g is 0.017 m s^{-2} (Thomas, 2010), and Y_t is 10^5 Pa. The relative impact velocity of impactor onto Hyperion is determined to be 9.4 km s^{-1} (Zahnle *et al.*, 2003), which is similar to the case of impact velocity of 10.5 km s^{-1} in Figure 3.14. The results show that the depth-to-diameter ratio is 0.3 at the surface compressive strength of ~ 10^5. Thus high values of depth-to-diameter of ~0.3 could be obtained by impact only. In contrast, the ratio of the penetration depth to the maximum diameter ratio is much smaller than the ratio of bulb depth to maximum diameter for the bodies having strength of 10^5 Pa. The dark material in the floors of the craters may be the fragment remnants of the impactor.

Figure 3.15 is for the case of Tempel 1. The average relative impact velocity for comet Tempel 1 is estimated to be 10.5 km s^{-1} (Vincent *et al.*, 2014) and this velocity is assumed here. The impact conditions of impactor here are the same as Table 3.3, and the bulk density, ρ_t and the porosity, ϕ of Tempel 1 are assumed to be 400 kg m^{-3}(Richardson *et al.*, 2007) and 76% (Consolmagno *et al.*, 2008), respectively. Eq. (3.16), which was obtained from the relation between the bulb depth and the projectile-to-target density ratio, is used

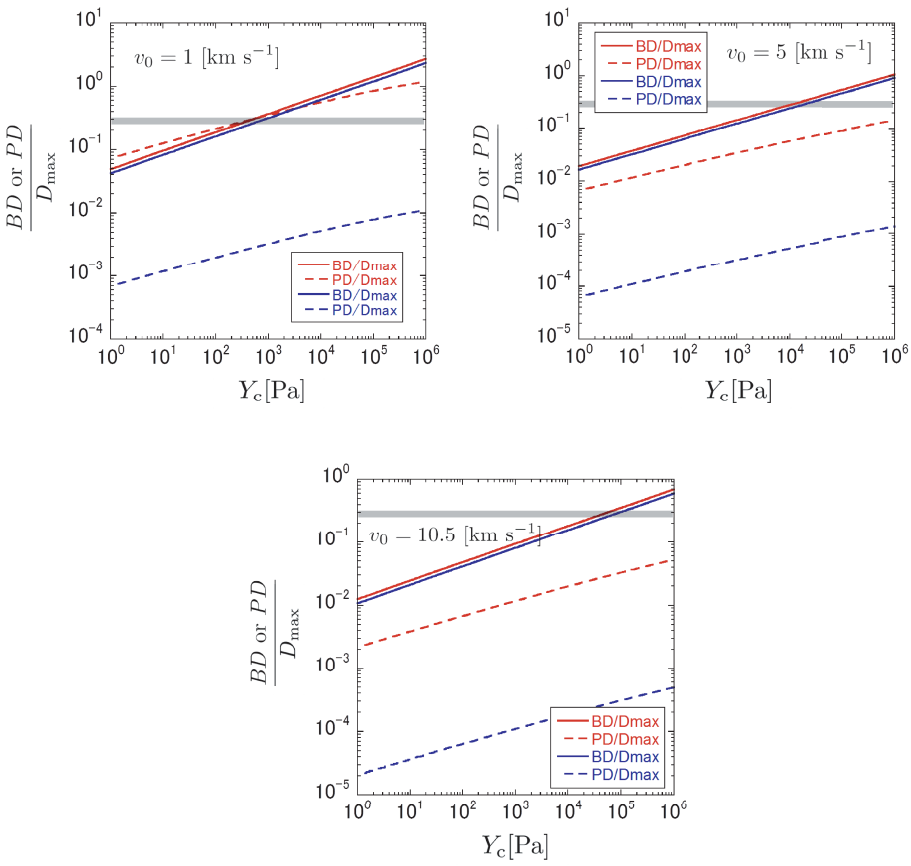

Figure 3.14: The ratio of bulb depth to maximum diameter and the ratio of penetration depth to maximum diameter as a function of compressive strength of the comet surface. Impact velocities are 1, 5, and 10.5 km s^{-1}. The red lines are obtained for the case of ρ_p = 2250 kg m^{-3}, Y_{pt} = 3.2 MPa, whereas the blue lines are obtained for the case of ρ_p = 1400 kg m^{-3}, Y_{pt} = 500 Pa. The light gray line shows the depth-to-diameter ratio of ~0.3 (White and Schenk, 2011).

for calculation of the bulb depth in Figure 3.15 (a), whereas Eqs. (3.13), (3.14), and (3.15), which were obtained crater scaling law, are used for it in Figure 3.15 (b). The light gray areas show the range of the compressive strength of the surface obtained in this study. The difference of the results of BD/D_{max} in Figure (a) and (b) in the range of the strength is only within a factor of 3 and the value of BD/D_{max} is smaller than ~0.3. Figure 3.16 shows the results of BD/D_{max} and PD/D_{max} as a function of impact velocity, at a constant compressive strength of the surface of 500 Pa as a representative value in the range of the strength obtained here. The difference of Figure 3.16 (a) and (b) is the difference of the use of the scaling laws for the bulb depth. The results of BD/D_{max} in Figure 3.16 (a) and (b) are almost all the same; The difference is within a factor of two in the velocity range from 2 to 12 km s^{-1}. Little change of the values of BD/D_{max} has been found at the impact-velocity range and it was $0.1 < BD/D_{\mathrm{max}} < 0.4$. If the surface strength is less than the strength that we assumed, the value of BD/D_{max} becomes smaller. These results suggest that craters on comets which look shallow can be created only by impact.

Note that craters on comets which looks like shallow could also possibly be due to viscous relaxation. Cheng and Dombard (2006) calculated the relaxation time scale of ice-surface topography as a function of comet temperature. When temperature of comet is 225 K, the relaxation time is less than 10^4 yr (for a grain size of comet less than 1 μm). The relaxation time decreases with increasing temperature. The derived temperature of comet Tempel 1 on the sunlit side varies from 260 ± 6 K to 329 ± 8 K (A'Hearn *et al.*, 2005), which is larger than 225 K. Thus impact craters formed on the comet would have been modified to those with smaller values of depth-to-diameter ratio. The degree of modification is depending on the detailed thermal history as well as composition and material properties.

Though all the results for BD/D_{max} in Figure 3.15 and 3.16 are larger than PD/D_{max}, Figure 3.16 suggests that the impactors would be captured on the crater bottom or below the crater when impactors have stronger strength and impact velocity of nearly or less than

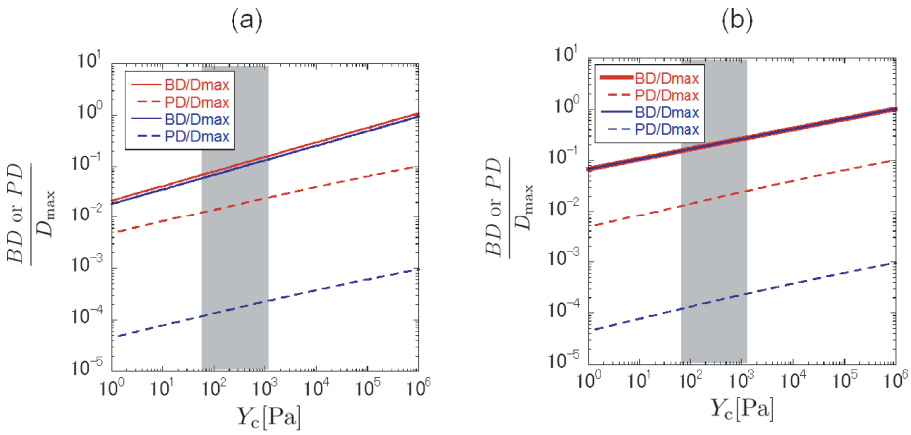

Figure 3.15: The ratio of bulb depth to maximum diameter and the ratio of penetration depth to maximum diameter as a function of compressive strength of the comet surface. Impact velocity is 10.5 km s^{-1}. The red lines are obtained for the case of ρ_p = 2250 kg m^{-3}, Y_{pt} = 3.2 MPa, whereas the blue lines are obtained for the case of ρ_p = 1400 kg m^{-3}, Y_{pt} = 500 Pa. The scaling relation between bulb depth and projectile-to-target density ratio is used for calculation of the bulb depth in (a), whereas the scaling relation obtained from the crater scaling law is used for calculation of the bulb depth in (b). The light gray area shows the compressive strength of Tempel 1 obtained in this study.

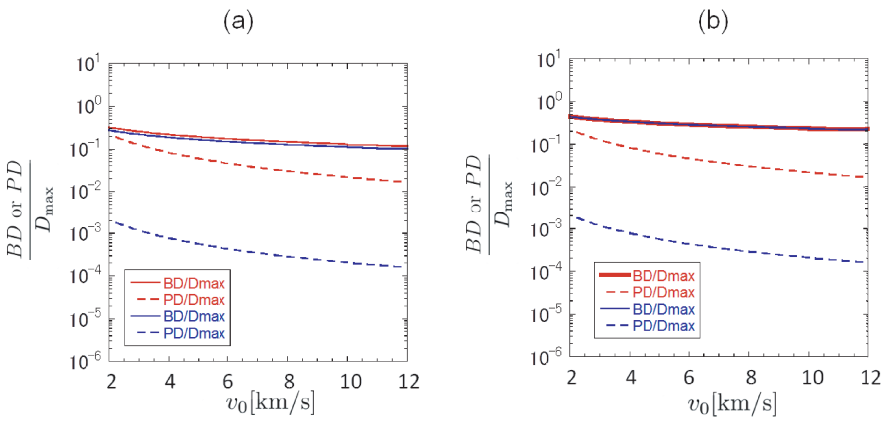

Figure 3.16: The ratio of bulb depth to maximum diameter and the ratio of penetration depth to maximum diameter as a function of impact velocity. The red lines are obtained for the case of ρ_p = 2250 kg m^{-3}, Y_{pt} = 3.2 MPa, whereas the blue lines are obtained for the case of ρ_p = 1400 kg m^{-3}, Y_{pt} = 500 Pa. The scaling relation between bulb depth and projectile-to-target density ratio is used for calculation of the bulb depth in (a), whereas the scaling relation obtained from the crater scaling law is used for calculation of the bulb depth in (b).

2 km s^{-1}.

3.4 Summary

We have conducted high-velocity impact experiments on gypsum targets with porosities of ~50%, pumice targets with those of 74%, and sintered glass-bead targets with those of 87% and 94%. The cavity dimensions, in particular the depth from the entrance hole to the maximum diameter, L_{max}, the maximum diameter, D_{max}, the bulb depth, *BD* were investigated. L_{max} is shown to increase with increasing characteristic length, L_0, which indicates that L_{max} depends on primarily the projectile-target density ratio with smaller contribution of the degree of projectile deformation or disruption. Empirical relation for the maximum diameter is obtained using non-dimensional parameters used for crater scaling. The empirical relation which is dependent on the projectile-to-target density ratio is obtained for the bulb depth.

We applied the scaling relation to icy bodies. The surface strength of comet Tempel 1 is estimated to be of the orders of 10^1–10^3 Pa. Our estimate narrowed the range of the comet strength which were previously estimated as not more than 10^3–10^4 Pa by Richardson *et al.* (2007). From the obtained compressive strength of the surface of Tempel 1, we estimated the grain size of the surface to be larger than 58 μm, assuming that the grains are monodisperse. It suggests that the larger dust size cannot be explained only by a simple cometesimal-formation model in which sub-micrometer-sized dust directly hit-and-stick and grow to comets, and some metamorphic events of the surface are necessary for the explanation.

We also calculated the ratio of bulb depth to the maximum diameter from the scaling relations, and it shows that craters on comets which look shallow can be created only by impact without activities after imapct, such as sublimation and viscous relaxation.

Chapter 4

Experimental study of catastrophic disruption of highly porous targets[*1]

4.1 Introduction

Recent numerical simulation shows that collisions of bodies characterized by different bulk densities and strengths may have occurred owing to the migration of giant planets. The Grand Tack model (Walsh *et al.*, 2012) suggests that both inner- and outer-orbit bodies were scattered and mixed following the inward and outward migrations of Jupiter and Saturn. The Nice model also implies that Kuiper Belt Objects were scattered and transported to the asteroid region when Jupiter and Saturn crossed their 1:2 mean-motion resonance (Gomes *et al.*, 2005).

Ryan *et al.* (1999) showed that the disruption threshold, Q^* (described in Section 1.4), for pure ice targets is smaller than those for silicate and metal targets. Setoh *et al.* (2010) used sintered glass-bead targets of ~40% porosity and various compressive strengths, and showed that Q^* increased with increasing target compressive strength. Love *et al.* (1993) indicated that the Q^* of sintered glass-bead targets increased with increasing target porosity.

[*1]An earlier version of this chapter has been published as:
Okamoto T., Nakamura A. M., and Hasegawa S. 2014. Impact Experiments on Highly Porous Targets: Cavity Morphology and Disruption Thresholds in the Strength Regime. *Planetary and Space Science, in press*

To understand the collisional evolution of highly porous bodies, it is necessary to understand the impact characteristics of targets with porosities in excess of those used in previous studies. In this study, impact experiments on sintered glass-bead targets with different porosities of up to 94% are conducted. The disruption thresholds of the high-porosity targets were analyzed. The results are compared with previous studies of porous targets of various materials.

4.2 Experiments

We prepared sintered hollow glass beads targets with porosities, ϕ, of 87% and 94%, which we refer to as fluffy87 and fluffy94, respectively. Normal, solid glass-bead targets with a porosity of 80% were also prepared ("fluffy80"). These sintered glass-bead targets were cylindrical in shape. Table 3.1 includes a summary of the target properties. Target dimensions and the impact conditions are listed in Table 4.1. We used targets of different aspect ratios (i.e., different diameter-to-height ratios), to examine the effect of the target shape on the degree of disruption. The targets were recovered after the shots, and the mass of the largest fragment, M_{L}, was determined. The results of the experiments are also presented in Table 4.1.

4.3 Results and discussoions

4.3.1 Disruption thresholds of targets

The ratio of the largest fragment mass, M_{L}, to the initial target mass, M_{t}, generally decreases with increasing energy density, Q. The energy density is defined by the initial projectile's kinetic energy divided by the sum of the target and projectile masses. When the target mass is much higher than that of the projectile, Q is approximately represented

Table 4.1: Experimental condition and result for target disruption

Run number	Target type	Target diam. (mm)	Target mass (g)	diam. /height	Impact velocity (km s^{-1})	Projectile material	Projectile size[a] (mm)	Projectile mass (mg)	M_L/M_t[b]
1105_D	fluffy94	63.3	55.3	0.49	4.29	Ti	3.2	75.4	0.66
1105_E	fluffy94	63.0	52.9	0.50	4.23	Ti	3.2	75.4	0.63
1109_E	fluffy80	60.5	195.8	0.47	4.17	Ti	3.2	75.4	0.44
1109_F	fluffy80	61.0	200.8	0.45	2.52	Basalt	D3.2×H2.0	49	0.84
1109_G	fluffy80	62.3	200.7	0.48	3.89	Basalt	D3.2×H2.0	51	0.74
1109_H	fluffy80	62.3	196.2	0.46	3.86	Ti	3.2	75.4	0.43
1109_Y	fluffy94	61.3	53.6	0.49	4.22	Basalt	D3.2×H2.0	51	0.23
1109_X	fluffy94	62.6	52.5	0.50	6.63	Basalt	D3.2×H2.0	50	0.12
1111_A	fluffy94	63.4	59.9	0.47	6.37	Ti	3.2	75.4	0.09
1111_R	fluffy87[c]	48.2	125.9	0.24	1.83	Ti	3.2	75.4	0.98[d]
1111_T	fluffy87	47.7	59.7	0.47	4.26	Ti	3.2	75.0	0.22
1111_U	fluffy87	47.5	60.5	0.47	6.18	Ti	3.2	75.0	0.16
1201_A	fluffy94	62.4	60.4	0.45	2.26	Ti	3.2	75.4	0.96
1201_D	fluffy94	62.3	59.6	0.45	3.28	Basalt	D3.2×H2.3	49.8	0.41
1204_H	fluffy94	62.4	61.9	0.44	2.30	Basalt	D3.2×H2.3	50.0	0.98[d]
1309_A	fluffy94	79.6	61.5	0.95	6.76	Ti	3.2	75	0.15
1309_B	fluffy94	79.5	61.8	0.94	3.09	Basalt	D3.2×H2.2	45	0.99[d]
1309_C	fluffy94	79.0	59.8	0.94	4.70	Ti	3.2	75	0.95
1312_D	fluffy87	60.6	75.7	0.78	6.41	Nylon	3.2	19	0.78
1403_A	fluffy87	59.4	71.4	0.79	4.30	Ti	3.2	75	0.24
1403_B	fluffy87	59.4	73.5	0.78	5.96	Ti	3.2	75	0.16
1403_D	fluffy87	61.3	71.2	0.82	7.00	Nylon	3.2	19	0.59

[a] Diameter for spherical projectiles; diameter (D) and height (H) for cylindrical projectiles.
[b] M_L/M_t: Ratio of largest fragment mass, M_L to the initial target mass, M_t.
[c] The 1111_R target has a different shape from the other fluffy87 targets; 48 mm in diameter, 203 mm in height, and 125.9 g in mass.
[d] The shot did not disrupt the targets. The M_L for this shot is the mass of the target, reduced by the excavated mass.

by

$$Q = \frac{\frac{1}{2} m_{\mathrm{p}} {v_0}^2}{M_{\mathrm{t}}}. \tag{4.1}$$

The threshold energy density for disruption, Q^*, is defined by the energy density that results in the largest remnant having half the mass of the target (Holsapple *et al.*, 2002). The ratio of the largest fragment mass versus the energy density is plotted for targets with different diameter/height ratios in Figure 4.1. The following relation is used for the fits to the data:

$$Q = 10^a \left(\frac{M_{\mathrm{L}}}{M_{\mathrm{t}}} \right). \tag{4.2}$$

The best-fitting results are shown in Table 4.2, along with their Q^* values. Each Q^* value is on the order of kilojoules per kilogram, and is thus larger than those of pure ice targets, ~35 J kg^{-1} (Arakawa, 1999), ice-fragments targets, 82 J kg^{-1} (Giblin *et al.*, 2004), and basalt targets, 0.74 kJ kg^{-1} (Fujiwara *et al.*, 1977). The values are, however, similar to those of sintered glass-bead targets with a porosity of 60% (3.8 kJ kg^{-1}), ~40% (1.5 and 3.3 kJ kg^{-1}) (the two values correspond to targets of two different static strengths), and 5% (1.3 kJ kg^{-1}) (Love *et al.*, 1993). The Q^* values for targets with diameter/height ratios of ~0.9 and ~0.8 are slightly larger than Q^* for targets with elongated shapes (diameter/height ~0.5), within a factor of ~2.

Table 4.2: Curve-fitting results

Target type	Ratio[1]	a[2]	b[2]	Q^*(kJ kg^{-1})
fluffy94	~0.5	3.60±0.14	-0.73±0.25	6.6±2.1
fluffy94	~0.9	3.83±0.30	-0.76±0.63	11±8.0
fluffy87	<~0.5	2.97±0.07	-1.72±0.11	3.1±0.5
fluffy87	~0.8	3.63±0.07	-0.71±0.13	7.0±1.1
fluffy80	~0.5	2.89±0.16	-1.60±0.61	2.4±0.9

[1] Ratio of target diameter to height.
[2] a and b are constants in Eq. (4.2).

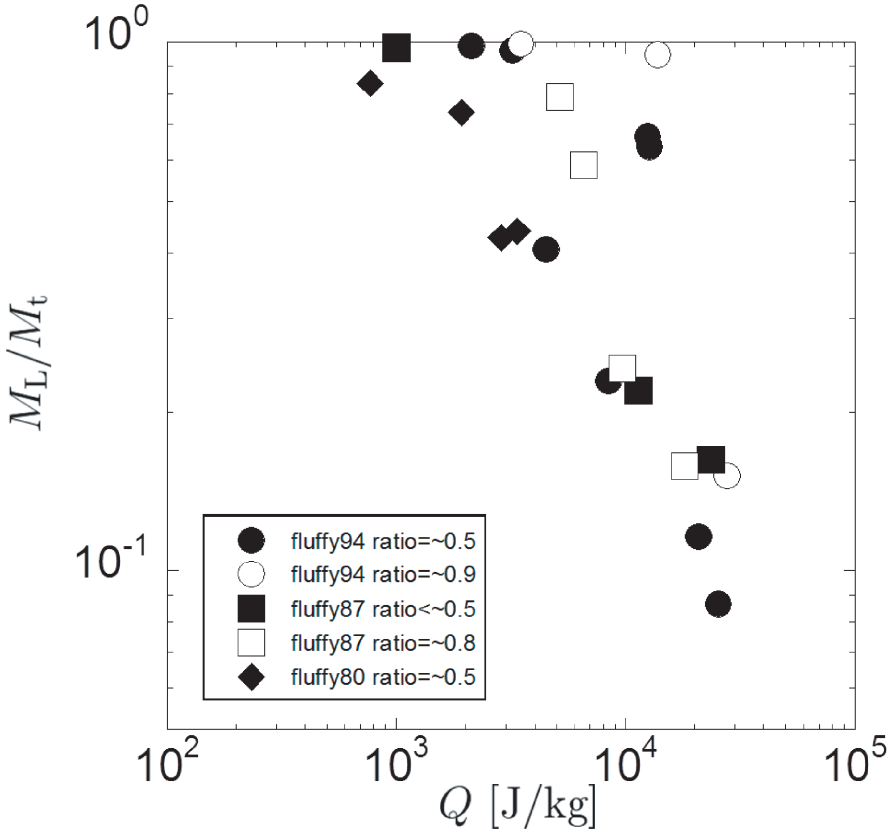

Figure 4.1: Largest fragment mass ratio versus energy density. Solid symbols are for targets with diameter/height ratio of ~0.5, while open symbols relate to targets with ratios of ~0.9 (fluffy94) and ~0.8 (fluffy87).

The present results are compared with previous data of targets composed of various materials and characterized by a range of porosities. Figure 4.2 shows Q^* versus target compressive strength. The values for the Murchison target from Miura *et al.* (2008) and that for a pure ice target derived from the empirical equation in Arakawa and Tomizuka (2004) are adopted as the compressive strengths of the Murchison (Flynn *et al.*, 2009) and pure ice targets (Arakawa, 2002), respectively. The compressive strengths for other materials were given in each paper. According to Flynn *et al.* (2009), Q^* for the Murchison target is at least as strong as that for the anhydrous meteorite targets, for which Flynn and Durda (2004) determined $Q^* \sim 1400$ J kg^{-1}. We adopted this value as the lower limit to Q^* for the Murchison targets. Q^* tends to increase with increasing target strength. Q^* also tends to increase with increasing porosity at a given compressive strength. This tendency is probably due to the different efficiencies of shock attenuation.

We will now discuss the porosity dependence using a non-dimensional catastrophic disruption threshold, defined as $\rho_t Q^*/Y$. Compressive strength, Y_c is substituted for Y here. Figure 4.3 shows the relation between the non-dimensional disruption threshold and filling factor, f ($f = 1 - \phi/100$). The non-dimensional disruption threshold increases with increasing porosity. Solid symbols show the results of experiments for impact velocities larger than 1 km s^{-1}, while open symbols refer to impact velocities smaller than 1 km s^{-1}. The $\rho_t Q^*/Y$ ratio is within approximately one order of magnitude for a given porosity for experiments of different impact velocities and target sizes. No apparent dependence on impact velocities was found.

A non-dimensional strength parameter, Π_s, based on the coupling-parameter concept has been proposed (Holsapple and Housen, 1986; Housen and Holsapple, 1990),

$$\Pi_s = Q\left(\frac{Y}{\rho_t}\right)^{3\mu/(\lambda-2)} R'^{-3\mu(\lambda+\tau)/(\tau-2)} v_0{}^{3\mu-2}\left(\frac{\rho_t}{\rho_p}\right)^{1-3\nu}, \tag{4.3}$$

where λ and τ are dimensionless material constants and R' is the target radius. The largest

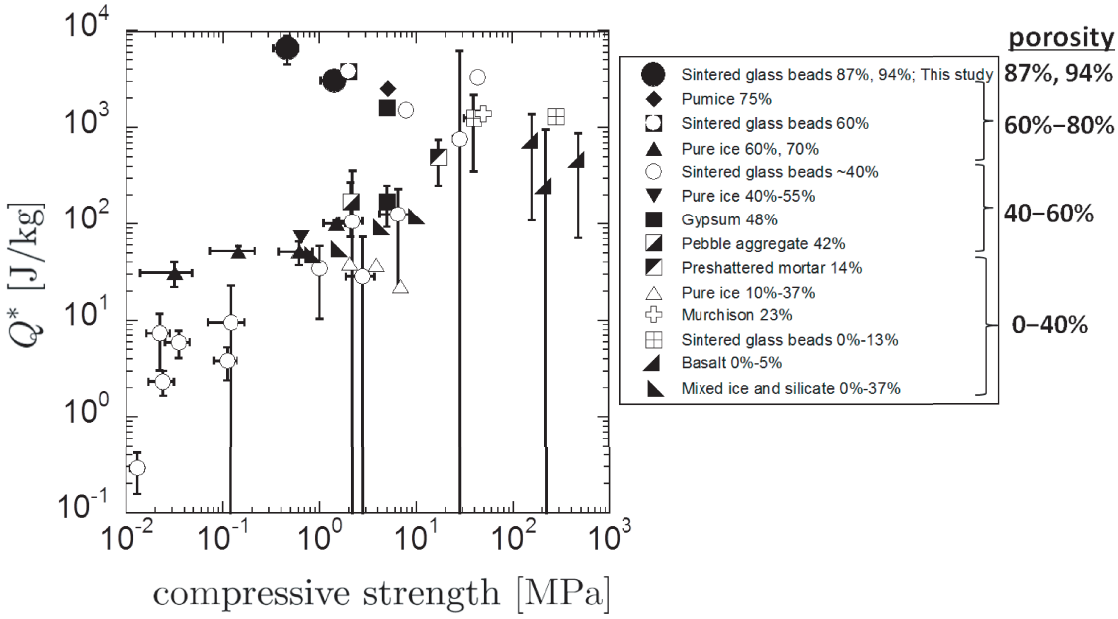

Figure 4.2: Disruption threshold, Q^*, versus compressive strength of the targets from various studies. Sintered glass-bead targets (ϕ= 60%, ~40%, 0%–13%; Love *et al.*, 1993; Setoh *et al.*, 2010), pumice targets (Nakamura *et al.*, 2009), pure ice targets (Arakawa, 2002; Shimaki and Arakawa, 2012), mixed ice and silicate targets (Arakawa and Tomizuka, 2004), gypsum targets (Kawakami *et al.*, 1991), pebble and preshattered mortar targets (Ryan *et al.*, 1991), Murchison (Flynn *et al.*, 2009), and basalt targets (Fujiwara *et al.*, 1977; Matsui *et al.*, 1982; Takagi *et al.*, 1984).

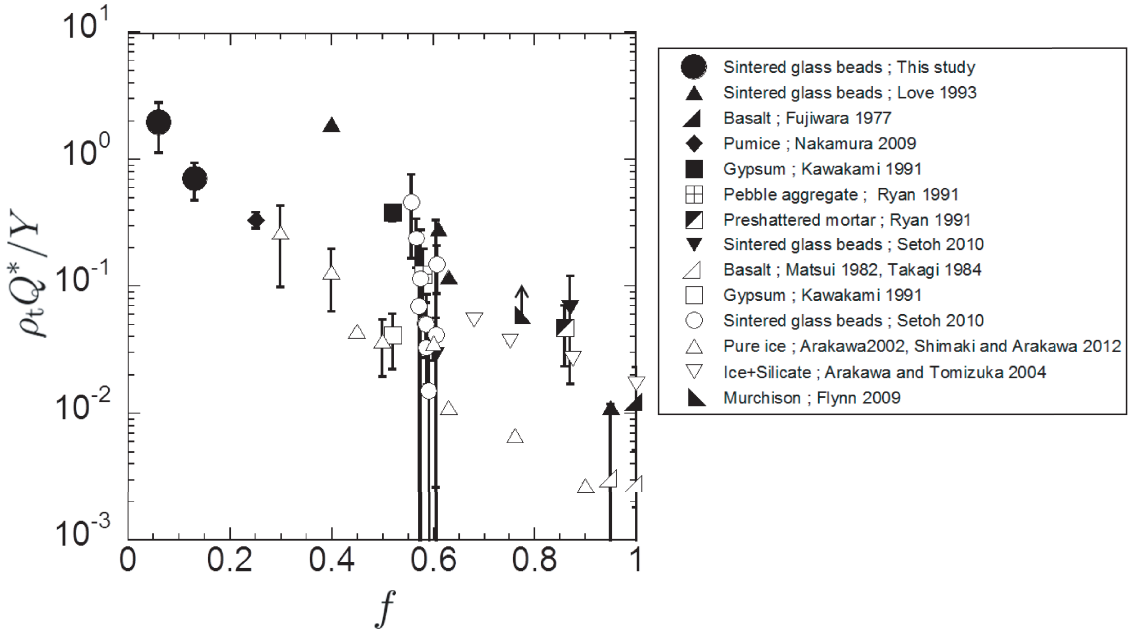

Figure 4.3: Non-dimensional disruption threshold, $\rho_t Q^*/Y$, versus filling factor, f, from various studies. The references in this figure are the same as those used in Figure 4.2. Solid symbols show results from experiments for impact velocities > 1 km s^{-1} (higher velocities), while open symbols show those for impact velocities smaller than 1 km s^{-1} (lower velocities). Solid and open squares (preshattered mortar) show results for a wide velocity range of 0.09–5.61 km s^{-1}.

fragment mass ratio is represented by

$$\frac{M_{\mathrm{L}}}{M_{\mathrm{t}}} = F(\Pi_{\mathrm{s}}). \tag{4.4}$$

The catastrophic disruption threshold is obtained by adopting $M_{\mathrm{L}}/M_{\mathrm{t}} = 0.5$, so that $F(\Pi_{\mathrm{s}}{}^{*}) = \text{constant}$; i.e.,

$$\Pi_{\mathrm{s}}{}^{*} = \text{constant}. \tag{4.5}$$

Assuming that $\nu = 1/3$ and that the strength of the target material does not depend on either the size scale or the strain rate (i.e., both dimensionless material constants λ and τ are zero), the strength parameter at the catastrophic disruption threshold, $\Pi_{\mathrm{s}}{}^{*}$, is simplified to

$$\Pi_{\mathrm{s}}{}^{*} = Q^{*}\left(\frac{Y}{\rho_{\mathrm{t}}}\right)^{-3\mu/2} v_0{}^{3\mu-2}. \tag{4.6}$$

Values of $\Pi_{\mathrm{s}}{}^{*}$ have been calculated for the present data as well as for data presented in previous studies. In Eq. (4.6) we substituted the approximate mean values of the velocity ranges pertaining to each experiment for the impact velocity. Housen and Holsapple (2003) expected that μ tends toward a scaling limit of 1/3 with increasing porosity, so that we simply regard μ as a function of porosity,

$$\mu = \frac{1}{3} + \frac{1}{3}\left(1 - \frac{\phi}{100}\right) = \frac{1+f}{3}. \tag{4.7}$$

The value of μ for porosities of 65%–69% obtained from this simple equation covers the range 0.44–0.45, which is close to $\mu \approx 0.4$ for gypsum targets with porosities of 65%–69%, as determined from impact experiments focusing on catastrophic disruption (Nakamura *et al.*, 2014). Figure 4.4 shows the relationship between $\Pi_{\mathrm{s}}{}^{*}$ and filling factor, f. As in Figure 4.3, solid symbols show experimental results for higher impact velocities, while open symbols pertain to lower impact velocities. The values of $\Pi_{\mathrm{s}}{}^{*}$ are roughly constant (approximately 0.02), and they are found within one order of magnitude irrespective of porosity. The result for the Murchison target (Flynn *et al.*, 2009), which is a natural product from the solar system, is also consistent with this relation.

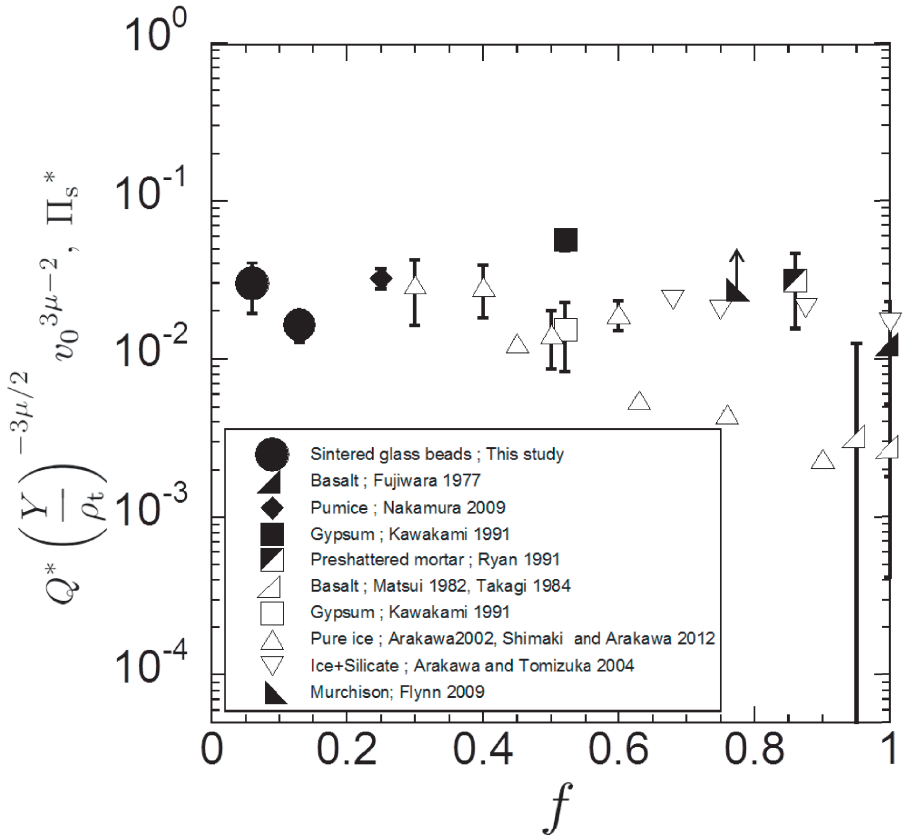

Figure 4.4: Strength parameter at the catastrophic disruption threshold, Π_s^* (Housen and Holsapple, 1990) versus filling factor, f, with results of various studies. Solid symbols show results from experiments for impact velocities > 1 km s^{-1} (higher velocities), while open symbols show those for impact velocities < 1 km s^{-1} (lower velocities). Solid and open squares (preshattered mortar) show results for a wide velocity range of 0.09–5.61 km s^{-1}.

4.4 Summary

We have conducted high-velocity impact experiments on sintered glass-bead targets with porosities of 80%, 87%, and 94%. The target disruption thresholds, Q^*, are investigated. No clear porosity dependence is observed for fluffy80, fluffy87, and fluffy94 targets with a diameter/height ratio of ~0.5. Each Q^* value is on the order of kilojoules per kilogram, which is larger than the values appropriate for pure ice (Arakawa, 1999) and basalt (Fujiwara *et al.*, 1977) determined from high-velocity impact experiments. Q^* for targets with diameter/height ratios of ~0.9 and ~0.8 are slightly larger than Q^* for targets with more elongated shapes (diameter/height ~0.5), within a factor of ~2. We investigated the relationship between the non-dimensional disruption threshold, $\rho_t Q^*/Y$, and porosity. We showed that the values of $\rho_t Q^*/Y$ for various materials with different impact velocities and target sizes are located within approximately one order of magnitude of each other for a given porosity. The strength parameter at the catastrophic disruption threshold $\Pi_s{}^*$, proposed by (Housen and Holsapple, 1990), is also calculated. If we assume a linear relationship, $\mu = 2/3 - \phi/300 = (1 + f)/3$, the values of $\Pi_s{}^*$ are shown to be roughly constant and they almost all fall within one order of magnitude, although the porosity ranges from 0 to 94%.

Chapter 5

General summary

In order to investigate the penetration process, cratering process and the disruption of highly porous bodies in the strength regime, impact experiments were performed on targets with porosities larger than 50%. We compare our results with the results of previous studies, and examine the impact phenomena with wider range in porosity in the parameter space of strength regime.

In chapter 2, we examined the penetration process of the projectiles. Impact-penetration experiments were conducted using metal spheres and basalt cylinders for projectiles. We prepared sintered glass-bead targets with porosities of 94%, 87%, and 80%. Impact velocities ranged from 1.6 to 7.2 km s^{-1}. A flash X-ray imaging system were used to observe projectile deceleration processes. Two types of track morphologies were observed. One is a “carrot”-shaped track, which is a thin and long shape track. The other one is a “bulb”-shape track which is thick and short with/without tails. The transition from carrot to bulb shape occurs when the initial dynamic pressure exceeds approximately 20 times the projectile’s tensile strength. The compacted region due to impact was observed on flash X-ray images. It was found that the almost all material was transported to the compacted region to form a cavity and only little was ejected. We constructed a simple model for projectile deceleration; when a projectile collides with a target, the projectile disrupt, and the largest fragment of the projectile decelerates in the target by inertial drag and drag that is propor-

tional to the target strength. This model roughly reproduces the experimental results with respect to penetration depth for projectiles that did not experience severe deformation and fragmentation. We applied this penetration model to icy bodies which were homogeneous on much smaller scales than the impacting dust particles with different bulk porosities and estimated the penetration depth of silicate dust. The predicted depth showed that the dust penetration was only approximately 100 times the projectile diameter, even for bodies with 90% bulk porosity.

In chapter 3, we examined the craters formed on porous targets in strength regime in order to obtain the scaling relation for crater dimensions, i.e., diameter and depth of cavity. We conducted high-velocity impact experiments on gypsum targets with porosities of ~50%, pumice targets with those of 74%, and sintered glass-bead targets with those of 87%, and 94%. The cavity dimensions, in particular the depth from the entrance hole to the maximum diameter, $L_{\max}$, the maximum diameter, $D_{\max}$, the bulb depth, BD were investigated. We compared our results with previous studies. The results show that $L_{\max}$ depends on primarily the projectile-target density ratio with smaller contribution of the degree of projectile deformation or disruption. Empirical relation for the maximum diameter is obtained using non-dimensional parameters used for crater scaling. The empirical relation which is dependent on the projectile-to-target density ratio is obtained for the bulb depth. We applied the scaling relations to icy bodies. The surface strength of comet Tempel 1 is estimated to be of the orders of 10^1–10^3 Pa. We narrowed down the range of the strength values which were previously estimated as not more than 10^3–10^4 Pa by Richardson *et al.* (2007). We presented the possibility of formation of shallow craters on comets due only to impacts.

In chapter 4, the target disruption thresholds, Q^*, for sintered glass-bead targets with porosities of 80%, 87% and 94%, were determined. We also used targets of different aspect ratios to examine the effect of the target shape on the degree of disruption. Each Q^* value

for sintered glass-bead targets with the same diameter-to-hgeight ratios of ~0.5 are on the order of kilojoules per kilogram, which is larger than the values appropriate for pure ice (Arakawa, 1999) and basalt (Fujiwara *et al.*, 1977) determined from high-velocity impact experiments. Q^* for targets with diameter/height ratios of ~0.9 and ~0.8 are slightly larger than Q^* for targets with more elongated shapes (diameter/height ~0.5), within a factor of ~2. We investigated the relationship between the non-dimensional disruption threshold, $\rho_t Q^*/Y$, and porosity. We showed that the values of $\rho_t Q^*/Y$ for various materials with different impact velocities and target sizes are located within approximately one order of magnitude of each other for a given porosity. The strength parameter at the catastrophic disruption threshold $\Pi_s{}^*$, proposed by Housen and Holsapple (1990), is also calculated. If we assume a linear relationship, $\mu = 2/3 - \phi/300 = (1 + f)/3$, the values of $\Pi_s{}^*$ are shown to be roughly constant and they almost all fall within one order of magnitude, although the porosity ranges from 0 to 94%.

While we obtained scaling relations for crater sizes and disruption threshold of the targets, many physical processes are not yet well understood. In order to convince the validity of extrapolation of the scaling relations obtained from the laboratory scale to the scale of small bodies, it is necessary to find out physical interpretations of the scaling relations. Comparing the strength of targets with attenuated shock pressure may be one of keys to find it. For example, if the attenuated pressure nearly equals to the target strength, the growth of the cavity is considered to be finished (Kadono *et al.*, 2012), whreas if the most attenuated pressure in the target, i.e., the pressure at the farthest point from an impact point, is much larger than the target strength, the target must be disrupted catastrophically (Mizutani *et al.*, 1990). Shock attenuation mechanisms of highly porous targets, however are not well-studied nor well-understood, so we firstly should study it experimentally, such as a shock attenuation rate in highly porous targets.

We should also compare our results with a numerical simulation in order to understand better the effect of porosity. Taking advantages of combination of experimental and numerical approaches, we can reveal the physical mechanisms of cratering on highly porous targets. ESA's space craft Rosseta and its lander, Philae, which are performing detailed studies of comet 67P/Churyumov-Gerasimenko, will also give us the physical properties of a comet nucleus, and improve our understanding of crater formation on small bodies.

Acknowledgments

I am extremely grateful to A. M. Nakamura for providing many helpful comments and suggestions for this dissertation. I appreciate M. Arakawa, Y. Yasui, and other members in the Experimental Planetary Science Laboratory for their valuable discussions and suggestions. I also thank S. Sugita and Y. Sekine for many enlightening discussions. I also thank K. Sangen for his preparation of experimental equipments, S. Hasegawa, K. Kurosawa, M. Tabata, A. Suzuki, and T. Hirai, for performing the experiments at ISAS/JAXA, and A. Tsuchiyama, K. Ikezaki, and A. Shimada for giving us an opportunity to obtain images using the micro-X-ray tomography instrument. I wish to express my gratitude to A. Higuchi, S. Urakawa, K. Kitazato, T. Morota, and C. Güttler for their encouragement. Last but not least, I thank my parents and friends for their support and encouragement.

Bibliography

A'Hearn, M. F., M. J. S. Belton, W. A. Delamere, J. Kissel, K. P. Klaasen, L. A. McFadden, K. J. Meech, H. J. Melosh, P. H. Schultz, J. M. Sunshine, P. C. Thomas, J. Veverka, D. K. Yeomans, M. W. Baca, I. Busko, C. J. Crockett, S. M. Collins, M. Desnoyer, C. A. Eberhardy, C. M. Ernst, T. L. Farnham, L. Feaga, O. Groussin, D. Hampton, S. I. Ipatov, J.-Y. Li, D. Lindler, C. M. Lisse, N. Mastrodemos, W. M. Owen, J. E. Richardson, D. D. Wellnitz, and R. L. White 2005. Deep Impact: excavating comet Tempel 1. *Science* **310**, 258–264.

Arakawa, M. 1999. Collisional Disruption of Ice by High-Velocity Impact. *Icarus* **142**, 34–45.

Arakawa, M. 2002. Impact Experiments on Porous Icy-Silicate Cylindrical Blocks and the Implication for Disruption and Accumulation of Small Icy Bodies. *Icarus* **158**, 516–531.

Arakawa, M., and D. Tomizuka 2004. Ice—silicate fractionation among icy bodies due to the difference of impact strength between ice and ice—silicate mixture. *Icarus* **170**, 193–201.

Blum, J., and R. Schräpler 2004. Structure and mechanical properties of high-porosity macroscopic agglomerates formed by random ballistic deposition. *Physical Review Letters* **93**, 115503 (1–4).

Blum, J., R. Schrapler, B. J. R. Davidsson, and J. M. Trigo Rodriguez 2006. The Physics of

Protoplanetesimal Dust Agglomerates. I. Mechanical Properties and Relations to Primitive Bodies in the Solar System. *The Astrophysical Journal* **652**, 1768–1781.

Bockelee-Morvan, D., D. Gautier, F. Hersant, J.-M. Hure, and F. Robert 2002. Turbulent radial mixing in the solar nebula as the source of crystalline silicates in comets.

Brad, D. J., D. P. Cruikshank, and R. N. Clark 2012. Compositional analysis of Hyperion with the Cassini Visual and Infrared Mapping Spectrometer. *Icarus* **220**, 752–776.

Brownlee, D., D. Joswiak, and G. Matrajt 2012. Overview of the rocky component of Wild 2 comet samples: Insight into the early solar system, relationship with meteoritic materials and the differences between comets and asteroids. *Meteoritics & Planetary Science* **47**, 453–470.

Brownlee, D., P. Tsou, J. Aléon, C. M. O. Alexander, T. Araki, S. Bajt, G. A. Baratta, R. Bastien, P. Bland, P. Bleuet, J. Borg, J. P. Bradley, A. Brearley, F. Brenker, S. Brennan, J. C. Bridges, N. D. Browning, J. R. Brucato, E. Bullock, M. J. Burchell, H. Busemann, A. Butterworth, M. Chaussidon, A. Cheuvront, M. Chi, M. J. Cintala, B. C. Clark, S. J. Clemett, G. Cody, L. Colangeli, G. Cooper, P. Cordier, C. Daghlian, Z. Dai, L. D'Hendecourt, Z. Djouadi, G. Dominguez, T. Duxbury, J. P. Dworkin, D. S. Ebel, T. E. Economou, S. Fakra, S. A. J. Fairey, S. Fallon, G. Ferrini, T. Ferroir, H. Fleckenstein, C. Floss, G. Flynn, I. A. Franchi, M. Fries, Z. Gainsforth, J.-P. Gallien, M. Genge, M. K. Gilles, P. Gillet, J. Gilmour, D. P. Glavin, M. Gounelle, M. M. Grady, G. A. Graham, P. G. Grant, S. F. Green, F. Grossemy, L. Grossman, J. N. Grossman, Y. Guan, K. Hagiya, R. Harvey, P. Heck, G. F. Herzog, P. Hoppe, F. Hörz, J. Huth, I. D. Hutcheon, K. Ignatyev, H. Ishii, M. Ito, D. Jacob, C. Jacobsen, S. Jacobsen, S. Jones, D. Joswiak, A. Jurewicz, A. T. Kearsley, L. P. Keller, H. Khodja, A. L. D. Kilcoyne, J. Kissel, A. Krot, F. Langenhorst, A. Lanzirotti, L. Le, L. A. Leshin, J. Leitner, L. Lemelle,

H. Leroux, M.-C. Liu, K. Luening, I. Lyon, G. Macpherson, M. A. Marcus, K. Marhas, B. Marty, G. Matrajt, K. McKeegan, A. Meibom, V. Mennella, K. Messenger, S. Messenger, T. Mikouchi, S. Mostefaoui, T. Nakamura, T. Nakano, M. Newville, L. R. Nittler, I. Ohnishi, K. Ohsumi, K. Okudaira, D. A. Papanastassiou, R. Palma, M. E. Palumbo, R. O. Pepin, D. Perkins, M. Perronnet, P. Pianetta, W. Rao, F. J. M. Rietmeijer, F. Robert, D. Rost, A. Rotundi, R. Ryan, S. A. Sandford, C. S. Schwandt, T. H. See, D. Schlutter, J. Sheffield-Parker, A. Simionovici, S. Simon, I. Sitnitsky, C. J. Snead, M. K. Spencer, F. J. Stadermann, A. Steele, T. Stephan, R. Stroud, J. Susini, S. R. Sutton, Y. Suzuki, M. Taheri, S. Taylor, N. Teslich, K. Tomeoka, N. Tomioka, A. Toppani, J. M. Trigo-Rodríguez, D. Troadec, A. Tsuchiyama, A. J. Tuzzolino, T. Tyliszczak, K. Uesugi, M. Velbel, J. Vellenga, E. Vicenzi, L. Vincze, J. Warren, I. Weber, M. Weisberg, A. J. Westphal, S. Wirick, D. Wooden, B. Wopenka, P. Wozniakiewicz, I. Wright, H. Yabuta, H. Yano, E. D. Young, R. N. Zare, T. Zega, K. Ziegler, L. Zimmerman, E. Zinner, and M. Zolensky 2006. Comet 81P/Wild 2 under a microscope. *Science* **314**, 1711–1716.

Burchell, M. J., S. A. J. Fairey, P. Wozniakiewicz, D. E. Brownlee, F. Hörz, A. T. Kearsley, T. H. See, P. Tsuo, A. Westphal, S. F. Green, J. M. Trigo-Rodríguez, and G. Domingúez 2008. Characteristics of cometary dust tracks in Stardust aerogel and laboratory calibrations. *Meteoritics & Planetary Science* **40**, 23–40.

Cheng, A. F., and A. J. Dombard 2006. Viscous relaxation on comets. *Icarus* **184**, 584–588.

Ciesla, F. J. 2007. Outward transport of high-temperature materials around the midplane of the solar nebula. *Science* **318**, 613–615.

Cintala, M. J. 1981. Meteoroid impact into short-period comet nuclei. *Nature* **291**, 134–136.

Consolmagno, G., D. Britt, and R. Macke 2008. The significance of meteorite density and porosity. *Chemie der Erde - Geochemistry* **68**, 1–29.

Cruikshank, D. P., J. B. Dalton, C. M. Dalle Ore, J. Bauer, K. Stephan, G. Filacchione, A. R. Hendrix, C. J. Hansen, A. Coradini, P. Cerroni, F. Tosi, F. Capaccioni, R. Jaumann, B. J. Buratti, R. N. Clark, R. H. Brown, R. M. Nelson, T. B. McCord, K. H. Baines, P. D. Nicholson, C. Sotin, A. W. Meyer, G. Bellucci, M. Combes, J.-P. Bibring, Y. Langevin, B. Sicardy, D. L. Matson, V. Formisano, P. Drossart, and V. Mennella 2007. Surface composition of Hyperion. *Nature* **448**, 54–56.

Cuzzi, J. N., R. C. Hogan, and K. Shariff 2008. Toward planetesimals: Dense chondrule clumps in the protoplanetary nebula. *The Astrophysical Journal* **687**, 1432–1447.

Davidsson, B., and P. Gutierrez 2005. Nucleus properties of Comet 67P/Churyumov—Gerasimenko estimated from non-gravitational force modeling. *Icarus* **176**, 453–477.

Davis, D. R., C. R. Chapman, R. Greenberg, S. J. Weidenschilling, and A. W. Harris 1979. *Collisional evolution of asteroids - Populations, rotations, and velocities*, pp. 528–557.

Farinella, P., and D. R. Davis 1996. Short-Period Comets: Primordial Bodies or Collisional Fragments? *Science* **273**, 938–941.

Flynn, G. J., and D. D. Durda 2004. Chemical and mineralogical size segregation in the impact disruption of inhomogeneous, anhydrous meteorites. *Planetary and Space Science* **52**, 1129–1140.

Flynn, G. J., D. D. Durda, L. E. Sandel, J. W. Kreft, and M. M. Strait 2009. Dust production from the hypervelocity impact disruption of the Murchison hydrous CM2 meteorite: Implications for the disruption of hydrous asteroids and the production of interplanetary dust. *Planetary and Space Science* **57**, 119–126.

Fujii, Y., and A. M. Nakamura 2009. Compaction and fragmentation of porous gypsum targets from low-velocity impacts. *Icarus* **201**, 795–801.

Fujiwara, A. 1982. Complete fragmentation of the parent bodies of Themis, Eos, and Koronis families. *Icarus* **52**, 434–443.

Fujiwara, A., G. Kamimoto, and A. Tsukamoto 1977. Destruction of basaltic bodies by high-velocity impact. *Icarus* **31**, 277–288.

Gault, D. E., and J. A. Wedekind 1969. The destruction of tektites by micrometeoroid impact. *Journal of Geophysical Research* **74**, 6780–6794.

Giblin, I., D. R. Davis, and E. Ryan 2004. On the collisional disruption of porous icy targets simulating Kuiper belt objects. *Icarus* **171**, 487–505.

Gomes, R., H. F. Levison, K. Tsiganis, and A. Morbidelli 2005. Origin of the cataclysmic Late Heavy Bombardment period of the terrestrial planets. *Nature* **435**, 466–469.

Greenberg, J. 1998. Making a comet nucleus. *Astronomy and Astrophysics* **380**, 375–380.

Greenberg, R., and W. K. Hartmann 1977. Impact Strength: A Fundamental Parameter of Collisional Evolution. *Bulletin of the American Astronomical Society*, 455.

Greenwood, N., and A. Earnshaw 1984. *Chemistry of the elements*. Pergamon Press.

Harker, D. E., C. E. Woodward, and D. H. Wooden 2005. The dust grains from 9P/Tempel 1 before and after the encounter with Deep Impact. *Science* **310**, 278–280.

Hartmann, W. K. 1980. Continued Low-Velocity Impact Experiments at AMES Vertical Gun Facility: Miscellaneous Results. In *Lunar and Planetary Science Conference*, pp. 404–406.

Hiraoka, K. 2008. *Experimental Study of the Impact Cratering Process in the Strength Regime*. Doctral dissertation, Graduate School of Science and Technology, Kobe University.

Holsapple, K. 1993. The scaling of impact processes in planetary sciences. *Annual Review of Earth and Planetary Sciences* **21**, 333–373.

Holsapple, K., I. Giblin, K. Housen, A. Nakamura, and E. Ryan 2002. Asteroid Impacts: Laboratory Experiments and Scaling Laws. *Asteroids III*, 443–462.

Holsapple, K., and R. M. Schmidt 1982. On the scaling of crater dimensions. II - Impact processes. **87**, 1849–1870.

Holsapple, K. A., and K. R. Housen 1986. Scaling laws for the catastrophic collisions of asteroids. *Mem. Soc. Astron.* **57**, 65–85.

Holsapple, K. A., and R. M. Schmidt 1987. Point source solutions and coupling parameters in cratering mechanics. *Journal of Geophysical Research* **92**, 6350–6376.

Hörz, F., R. Bastien, J. Borg, J. P. Bradley, J. C. Bridges, D. E. Brownlee, M. J. Burchell, M. Chi, M. J. Cintala, Z. R. Dai, Z. Djouadi, G. Dominguez, T. E. Economou, S. a. J. Fairey, C. Floss, I. a. Franchi, G. a. Graham, S. F. Green, P. Heck, P. Hoppe, J. Huth, H. Ishii, A. T. Kearsley, J. Kissel, J. Leitner, H. Leroux, K. Marhas, K. Messenger, C. S. Schwandt, T. H. See, C. Snead, F. J. Stadermann, T. Stephan, R. Stroud, N. Teslich, J. M. Trigo-Rodríguez, a. J. Tuzzolino, D. Troadec, P. Tsou, J. Warren, A. Westphal, P. Wozniakiewicz, I. Wright, and E. Zinner 2006. Impact features on Stardust: implications for comet 81P/Wild 2 dust. *Science* **314**, 1716–1719.

Hörz, F., M. J. Cintala, T. H. See, and K. Nakamura-Messenger 2009. Penetration tracks in aerogel produced by Al 2 O 3 spheres. *Meteoritics & Planetary Science 44*(9), 1243–1264.

Housen, K. R., and K. A. Holsapple 1990. On the fragmentation of asteroids and planetary satellites. *Icarus* **84**, 226–253.

Housen, K. R., and K. A. Holsapple 1999. Scale Effects in Strength-Dominated Collisions of Rocky Asteroids. *Icarus* **33**, 21–33.

Housen, K. R., and K. A. Holsapple 2003. Impact cratering on porous asteroids. *Icarus* **163**, 102–119.

Housen, K. R., and K. A. Holsapple 2011. Ejecta from impact craters. *Icarus* **211**, 856–875.

Howard, A. D., J. M. Moore, P. M. Schenk, O. L. White, and J. Spencer 2012. Sublimation-driven erosion on Hyperion: Topographic analysis and landform simulation model tests. *Icarus* **220**, 268–276.

Ishibashi, T., A. Fujiwara, and N. Fujii 1990. Penetration of hypervelocity projectile into foamed polystyrene. *Japanese Journal of Applied Physics* **29**, 2543–2549.

Israelachvili, J. 1992. *Intermolecular and Surface Forces, Second Edition*. Academic Press.

Ivanov, B., D. Deniem, and G. Neukum 1997. Implementation of dynamic strength models into 2D hydrocodes: Applications for atmospheric breakup and impact cratering. *International Journal of Impact Engineering* **20**, 411–430.

Kadono, T., and A. Fujiwara 2005. Cavity and crater depth in hypervelocity impact. *International Journal of Impact Engineering* **31**, 1309–1317.

Kadono, T., R. Niimi, K. Okudaira, S. Hasegawa, M. Tabata, and A. Tsuchiyama 2012. Penetration into low-density media: In situ observation of penetration process of various projectiles. *Icarus* **221**, 587–592.

Kataoka, A., H. Tanaka, S. Okuzumi, and K. Wada 2013. Fluffy dust forms icy planetesimals by static compression. *Astronomy & Astrophysics* **557**, L4.

Kawai, N., K. Tsurui, S. Hasegawa, and E. Sato 2010. Single microparticle launching method using two-stage light-gas gun for simulating hypervelocity impacts of micrometeoroids and space debris. *Review of Scientific Instruments* **81**, 115105 (4 pages).

Kawakami, S., Y. Kanaori, A. Fujiwara, M. Arakawa, M. Kato, H. Mizutani, P. Cerroni, and F. Capaccioni 1991. An experimental study of impact fracturing of small planetary bodies in the Solar System with an application to Phobos. *Astronomy & Astrophysics* **241**, 233–242.

Kaye, G., and T. Laby 1986. *Tables of physical and chemical constants and some mathematical functions*. Longman.

Kearsley, A. T., M. J. Burchell, M. C. Price, M. J. Cole, P. J. Wozniakiewicz, H. a. Ishii, J. P. Bradley, M. Fries, and N. J. Foster 2012. Experimental impact features in Stardust aerogel: How track morphology reflects particle structure, composition, and density. *Meteoritics & Planetary Science* **47**, 737–762.

Levison, H., and M. Duncan 1997. From the Kuiper Belt to Jupiter-Family Comets: The Spatial Distribution of Ecliptic Comets. *Icarus* **127**, 13–32.

Love, S. G., F. Hörz, and D. E. Brownlee 1993. Target Porosity Effects in Impact Cratering and Collisional Disruption. *Icarus* **105**, 216–224.

Machii, N., and A. M. Nakamura 2011. Experimental study on static and impact strength of sintered agglomerates. *Icarus* **211**, 885–893.

Manhani, L. G. B., L. C. Pardini, and F. Levy Neto 2007. Assessement of tensile strength of graphites by the Iosipescu coupon test. *Materials Research* **10**, 233 – 239.

Matsui, T., T. Waza, and S. Suzuki 1982. Laboratory simulation of planetesimal collision. *Journal of Geophysical Research* **87**, 10,968–10,982.

McKeegan, K. D., J. Aléon, J. Bradley, D. Brownlee, H. Busemann, A. Butterworth, M. Chaussidon, S. Fallon, C. Floss, J. Gilmour, M. Gounelle, G. Graham, Y. Guan, P. R. Heck, P. Hoppe, I. D. Hutcheon, J. Huth, H. Ishii, M. Ito, S. B. Jacobsen, A. Kearsley, L. A. Leshin, M.-C. Liu, I. Lyon, K. Marhas, B. Marty, G. Matrajt, A. Meibom, S. Messenger, S. Mostefaoui, S. Mukhopadhyay, K. Nakamura-Messenger, L. Nittler, R. Palma, R. O. Pepin, D. A. Papanastassiou, F. Robert, D. Schlutter, C. J. Snead, F. J. Stadermann, R. Stroud, P. Tsou, A. Westphal, E. D. Young, K. Ziegler, L. Zimmermann, and E. Zinner 2006. Isotopic compositions of cometary matter returned by Stardust. *Science* **314**, 1724–1728.

Mellor, M. 1974. *A Review of Basic Snow Mechanics*. U.S. Army Cold Regions Research and Engineering Laboratory.

Melosh, H. J., E. V. Ryan, and E. Asphaug 1992. Dynamic Fragmentation in Impacts: Hydrocode Simulation of Laboratory Impacts. *Journal of Geophysical Research* **97**, 14735–14759.

Michikami, T., K. Moriguchi, S. Hasegawa, and A. Fujiwara 2007. Ejecta velocity distribution for impact cratering experiments on porous and low strength targets. *Planetary and Space Science* **55**, 70–88.

Miura, Y. N., T. Noguchi, A. Tsuchiyama, H. Yano, S. Yoshida, and K. Nagata 2008. Compressive strength measurements of meteorites and terrestrial rocks: Implications for physical properties of asteroidal surfaces. In *Proceedings of the Japan Geoscience Union Meeting, P168-P002*.

Mizutani, H., Y. Takagi, and S.-i. Kawakami 1990. New Scaling Laws on Impact Fragmentation. *Icarus* **87**, 307–326.

Nakamura, A. M., K. Hiraoka, Y. Yamashita, and N. Machii 2009. Collisional disruption experiments of porous targets. *Planetary and Space Science* **57**, 111–118.

Nakamura, A. M., P. Michel, and M. Setoh 2007. Weibull parameters of Yakuno basalt targets used in documented high-velocity impact experiments. *Journal of Geophysical Research* **112**, 1–7.

Nakamura, A. M., F. Yamane, T. Okamoto, and S. Takasawa 2014. Size dependence of the disruption threshold: laboratory examination of millimeter—centimeter porous targets. *Planetary and Space Science*, in press.

Nakamura, T., T. Noguchi, A. Tsuchiyama, T. Ushikubo, N. T. Kita, J. W. Valley, M. E. Zolensky, Y. Kakazu, K. Sakamoto, E. Mashio, K. Uesugi, and T. Nakano 2008. Chondrulelike objects in short-period comet 81P/Wild 2. *Science* **321**, 1664–1667.

National Astronomical Observatory of Japan (Ed.) 2012. *Chronological Scientific Tables*. Maruzen Co., Ltd.

Niimi, R., T. Kadono, M. Arakawa, M. Yasui, K. Dohi, A. M. Nakamura, Y. Iida, and A. Tsuchiyama 2011. In situ observation of penetration process in silica aerogel: Deceleration mechanism of hard spherical projectiles. *Icarus 211*(2), 986–992.

Niimi, R., T. Kadono, A. Tsuchiyama, K. Okudaira, S. Hasegawa, M. Tabata, T. Watanabe, M. Yagishita, N. Machii, A. M. Nakamura, K. Uesugi, A. Takeuchi, and T. Nakano 2012. Size and Density Estimation From Impact Track Morphology in Silica Aerogel: Application To Dust From Comet 81P/Wild 2. *The Astrophysical Journal* **744**, 18 (5 pages).

Ogliore, R. C., G. R. Huss, K. Nagashima, a. L. Butterworth, Z. Gainsforth, J. Stodolna, a. J. Westphal, D. Joswiak, and T. Tyliszczak 2012. Incorporation of a Late-Forming Chondrule Into Comet Wild 2. *The Astrophysical Journal* **745**, L19.

Okamoto, T., A. M. Nakamura, S. Hasegawa, K. Kurosawa, K. Ikezaki, and A. Tsuchiyama 2013. Impact experiments of exotic dust grain capture by highly porous primitive bodies. *Icarus* **224**, 209–217.

Öpic, E. J. 1966. Sun-Grazing Comets and Tidal Disruption. *Irish Astronomical Journal* **7**, 141–161.

Petro, N., and C. Pieters 2004. Surviving the heavy bombardment: Ancient material at the surface of South Pole-Aitken Basin. *Journal of Geophysical Research:* **109**, E06004 (13 pages).

Pike, R. J. 1974. Depth/diameter relations of fresh lunar craters: Revision from spacecraft data. *Geophysical Research Letters* **1**, 291–294.

Popova, O., J. Borovicka, W. K. Hartmann, P. Spurny, E. Gnos, I. Nemtchinov, and J. M. Trigo-Rodrquez 2011. Very low strengths of interplanetary meteoroids and small asteroids. *Meteoritics & Planetary Science* **46**, 1525–1550.

Richardson, J., H. Melosh, C. Lisse, and B. Carcich 2007. A ballistics analysis of the Deep Impact ejecta plume: Determining Comet Tempel 1's gravity, mass, and density. *Icarus* **190**, 357–390.

Richardson, J. E., and H. Melosh 2013. An examination of the Deep Impact collision site on Comet Tempel 1 via Stardust-NExT: Placing further constraints on cometary surface properties. *Icarus 222*(2), 492–501.

Rumpf, H. 1970. Zur Theorie der Zugfestigkeit von Agglomeraten bei Kraftübertragung an Kontaktpunkten. *Chemie Ingenieur Technik* **42**, 538–540.

Ryan, E., D. Davis, and I. Giblin 1999. A laboratory impact study of simulated Edgeworth—Kuiper belt objects. *Icarus* **62**, 56–62.

Ryan, E., W. Hartmann, and D. Davis 1991. Impact experiments. 3: Catastrophic fragmentation of aggregate targets and relation to asteroids. *Icarus* **94**, 283–298.

Schmude, R. 2010. *Comets and How to Observe Them*. Astronomers' Observing Guides. Springer.

Sephton, M. A. 2002. Organic compounds in carbonaceous meteorites. *Natural product reports* **19**, 292–311.

Setoh, M., A. Nakamura, P. Michel, K. Hiraoka, Y. Yamashita, S. Hasegawa, N. Onose, and K. Okudaira 2010. High- and low-velocity impact experiments on porous sintered glass bead targets of different compressive strengths: Outcome sensitivity and scaling. *Icarus* **205**, 702–711.

Shackelford, J., and W. Alexander 2000. *CRC Materials Science and Engineering Handbook, Third Edition*. Taylor & Francis.

Shimaki, Y., and M. Arakawa 2012. Experimental study on collisional disruption of highly porous icy bodies. *Icarus* **218**, 737–750.

Shu, F. H., H. Shang, M. Gounelle, A. E. Glassgold, and T. Lee 2001. The Origin of Chondrules and Refractory Inclusions in Chondritic Meteorites.

Shu, F. H., H. Shang, and T. Lee 1996. Toward an astrophysical theory of chondrites. *Science* **271**, 1545–1552.

Sirono, S. 2000. Do Cometesimal Collisions Lead to Bound Rubble Piles or to Aggregates Held Together by Gravity? *Icarus* **145**, 230–238.

Takagi, Y., H. Mizutani, and S. Kawakami 1984. Impact fragmentation experiments of basalts and pyrophyllites. *Icarus* **59**, 462–477.

Thomas, N. 2009. The nuclei of Jupiter family comets: A critical review of our present knowledge. *Planetary and Space Science* **57**, 1106–1117.

Thomas, P. C. 2010. Sizes, shapes, and derived properties of the saturnian satellites after the Cassini nominal mission. *Icarus* **208**, 395–401.

Thomas, P. C., J. W. Armstrong, S. W. Asmar, J. a. Burns, T. Denk, B. Giese, P. Helfenstein, L. Iess, T. V. Johnson, A. McEwen, L. Nicolaisen, C. Porco, N. Rappaport, J. Richardson, L. Somenzi, P. Tortora, E. P. Turtle, and J. Veverka 2007. Hyperion's sponge-like appearance. *Nature* **448**, 50–53.

Thomas, P. C., J. Veverka, M. J. Belton, A. Hidy, M. F. A'Hearn, T. Farnham, O. Groussin, J.-Y. Li, L. a. McFadden, J. Sunshine, D. Wellnitz, C. Lisse, P. Schultz, K. J. Meech, and W. A. Delamere 2007. The shape, topography, and geology of Tempel 1 from Deep Impact observations. *Icarus* **187**, 4–15.

Tsubaki, J. 1984. New interpretations of equation of Rumpf and their application. *Journal of the Society of Powder Technology, Japan* **21**, 30–39.

Tsuchiyama, A., T. Nakamura, T. Nakano, and N. Nakamura 2002. Three-dimensional description of the kobe meteorite by micro x-ray ct method: Possibility of three-dimensional curation of meteorite samples. *Geochemical Journal* **36**, 369–390.

Vincent, J. B., N. Oklay, S. Marchi, S. Höfner, and H. Sierks 2014. Craters on comets. *Planetary and Space Science*, in press.

Walsh, K. J., A. Morbidelli, S. N. Raymond, D. P. O'Brien, and A. M. Mandell 2011. A low mass for Mars from Jupiter's early gas-driven migration. *Nature* **475**, 206–208.

Walsh, K. J., A. Morbidelli, S. N. Raymond, D. P. O'Brien, and A. M. Mandell 2012. Populating the asteroid belt from two parent source regions due to the migration of giant planets-"The Grand Tack". *Meteoritics and Planetary Science* **47**, 1941–1947.

White, O., and P. Schenk 2011. Crater shapes on the saturnian satellites: New measurements using Cassini stereo images. *Lunar and Planetary Science Conference* **42**, 2283.

Wooden, D., S. Desch, and D. Harker 2007. Comet grains and implications for heating and radial mixing in the protoplanetary disk. In B. Reipurth, D. Jewitt, and K. Keil (Eds.), *Protostars and planets V*, Volume 951, pp. 815–833. Univ. Arizona Press, Tucson.

Wünnemann, K., G. S. Collins, and H. J. Melosh 2006. A strain-based porosity model for use in hydrocode simulations of impacts and implications for transient crater growth in porous targets. *Icarus* **180**, 514–527.

Yasui, M., M. Arakawa, S. Hasegawa, Y. Fujita, and T. Kadono 2012. In situ flash X-ray observation of projectile penetration processes and crater cavity growth in porous gypsum target analogous to low-density asteroids. *Icarus* **221**, 646–657.

Yomogida, K., and T. Matsui 1984. Multiple parent bodies of ordinary chondrites. *Earth and Planetary Science Letters* **68**, 34–42.

Zahnle, K., P. Schenk, H. Levison, and L. Dones 2003. Cratering rates in the outer Solar System. *Icarus* **163**, 263–289.

Zolensky, M. E., T. J. Zega, H. Yano, S. Wirick, A. J. Westphal, M. K. Weisberg, I. Weber, J. L. Warren, M. A. Velbel, A. Tsuchiyama, P. Tsou, A. Toppani, N. Tomioka,

K. Tomeoka, N. Teslich, M. Taheri, J. Susini, R. Stroud, T. Stephan, F. J. Stadermann, C. J. Snead, S. B. Simon, A. Simionovici, T. H. See, F. Robert, F. J. M. Rietmeijer, W. Rao, M. C. Perronnet, D. A. Papanastassiou, K. Okudaira, K. Ohsumi, I. Ohnishi, K. Nakamura-Messenger, T. Nakamura, S. Mostefaoui, T. Mikouchi, A. Meibom, G. Matrajt, M. A. Marcus, H. Leroux, L. Lemelle, L. Le, A. Lanzirotti, F. Langenhorst, A. N. Krot, L. P. Keller, A. T. Kearsley, D. Joswiak, D. Jacob, H. Ishii, R. Harvey, K. Hagiya, L. Grossman, J. N. Grossman, G. A. Graham, M. Gounelle, P. Gillet, M. J. Genge, G. Flynn, T. Ferroir, S. Fallon, S. Fakra, D. S. Ebel, Z. R. Dai, P. Cordier, B. Clark, M. Chi, A. L. Butterworth, D. E. Brownlee, J. C. Bridges, S. Brennan, A. Brearley, J. P. Bradley, P. Bleuet, P. A. Bland, and R. Bastien 2006. Mineralogy and petrology of comet 81P/Wild 2 nucleus samples. *Science* **314**, 1735–1739.